UC San Diego

UC San Diego Electronic Theses and Dissertations

Title

Investigating Internal Short Circuit Heating to Inform Novel Lithium-Ion Battery Safety Strategies

Permalink

https://escholarship.org/uc/item/46d41486

Author

Noelle, Daniel John

Publication Date

2018

Peer reviewed|Thesis/dissertation

eScholarship.org Powered by the California Digital Library
University of California

UNIVERSITY OF CALIFORNIA, SAN DIEGO

Investigating Internal Short Circuit Heating to Inform Novel Lithium-Ion Battery Safety Strategies

A dissertation submitted in partial satisfaction
of the requirements for the degree Doctor of Philosophy

in

Materials Science and Engineering

by

Daniel John Noelle

Committee in Charge:

Professor Yu Qiao, Chair
Professor Renkun Chen
Professor Darren Lipomi
Professor Ping Liu
Professor Jian Luo

2018

Copyright

Daniel John Noelle, 2018

All rights reserved.

This dissertation of Daniel John Noelle is approved, and it is acceptable in quality and form for publication on microfilm and electronically:

_____

_____

_____

_____

_____
Chair

University of California, San Diego

2018

Table of Contents

Signature Page iii

Table of Contents iv

List of Abbreviations viii

List of Symbols ix

List of Figures xii

List of Tables xv

Acknowledgements xvi

Vita xviii

Abstract of the Dissertation xx

Chapter 1 Lithium-ion battery safety challenges and implications for electric vehicles 1

1.1 Importance of lithium-ion battery (LIB) safety in electric vehicles (EVs) 1

1.1.1 Rise in recent LIB fire accidents 1

1.1.2 Public perception of EV safety 2

1.1.3 Cost of an unsafe LIB 3

1.1.4 Emerging EV market considerations 3

1.2 Short circuit dangers in EVs 4

1.2.1 Threat of thermal runaway 4

1.2.2 Short circuit formation in collisions 5

1.3 LIB safety features for EVs 6

1.3.1 Primary protection structures and failsafe features 6

1.3.2 Shutdown additives 7

1.3.3 Fire-retardants 9

1.3.4 Encapsulation of shutdown additives and fire-retardants 10

1.3.5 Module and pack level temperature and fire suppression 10
1.4 Safety-first design approach to long-range EVs 11
1.4.1 Significance of LIB safety on EV mass 11
1.4.2 Addressing short circuit failures immediately upon impact 12
1.4.3 Developing advanced, light-weight EV safety strategies 13
1.5 Outline of thesis 14
Chapter 2 Internal resistance and polarization dynamics of lithium-ion batteries upon internal shorting 17
2.1 Introduction 17
2.2 Experimental procedure and data processing 20
2.2.1 Reference cell system 20
2.2.2 Direct current internal resistance testing 21
2.2.3 External shorting and nail penetration testing 23
2.2.4 Determining heat transfer characteristics 25
2.2.5 Electrolyte conductivity and viscosity measurement 27
2.3 Model development and calibration 28
2.3.1 Modeling electrolyte conductivity 28
2.3.2 Relating electrolyte and polarization resistance 31
2.3.3 Ion polarization 32
2.4 Discussion 34
2.4.1 Results of direct current internal resistance testing 34
2.4.2 Low current discharge regime 38
2.4.3 Elevated current discharge regime 38
2.4.4 Function and limitations of this interpretation 40
2.4.5 External shorting and nail penetration tests 43
2.4.6 Implications for thermal runaway mitigation 45

2.4.7 Significance of abuse responsive impedance increases 48

2.5 Concluding remarks 50

2.6 Acknowledgements 51

Chapter 3 Aggressive electrolyte poisons and multifunctional fluids comprised of diols and diamines for emergency shutdown of lithium-ion batteries 52

3.1 Introduction 52

3.2 Experimental methods and data acquisition 55

3.2.1 Reference cell system 55

3.2.2 Poisoning agent candidate selection and mechanism evaluation 56

3.2.3 Simultaneous nail penetration and injection testing 57

3.2.4 Modified cell case encapsulated poison impact testing 60

3.3 Poison selection and evaluation 63

3.3.1 Diol poison selection motivations and mechanism evaluation 63

3.3.2 Simultaneous nail penetration and poison injection testing 69

3.4 Electrolyte poisoning device design 73

3.4.1 Encapsulated poison impact testing 73

3.4.2 Multifunctional thermal management systems 76

3.5 Conclusion 79

3.6 Acknowledgements 80

Chapter 4 Improved safety and mechanical characterizations of thick lithium-ion battery electrodes structured with porous metal current collectors 81

4.1 Introduction 81

4.2 Experimental methods and data acquisition 83

4.2.1 Electrode processing 83

4.2.2 Electrochemical performance and abuse characterization 85

4.2.3 Mechanical property characterization 86

4.3 Results 87
4.3.1 High aerial capacity electrode fabrication 87
4.3.2 Electrochemical performance evaluation 87
4.3.3 External short circuit and nail penetration responses 90
4.3.4 Shear testing 91
4.3.5 Three-point bending 92
4.4 Discussion 95
4.4.1 Balancing rate capability and short circuit safety 95
4.4.2 Prospects and challenges for multifunctional application 97
4.5 Conclusion 100
4.6 Acknowledgements 100
Chapter 5 Summary and future work 101
References 107

List of Abbreviations

BMS ……. battery management system

BTMS …….. battery thermal management system

CB …… carbon black

CMC …….. carboxymethyl cellulose

DCIR …….. direct current internal resistance

DI ……. deionized water

DMC …….. dimethyl carbonate

EC ……... ethylene carbonate

EMC ……. ethyl methyl carbonate

EV ……. electric vehicle

IPC ……... interpenetrating phase composite

LC …….. laminate composite

LCO …….. lithium cobalt oxide

LIB …….. lithium-ion battery

LIR2032 ……. lithium-ion rechargeable 20 mm diameter 3.2 mm thick coin cell

LIR2450 ……. lithium-ion rechargeable 24 mm diameter 5.0 mm thick coin cell

NMP ……... N-methyl-2-pyrrolidone

PVDF …….. polyvinylidene fluoride

SBR ……... styrene-butadiene rubber

SOC ……... state of charge

List of Symbols

A …… ionic conductivity relation proportionality constant (S.Pa.s.m^2.mol^{-1}.K^{-1})

c_{p} ……..…….... effective system heat capacity (J.g^{-1}.K^{-1})

C ……..…… lithium-ion concentration of electrolyte (mol.m^{-3})

C_0 ……..……... lithium-ion concentration of unpolarized electrolyte (mol.m^{-3})

$\bar{C}_{\mathrm{i}}$ ……..……..……. average lithium-ion concentration of electrolyte in select region (mol.m^{-3})

E_{A} ……..……..…….. activation energy of electrolyte viscosity (J.mol^{-1})

$E_{\mathrm{A},1}$ ……..……..……. first parameter defining activation energy of electrolyte viscosity (J.mol^{-1})

$E_{\mathrm{A},2}$ ……..…… second parameter defining activation energy of electrolyte viscosity (m^3.mol^{-1})

h^*_{dis} ……..……... heat dissipation frequency coefficient (Hz)

I_{x} ……..……..…….. current rate for select discharge type (A)

m ……..…….. cell system mass (g)

$\dot{q}_{\mathrm{dis}}$ ……..……..…… rate of heat dissipation (W)

$\dot{q}_{\mathrm{gen}}$ ……..…… rate of heat generation (W)

$\dot{q}_{\mathrm{gen,eff}}$ ……..……..…… effective heat generation rate of poisoned cell (W)

$\dot{q}_{\mathrm{gen,ref}}$ ……. reference heat generation rate of unpoisoned cell (W)

$\dot{q}_{\mathrm{net}}$ ……..…… net rate of heating / cooling (W)

Q ……..……..…….. charged current capacity (A.h)

$r_{\mathrm{p,i}}$ ……..…….. specific resistance of polarized electrolyte in select region (Ω)

R ……..…….. ideal gas constant (J.mol^{-1}.K^{-1})

R_{eff} ……..…… effective resistance to heat generation of poisoned cell (Ω)

R_{elec} …….. resistance of electrolyte (Ω)

R_{ext} ……. external shorting resistance (Ω)

R_{int} ……. internal resistance (Ω)

R_{o} ……..……. ohmic resistance (Ω)

R_{p} ……..……. polarization resistance (Ω)

$R_{\mathrm{p,i}}$ …… polarization resistance contribution of electrolyte in select region (Ω)

R_{ref} ……..…… reference resistance to heat generation of unpoisoned cell (Ω)

t ……..……..…… time (s)

t_{ini} ……..……. initial time of heat dissipation frequency coefficient measurement interval (s)

T ……..……. temperature (K)

T_0 ……..……... ambient temperature (K)

V_{emf} ……. electromotive force (V)

V_{t} ……..…….. terminal voltage (V)

δ_{i} ……..…… thickness of select region (m)

ε ……..……... permittivity of electrolyte solvent (unitless)

ε_1 ……..……... first parameter defining permittivity of electrolyte solvent (unitless)

ε_2 ……..……. second parameter defining permittivity of electrolyte solvent (K^{-1})

μ ……..……. viscosity of electrolyte (Pa.s)

μ^* ……..……..... reference viscosity of electrolyte (Pa.s)

μ_1^* ……..……. first parameter defining reference viscosity of electrolyte (Pa.s)

μ_2^* ……..……. second parameter defining reference viscosity of electrolyte ($m^3.mol^{-1}$)

σ ……..…… ionic conductivity of electrolyte ($S.m^{-1}$)

i ……..……select region, =a, c, or s

x ……..…...…… select discharge type, =app or sc

a ……... anode

c …… cathode

s …….. separator

app ……. applied

sc …… short circuit

List of Figures

Figure 2.1 (a) Measured viscosity of $LiPF_6$ EC:EMC (1:1 w:w) electrolyte as a function of temperature for salt concentrations from 0.25 M to 2.37 M. (b) Fitted Arrhenius-type viscosity parameters as functions of the salt concentration. 30

Figure 2.2 Measured and modeled ionic conductivity of $LiPF_6$ EC:EMC (1:1 w:w) electrolyte as a function of the salt concentration at 23 ^oC. 31

Figure 2.3 (a) Modeled ionic conductivity of $LiPF_6$ EC:EMC (1:1 w:w) electrolyte with respect to the salt concentration and the temperature. (b) Corresponding modeled electrolyte resistance relative to the nominal 1 M $LiPF_6$ reference concentration at 23 ^oC 32

Figure 2.4 (a) LIR2450 cell DCIR terminal voltage and electromotive force responses for low applied current discharge rates up to 1.0 C and (b) elevated applied current discharge rates of 2.0 C to 10.0 C. (c) Corresponding ohmic resistances and dynamic polarization resistances for low current discharge rates and (d) elevated current discharge rates measured over time. 35

Figure 2.5 (a) Heat dissipation frequency coefficients denoting the magnitude of the slope for the linear fitter curves, determined following DCIR and nail penetration tests. (b) System heat capacities denoting the ratio between joule heat generated versus the product of cell mass and theoretical temperature accrued without heat dissipation upon DCIR current termination..... 36

Figure 2.6 (a) DCIR dynamic polarization resistance responses of LIR2450 cells at low and elevated applied current discharge rates, relative to the assumed 0.2 C unpolarized 1 M electrolyte reference profile. (b) Corresponding measured cell temperature (c, d) local average lithium-ion concentrations in the electrolyte within the cathode and anode regions. 37

Figure 2.7 (a) Local average lithium-ion concentrations in the cathode, anode, and separator regions for a LIR2450 cell discharged at 10.0 C applied current rate, as a function of time. (b) Ohmic resistance, dynamic polarization resistance contributions from the individual regions , and total polarization resistance influences to the measured internal impedance. 40

Figure 2.8 (a) Heat generation rate, discharge current, and cell temperature responses to external shorting and nail penetration testing of fully charged LIR2450 cells. (b) Corresponding ohmic and polarization resistances applied to the relative electrolyte resistance comparison model, showing rapid depletion of ions in the electrolyte within the cathode region. 44

Figure 2.9 Schematic illustrating transition from ohmically-controlled short circuit to polarization controlled short circuit. 44

Figure 2.10 Predicted internal impedance, heat generation rate, and cell temperature responses of LIR2450 cells upon nail penetration, subjected to (a, c, e) increased ohmic resistances or (b, d, f) increased polarization resistances by two-fold, five-fold, ten-fold, and twenty-fold relative to the measured reference response. 49

Figure 3.1 Modified cell case reconstruction and simultaneous nail penetration and poison injection testing. 59

Figure 3.2 Modified LIR2450 coin cell with encapsulated poison aluminum container incorporated into the cell case shown before and after drop tower impact testing. 62

Figure 3.3 (a) Viscosity of pristine electrolyte, diols, and (b) electrolyte / diol mixed solutions. 64

Figure 3.4 Ionic conductivity of pristine electrolyte / diol mixed solutions. 66

Figure 3.5 (a) Reaction temperature of 2 mL mixture of electrolyte components with 20 vol% 1,2-ethanediamine and (b) image of solid reaction product after 10 minutes. 68

Figure 3.6 Ionic conductivity of pristine electrolyte / diamine mixed solutions. 69

Figure 3.7 Cell temperature response observed in simultaneous nail penetration and diol injection testing of LIR2450 coin cells. 70

Figure 3.8 (a) Heat generation rate and (b) effective internal resistance increase dynamics observed in simultaneous nail penetration and diol injection testing of LIR2450 coin cells. 71

Figure 3.9 Cell temperature response observed in simultaneous nail penetration and diamine injection testing of LIR2450 coin cells. 72

Figure 3.10 (a) Heat generation rate and (b) effective internal resistance increase dynamics observed in simultaneous nail penetration and diamine injection testing of LIR2450 coin cells. 72

Figure 3.11 Cell temperature response observed in impact testing of LIR2450 cells with modified cases housing 1,5-pentanediol. 74

Figure 3.12 Simultaneous nail penetration and poison injection temperature response of LIR2450 cells with 400 µL of 1,2-ethanediol, 1,2-ethanediamine, and 1,2-ethanediol:1,2-ethanediamine 4:1 v:v mixed solution..... 77

Figure 4.1 Ultrasonic power application, mixing sequence, and consequent temperature dynamics of (a) cathode and (b) anode slurries processed using QSonica Q55 Sonicator with 3.2 mm diameter submersible ultrasonic horn homogenized in 10 mL Pyrex beakers. Images of (c) cathode materials and (d) anode materials dispersed in processing solvent to produce high-density slurries. 88

Figure 4.2 (a) Voltage / capacity profiles and times for increasing discharge current rates and (b) formation / cycling capacity for 600 µm thick, 1.98 cm^2 interpenetrating phase composite $LiCoO_2$ / graphite electrodes arranged in uniaxial full cell orientation in LIR2032 coin cells..... 90

Figure 4.3 (a) External short circuit temperature response and discharge current dynamics of LIR2032 coin cells with laminate composite (LC) electrodes and interpenetrating phase composite (IPC) electrodes. (b) Nail penetration temperature response. Images of (c) LC electrodes and (d) IPC electrodes used for electrochemical evaluation and abuse testing..... 91

Figure 4.4 Shear force-displacement profiles of current collector and electrode 1.98 cm^2 samples with a 3.2 mm diameter piston pressing the geometric centers into a 3.8 mm diameter gap at a rate of 10 $\mu m.s^{-1}$ for (a) cathodes as well as (b) anodes in laminate composite and interpenetrating phase composite formations. Images show fracture of (c) cathodes and (d) anodes after testing. 93

Figure 4.5 (a) Three-point bending force-displacement profiles for individual laminate composite and interpenetrating phase composite electrode and (b) electrode stack assemblies totaling 2.5 mm thickness, all tested with 12.5 mm width and support length loaded at a rate of 10 $\mu m.s^{-1}$. (c, d) Enhanced images of regions used to determine flexural modulus and bending stiffness..... 94

List of Tables

Table 2.1 Heat transfer measurement parameters. 27

Table 2.2 Conductivity relation coefficients for $LiPF_6$ EC:EMC (1:1 w:w) electrolyte and reference parameters for relative electrolyte resistance. 30

Table 2.3 Thicknesses of composite cathode, separator, and composite anode. 34

Table 3.1 Dielectric constant of pristine electrolyte, electrolyte components, and diols. 65

Table 4.1 Electrochemical characteristics of LIR2032 cells with laminate composite electrodes and interpenetrating phase composite electrodes. 89

Acknowledgements

I would like to express my sincerest gratitude to Professor Yu Qiao for his guidance as my advisor, as well as the support of my colleagues, Dr. Anh V. Le, Dr. Meng Wang, and Dr. Yang Shi. This time spent learning alongside such intelligent, charismatic, and good-hearted professionals has been an honor. I greatly appreciate their invitation to join this wonderful team, address tough challenges for noble causes, and dream the bigger dreams. I truly could not have asked for a more fulfilling experience in pursuing my Ph.D.

Special thanks to my dissertation review committee, Professor Renkun Chen, Professor Darren Lipomi, Professor Ping Liu, and Professor Jian Luo, for providing their insightful feedback and valuable time.

Lastly, I would like to thank my parents for their unending love and encouragement, instilling in me the drive to undertake difficult challenges with confidence, so that I may always strive to better myself.

Chapter 2, in full, is a reprint of the published material as it appears in Applied Energy. Daniel Noelle, Meng Wang, Anh V. Le, Yang Shi, and Yu Qiao., 2018. Internal resistance and polarization dynamics of lithium-ion batteries upon internal shorting. *Appl. Energy, 212, 796-808*. The dissertation author was the primary investigator and first author of the paper.

Chapter 3, in part, is a reprint of the published material as it appears in Journal of Power Sources. Daniel Noelle, Yang Shi, Meng Wang, Anh V. Le, and Yu Qiao., 2018. Aggressive electrolyte poisons and multifunctional fluids comprised of diols and diamines for emergency shutdown of lithium-ion batteries. *J. Power Sources, 384, 93-97.* The dissertation author was the primary investigator and first author of the paper.

Chapter 4, in full, is a reprint of the material submitted for publication. Daniel Noelle, Meng Wang, and Yu Qiao. Improved safety and mechanical characterizations of thick lithium-ion battery electrodes structured with porous metal current collectors. The dissertation author was the primary investigator and first author of the paper.

Vita

2018	Doctor of Philosophy	UC San Diego
2014	Master of Science	UC San Diego
2013	Bachelor of Science	Virginia Tech

Publications

D.J. Noelle, M. Wang, A.V. Le, Y. Shi, Y. Qiao, Internal resistance and polarization dynamics of lithium-ion batteries upon internal shorting, Appl. Energy. 212 (2018) 796–808.

D.J. Noelle, Y. Shi, M. Wang, A.V. Le, Y. Qiao, Aggressive electrolyte poisons and multifunctional fluids comprised of diols and diamines for emergency shutdown of lithium-ion batteries, J. Power Sources. 384 (2018) 93–97.

M. Wang, **D.J. Noelle**, Y. Shi, A.V. Le, Y. Qiao, Effect of notch depth of modified current collector on internal-short-circuit mitigation for lithium-ion battery, J. Phys. D. Appl. Phys. 51 (2018).

M. Wang, A.V. Le, Y. Shi, **D.J. Noelle**, D. Wu, J. Fan, W. Lu, Y. Qiao, Sigmoidal current collector for lithium-ion battery, J. Appl. Phys. 121 (2017) 15303.

M. Wang, A.V. Le, **D.J. Noelle**, Y. Shi, Y.S. Meng, Y. Qiao, Internal-short-mitigating current collector for lithium-ion battery, J. Power Sources. 348 (2017) 84–93.

Y. Shi, **D.J. Noelle**, M. Wang, A.V. Le, H. Yoon, M. Zhang, Y.S. Meng, J. Fan, D. Wu, Y. Qiao, Mitigating thermal runaway of lithium-ion battery through electrolyte displacement, Appl. Phys. Lett. 110 (2017) 63902.

M. Wang, A.V. Le, Y. Shi, **D.J. Noelle**, Y. Qiao, Heterogeneous current collector in lithium-ion battery for thermal-runaway mitigation, Appl. Phys. Lett. 110 (2017) 83902.

A.V. Le, M. Wang, **D.J. Noelle**, Y. Shi, H. Yoon, M. Zhang, Y.S. Meng, Y. Qiao, Effects of macromolecular configuration of thermally sensitive binder in lithium-ion battery, J. Appl. Polym. Sci. 134 (2017) 45078.

M. Wang, L. Zhu, A.V. Le, **D.J. Noelle**, Y. Shi, Y. Zhong, F. Hao, X. Chen, Y. Qiao, A multifunctional battery module design for electric vehicle, J. Mod. Transp. 25 (2017) 218-222.

A.V. Le, M. Wang, **D.J. Noelle**, Y. Shi, Y.S. Meng, D. Wu, J. Fan, Y. Qiao, Using high-HFP-content cathode binder for mitigation of heat generation of lithium-ion battery, Int. J. Energy Res. 41 (2017) 2430-2438.

M. Wang, Y. Shi, **D.J. Noelle**, A.V. Le, Y. Qiao, Effect of groove width of modified current collector on internal short circuit of abused lithium-ion battery, J. Phys. D. Appl. Phys. 50 (2017) 425503.

M. Wang, Y. Shi, **D.J. Noelle**, A. V. Le, H. Yoon, H. Chung, M. Zhang, Y.S.Y.S. Meng, Y. Qiao, Internal short circuit mitigation of high-voltage lithium-ion batteries with functional current collectors, RSC Adv. 7 (2017) 45662–45667.

A.V. Le, M. Wang, **D.J. Noelle**, Y. Shi, Y. Qiao, Mitigating thermal runaway of lithium-ion battery by using thermally sensitive polymer blend as cathode binder, J. Appl. Polym. Sci. 135 (2017) 45737.

Y. Shi, **D.J. Noelle**, M. Wang, A.V. Le, H. Yoon, M. Zhang, Y.S. Meng, Y. Qiao, Exothermic behaviors of mechanically abused lithium-ion batteries with dibenzylamine, J. Power Sources. 326 (2016) 514–521.

M. Wang, A.V. Le, Y. Shi, **D.J. Noelle**, H. Yoon, M. Zhang, Y.S. Meng, Y. Qiao, Effects of Angular Fillers on Thermal Runaway of Lithium-Ion Battery, J. Mater. Sci. Technol. 32 (2016) 1117–1121.

Y. Shi, **D.J. Noelle**, M. Wang, A. V. Le, H. Yoon, M. Zhang, Y.S. Meng, Y. Qiao, Role of Amines in Thermal-Runaway-Mitigating Lithium-Ion Battery, ACS Appl. Mater. Interfaces. 8 (2016) 30956–30963.

M. Wang, A.V. Le, **D.J. Noelle**, Y. Shi, H. Yoon, M. Zhang, Y.S. Meng, Y. Qiao, Effects of electrode pattern on thermal runaway of lithium-ion battery, Int. J. Damage Mech. 0 (2016) 1–8.

A.V. Le, M. Wang, Y. Shi, **D.J. Noelle**, Y. Qiao, W. Lu, Effects of additional multiwall carbon nanotubes on impact behaviors of LiNi0.5Mn0.3Co0.2O2 battery electrodes, J. Appl. Phys. 118 (2015) 85312.

A.V. Le, M. Wang, Y. Shi, **D.J. Noelle**, Y. Qiao, Heat generation of mechanically abused lithium-ion batteries modified by carbon black micro-particulates, J. Phys. D. Appl. Phys. 48 (2015) 385501.

Abstract of the Dissertation

Investigating Internal Short Circuit Heating to Inform
Novel Lithium-Ion Battery Safety Strategies

by

Daniel John Noelle

Doctor of Philosophy in Materials Science and Engineering

University of California, San Diego, 2018

Professor Yu Qiao, Chair

Lithium-ion batteries are prone to severe, mechanically-induced short circuit events that can lead to thermal runaway. Risk mitigating components commonly include primary protection structures and thermally-triggered failsafe mechanisms active at high temperatures, but features taking effect in the early stages of the joule heating regime are uncommon. To bridge this gap, the nature of the rate-limiting resistance dynamics is examined experimentally to clarify the progression of discharge events, and how to effectively address them upon short circuit initiation.

Direct current internal resistance, external shorting, and nail penetration experiments are performed on LIR2450 format 120 mAh $LiCoO_2$ / graphite coin cells to probe resistance and consequent heat generation dynamics over resolute temperature and time scales. The study reveals a low-resistance, electrically-controlled capacitive discharge event occurs immediately upon shorting which is subsequently throttled by increasing ionic resistances. An electrolyte resistance model is postulated and validated experimentally in terms of concentration, temperature, permittivity, and viscosity, to show how charge carriers polarize and reallocate within a cell when operated under stress.

The information attained identifies the need to exacerbate electrical resistance via mechanical response to suppress the powerful capacitive discharge feature immediately upon impact and suppress ion transport through electrolyte to halt continued discharge thereafter. Forming thick interpenetrating phase composite electrodes within brittle porous metal current collectors are shown to curb discharge power by preventing the formation of electrically conductive pathways between current collectors, as well as increasing the distance charge carriers must travel to liberate joule heat. Poisons capable of hindering ion transport to halt continued discharge are identified consulting the postulated electrolyte resistance model and tested via simultaneous injection and nail penetration testing of LIR2450 coin cells. Multifunctional design strategies are discussed for imparting greater degrees of integration within electronics by the lithium-ion batteries to reduce overall weight and volume upon further development of safe-cell technologies.

Chapter 1 Lithium-ion battery safety challenges and implications for electric vehicles

1.1 Importance of lithium-ion battery (LIB) safety in electric vehicles (EVs)

1.1.1 Rise in recent LIB fire accidents

On October 1st, 2013, a Tesla model S driving on route 167 in Kent, Washington, ran over a large piece of metallic debris, creating a 3" diameter hole through the 1/4" thick armor plate situated on the undercarriage of the vehicle, penetrating the battery pack [1]. The damage caused an uncontrolled short circuit to form in one of the lithium-ion battery (LIB) modules, resulting in a fire which engulfed the front of the vehicle. Video of the incident and images of the aftermath received widespread attention and reporting by national news outlets [2–5], highlighting electric vehicle (EV) safety as a controversial topic. Over the next six weeks, two additional Tesla model S fires would occur as a result of collision events [6], entrenching the stigmatization of EVs as unsafe in the public sphere, ushering in a new era of challenges concerning consumer perception and adoption in the personal vehicle marketplace.

Knowledge of LIB danger was thrust upon travelers in 2016, as the Department of Transportation announced the Samsung Galaxy Note 7 ban from passenger planes in airports throughout the United States, following the company's second recall of the product [7]. Originally issued following several LIB malfunctions grounding Boeing 787 Dreamliner aircraft [6], battery regulations are now explicitly communicated in Transportation Security Agency lines upon airport entry, alerting the public en masse of the threats posed by LIBs used in their personal electronics [8]. Further reporting of explosions resulting in injuries from faulty or improperly-used batteries

in a multitude of other electronic devices prompted investigation by the U.S. Fire Administration and Federal Emergency Management Agency in 2017, recommending enhanced safety guidelines for charging, operation, and storage of LIBs [9].

1.1.2 Public perception of EV safety

The series of LIB failure incidents over the past decade have brought safety to the forefront of conversation in the battery research, original equipment manufacturer, and EV commercial development communities. While this information is new to many in the public, these safety challenges inherent to LIBs have been known for many decades [10]. In general, these issues have received extensive attention from academic scientists and industrial technologists, the knowledge attained prompting fairly consistent safety standards among developed countries, encouraging robust EV designs [11]. In fact, because safety is a top priority of vehicle manufacturers, smart battery monitoring and thermal management systems are already widely implemented, such that there is a low incidence of serious, endangering thermal runaway events in EVs as is. Nonetheless, EVs may still experience catastrophic failure in unforeseen circumstances, as is the characteristic of any vehicle. Improving on existing systems to be failsafe in those abnormally abusive circumstances is critical to increasing EV marketplace acceptance.

In the case of the Tesla Model S fires, the spectacle of those EV crashes had far greater consequences than the flames themselves. According to surveys conducted seeking information about consumer perception of EVs, more than 40% of respondents think that EVs are an unsafe mode of transportation or are unsure due to limited understanding on the technology [12]. Visually threatening photographs of these incidents coupled with far-reaching reporting create and reinforce

negative opinions and increase apprehension among potential customers, which can delay transition to an EV-dominant travel infrastructure. Avoiding these kind of accidents is important to shaping public opinion at this critical point in time, when the transition from internal combustion engines and fossil fuels is essential to curbing greenhouse gas emissions [13].

1.1.3 Cost of an unsafe LIB

While nobody was hurt by the Model S fires, Tesla's stock price dropped by more than 25% at the end of the sixth week following the first incident in 2013, conveying both a risky investment outlook and poor public image [14]. Likewise, the day after the second Galaxy Note 7 recall, Samsung lost $17 billion in market value in addition to the $9.5 billion in lost sales from the phones themselves [15]. These costs do not even consider those of ongoing and future litigation stemming from injuries and property damage resulting from the fires [16]. While these large companies were able to afford such losses, weather the storm of bad publicity, and move forward with continued investment to address the safety challenges, those battery fire incidents might have forced a smaller start-up company into bankruptcy. Worse yet, and most importantly, the victims of LIB fires may suffer physical or emotional injury that can't be quantified in monetary terms.

1.1.4 Emerging EV market considerations

The global stock of EVs needs to reach 115 million by 2030 to meet the target set under the Paris Climate Agreement. The International Energy Agency projects global stock will not even pass 60 million by that time, if the current trajectory of technological improvements in energy

efficiency and achievement of governmental support policies is not improved upon. That said, the EV market is still very new, having only had its first consequential year of sales in 2010, so great potential for unexpected technological improvements could improve that outlook [17]. As a relatively new technology, there are many barriers to marketplace penetration, perhaps most importantly is consumer interest.

According to surveys conducted seeking information about consumer perception of EVs, the most significant factors which would dissuade a potential customer from purchasing an EV are high cost and limited drive range [12]. Aside from challenges associated with an underdeveloped charging infrastructure, this issue is inherent to the cost and energy density of the LIBs that power the vehicle. Each year, the cost and energy density of state-of-the-art commercial batteries for EVs improves incrementally, which allows EVs to be cheaper and travel further as each new make and model goes onto the market [18]. However, novel solutions are needed to produce the leap in technological advancement needed to allow EVs to compete directly with internal combustion engine vehicles in terms of cost and range, if they are to entice a larger market of interested buyers.

1.2 Short circuit dangers in EVs

1.2.1 Threat of thermal runaway

Thermal runaway is the primary safety concern for LIBs, characteristic of their energy-dense, flammable electrolyte chemistries. In the event that a LIB cell reaches a critical internal temperature, the LIB cell may experience a multitude of self-heating phenomena that can rapidly compound to raise temperature in an accelerating and uncontrolled manner, causing its flammable

materials to ignite a fire. The most significant exothermic, temperature-increase accelerating events occur in the following order [19]:

1. Lithiated graphite anode reacts with electrolyte carbonate solvent, onset at 110 ^{o}C.
2. Cathode active material decomposes, liberating oxygen, onset at 165 ^{o}C.
3. Electrolyte solvent decomposes, onset at 180^{o}C.
4. Flammable components undergo combustion.

The critical thermal runaway acceleration temperature can be reached in several ways: the LIB is inappropriately exposed to, or operated irresponsibly in a manner that produces a high-temperature environment for a prolonged period of time; the LIB is overcharged to excessive voltage causing the battery materials to undergo exothermic breakdown; or the LIB experiences a short circuit failure causing joule heat to accrue within the cell upon uncontrolled discharge. Upon reaching the critical acceleration temperature during the first stage of decomposition, between ~110 ^{o}C and ~150 ^{o}C, the temperature may increase to more than 500 ^{o}C in a matter of seconds [20].

1.2.2 Short circuit formation in collisions

In EVs, thermal runaway caused by overheating or overcharge is generally of minor concern as healthy, safe temperature and voltage are maintained throughout the pack using onboard computer-operated battery management and thermal management systems [21,22]. However, short circuit failure is a serious threat as vehicle collisions are unpredictable, and mechanical damage to the battery pack can allow the formation of unmanaged, low-resistance electrical pathways for energy to rapidly discharge stored energy [23].

Without a resistive load to accept discharging energy as electricity, the stored energy is instead dissipated as joule heat, causing temperature to quickly rise, eventually producing the conditions for thermal runaway to occur [24]. In addition to the exothermic decomposition events, joule heat continues to accrue from the short circuit, making this type of failure particularly dangerous. If a single LIB cell experiences thermal runaway, adjacent cells may experience thermal runaway upon exposure to high temperature of the first cell, affecting more cells thereafter, gradually cascading through the modules [25]. Such an event would engulf the entire battery pack in fire, as seen following the Tesla Model S impact events.

1.3 LIB safety features for EVs

1.3.1 Primary protection structures and failsafe features

The most straightforward way to avoid thermal runaway is to prevent a short circuit from forming in the first place. Just as the vehicle structure is traditionally designed to absorb impact energy in a crash to dampen abusive acceleration or deceleration forces experienced by vehicle occupants, the EV's structure is the first line of defense against a short circuit event in the LIB cells. Like the vehicle occupants, the battery pack is typically placed in the center of the vehicle [26], between energy dampening crumple zones in the front and back [27]. The pack may be placed within a deformable chassis [28], or the LIB modules may be arranged to tolerate a degree of deformation [29], minimizing the reaction force experienced by the individual LIB cells. In some cases, the pack may even be considered as energy absorbing element to protect the driver [30].

Planning for potential accidents based on likelihood and severity, informed design choices minimize overall risk.

If the primary protection structures are insufficient, there are three main strategies for mitigating thermal runaway upon shorting: joule heat generation can be curbed by hindering ion or electron transport between the electrodes; combustion and explosion can be avoided by preventing the realization of conditions where electrolyte can flash; or temperature accruement can be limited through management of heat generated. Thermal runaway mitigation technologies exist to address these phenomena at the LIB cell, module, and pack levels [31].

1.3.2 Shutdown additives

Technologies for hindering ion transport primarily exist at the cell level. They typically involve an element not inherent to the battery for the purpose of electrochemical functionality, known as a shutdown additive [31–33]. Shutdown additives most commonly attempt to address heat generation by increasing ionic resistivity in the free electrolyte or at an electrode-electrolyte interface. The shutdown mechanisms of these additives typically activate once a LIB cell reaches a predetermined, elevated temperature value or range. Many different additives have been tested, yielding varying degrees of success in preventing thermal runaway.

Reaction agent additives actively attack specific electrochemical components to increase resistivity in unique ways. Xia et al. have shown that by loading common 1M $LiPF_6$, ethylene carbonate (EC), dimethyl carbonate (DMC), ethyl methyl carbonate (EMC) (EC:DMC:EMC 1:1:1 v:v:v) electrolyte with 3 wt.% 1,1'-(methylenedi-4,1-phenylene) bismaleimide monomer and 2,2'-azo-bis-iso-butyronitrile polymerization initiator, the solution will solidify upon reaching 110^{o}C,

preventing further ion transport [34]. Ziegler-Natta catalysts have been placed in semi-solid electrolyte frameworks such that polymerization of cyclic carbonate electrolyte solvents will occur at 90^{o}C [35]. Polyvinylidene fluoride-hexafluoropropylene based gel-electrolytes impregnated with polyethylene glycol dimethacrylate oligomers have been employed such that the oligomers cross-link upon heating to 100^{o}C, increasing viscosity [36]. Zhang discusses several additional examples, but the majority have not been proven in mechanical abuse testing, and often come at some expense to long-term electrochemical stability or day-to-day functionality [33].

Blocking agent additives are used to address ion transport through separators and at electrode-electrolyte interfaces. Shutdown separators are made of multiple layers where at least one layer is made up of a material with a melting temperature or glass transition temperature lower than the others. Upon heating, the layer which responds to the lower temperature melts or deforms to close the pores of the separator, such that ions can no longer travel through them [37,38]. This type of separator often employs a polypropylene-polyethylene-polypropylene trilayer configuration, which are common in commercially-available LIB cells [39]. They are effective against mild short circuits but in the event major damage occurs, the temperature may quickly rise past the shutdown temperature to the failure temperature where the entire separator melts, rendering it ineffective. Following the same principle, Baginska et al. have shown that polyethylene microspheres can be coated onto the separator or paraffin microspheres can be placed in the composite electrode matrix, such that they melt upon heating, coating the surface of the separator or electrode with a non-conductive layer impermeable to the ions [40]. In the event these technologies fail to respond quickly and effectively, they may make the situation worse.

1.3.3 Fire-retardants

Some engineers seek to address the flammability of the organic carbonate electrolyte solvents, rather than attempt to throttle the powerful heating kinetics of a short circuit failure. This usually involves placing fire-retardant additive in the electrolyte that either forms a physical charred layer, separating the volatile liquid from its flammable gas, or acts as a radical scavenger, terminating the chain reaction of the combustion process [33]. These additives are usually organic phosphate compounds, taken and modified from technologies serving other fields beset with fire hazards.

Xu et al. extensively studied fire-retardant additives in the early 2000's. They found that while non-flammable alkyl phosphates are not effective fire-retardants [41], some fluorinated alkyl phosphates such as tris(2,2,2-trifluoroethyl) phosphate can render 1M $LiPF_6$ EC:EMC (1:1 w:w) electrolyte non-flammable at 20 vol.% [42]. Li et al. later found that bis(2-methoxyethoxy)methylallylphosphonate can render 1M $LiPF_6$ EC:DMC (1:1 v:v) non-flammable at 10 vol% [43]. There is also considerable interest in replacing the flammable carbonates altogether. For instance, methylcarbonate terminated perfluoropolyethers solvate fluorinated anions stable at voltages up to 4.2 V, and are completely non-flammable [44]. These approaches come at sacrifice to ionic conductivity of the electrolyte which limits rate capability and low temperature performance. Alternatively, aqueous electrolytes would solve the thermal runaway problem as they are inherently non-flammable, but their voltage window is limited and they often have problems with long-term stability [45,46].

1.3.4 Encapsulation of shutdown additives and fire-retardants

Deploying shutdown additives and fire-retardant additives directly into the LIB environment demands compromises to both normal electrochemical performance and the degree of safety which the additive is capable of imparting. Engineers address this issue by encapsulating the additives in inert materials, such that they do not interact with the electrochemical system until a triggering event occurs. This idea dates back to before the commercialization of the LIB, addressing thermal runaway in energy storage chemistries of the previous generation [47]. Such additive containing capsules are typically designed to melt at a predetermined temperature, but some can also decompose under high voltage in the event of overcharging [48]. By using these techniques, shutdown and fire-retardant additives can be employed without considering the constraint of their effects on everyday performance.

1.3.5 Module and pack level temperature and fire suppression

At the module and pack levels, EV manufacturers generally try to limit accrued temperature by managing the heat generated rather than stopping it altogether. Fans and liquid cooling structures are used to maintain the health of the battery during day-to-day operation, but cannot be relied on to cool the batteries or prevent propagation of thermal runaway to adjacent cells in a shorting event. Emergency temperature management approaches commonly utilize phase change materials in the module structures or deploys low temperature refrigerants through the battery pack using specially designed thermal management systems.

A multiplicity of batteries may be placed in modules made up of low melting point or low boiling point phase change materials which absorb large quantities of latent heat under isothermal conditions upon phase change. Such modules have been made using paraffin and hydrogel [49,50]. Specially designed cooling systems using pressurized refrigerants have been developed by Tesla and General Motors to flood the battery pack enclosure with low temperature, non-flammable gases, which actively cool the batteries and suffocate the system, removing any flammable gas and oxygen capable of supporting a flame [51,52]. These systems are both thermally responsive and can be triggered by onboard computer or sensor signals. Their major drawback is that they can be quite heavy.

1.4 Safety-first design approach to long-range EVs

1.4.1 Significance of LIB safety on EV mass

Battery health and safety considerations incur consequential mass additions to EV systems, which hinder their range capabilities. For instance, the Tesla Model S manages and protects 7104 Panasonic NCR18650B LIB cell units in its 85 kWh battery pack, each with a rated energy density of 243 Wh/kg [53]. The LIB cells are arranged into 16 modules [54], outfitted with primary protection structures, thermal management components, monitoring sensors, operational hardware, and failsafe features, altogether weighing 540 kg. Only 350 kg of the LIB pack's mass are energy-storing cell units. The remaining 190 kg are dedicated to ensure proper day-to-day operation and resilience against catastrophic short circuit failure in an unforeseen event, representing about 9% of the vehicle's total mass [55].

Light-weighting of EVs with improved safety features is a straightforward approach to increase the maximum drive range for a given charge. It is envisioned that if the LIB could be made inherently safe, redundant heavy protection components could be removed or replaced with additional LIB cells. If a sufficient safety margin is achieved, the pack could even be integrated into the vehicle frame or body, assisting the structural needs of the vehicle to cut additional weight, increasing the drive range through a multifunctionality [56].

The viability of the safety-first design approach to extend EV range is contingent upon the resilience of the LIB in abusive events and the vehicle's tolerance of risks characteristic of the LIB's energy-dense, flammable chemistry. Furthermore, the safety features themselves need to be lightweight to yield range-extending implementation.

1.4.2 Addressing short circuit failures immediately upon impact

There is currently a technological gap in development between primary protection structures and the thermally-triggered failsafe features employed in today's EV LIB systems. If the primary protection structures fail to prevent a short circuit from forming in an intense collision, the existing failsafe features only begin to take effect at high temperature, close to the thermal runaway acceleration point. Depending on the severity of the short circuit event, attempts to throttle heat generation at high temperatures may be futile, ending the LIB's service in a fiery demise. Next-generation EV LIB systems should be designed with failsafe features that take effect immediately upon shorting, activating upon mechanical impact. Like the primary protection structures and thermal management systems, emergency shutdown strategies should seek to prevent temperature from accruing within LIB cells in the first place, not rely on the dangerous

conditions produced by the short circuit failure to trigger them. At the very least, new failsafe features should slow the rate of heat generation to manageable levels the existing thermally-activated features can reliably handle.

The energy density of the LIB pack is greatly sacrificed for the sake of safety in collision scenarios. The primary protection structures attempt to prevent short circuit events from ever occurring, but LIB failure cannot always be avoided in certain unpredictable circumstances. Rather than relying on massive primary protection structures to prevent short circuits from ever forming, even under the most extreme conditions, it should be accepted that those events are sometimes inevitable. Focus should instead be given to outfitting LIB cells with failsafe features that make them inherently safe against thermal runaway and fire when a short circuit forms. If new, lightweight technologies can impart a greater margin of safety for EV occupants, heavy protection structures could be removed, and mass-reducing replacements could increase vehicle range.

1.4.3 Developing advanced, light-weight EV safety strategies

Mechanically-activated shutdown technologies should address LIB failure in the earliest stages of the joule heating regime. As existing technologies are thermally-activated, they do not consider the nature of short circuit discharge immediately upon impact. In severe short circuit events in large LIB cells, temperature quickly rises and distributes non-uniformly throughout cells, modules, and packs [57], an expected consequence relied upon to trigger those traditional safety features. Convolution by other exothermic decomposition events associated with thermal runaway make joule heating difficult to examine, so the details of its dynamic evolution during shorting are incomplete as they remain relatively unexplored [58]. Experimental design choices made

specifically to examine those dynamics would elucidate the sequence and importance of previously unidentified or overlooked events, providing a better understanding of how a battery fails. To arrest LIB temperature increase directly in response to a collision event, detailed information about the joule heating regime at low temperatures serve to inform new shutdown strategies and advance failsafe device development.

The rate of joule heating is inversely proportional to the internal resistance of the LIB in a short circuit event. With clarification of the how the internal resistance changes during discharge, and how the different elements of the LIB contribute on which timescales, methods for exacerbating the impedance of relevant components can be devised to slow the heating rate and stop temperature increase prior to realization of the dangerous conditions which facilitate thermal runaway. Considering existing failsafe feature designs, and those developed for battery chemistries of the previous generation, modifications can be made to make them impact-responsive and effective at low temperatures. Recognizing opportunities for the existing support elements of the LIB pack infrastructure to act as safety features, next generation EVs could increase safety margins with multifunctional devices that do not add mass to the vehicle. This narrative considers safety challenges with newly-attained knowledge about the joule heating regime from a unique perspective, serving to aid in developing novel approaches for improving EV safety and increasing vehicle range.

1.5 Outline of thesis

The Chapter 1 introduction informs the importance of LIB safety, describes the current state of EV development, and enumerates some of the challenges to personal vehicle market

penetration. The background of failsafe features currently developed for EVs is given to share the motivation behind the experimental analysis of the short circuit joule heating regime, which is used to aid in development of advanced failsafe features capable of addressing mechanically-induced LIB failure in EV collisions.

In Chapter 2, the internal resistance and electrolyte polarization dynamics of a LIB operated under stressful discharge conditions are examined experimentally using a coin cell system selected specifically to study joule heating. The findings are used to explain the nature of the joule heating events demonstrated in external short circuit and nail penetration testing, and predict how the LIB cell might respond if different resistive elements are manipulated. Further discussion suggests ideas for thermal runaway mitigation strategies which address LIB failure in its earliest stages, two of which are selected for examination in the subsequent chapters.

In Chapter 3, aggressive electrolyte poisoning agents are identified to curb the rate of short circuit joule heating and shutdown a LIB in an emergency situation. A unique testing system is developed to facilitate efficient vetting of candidate poisons. Several successful examples are discussed in terms of the experimentally derived short circuit discharge and electrolyte conductivity model presented in the previous chapter. Potential multifunctional fluid formulations are identified for further investigation of active shutdown systems in EVs.

In Chapter 4, the electrochemical, mechanical, and safety characteristics of thick electrodes employing porous metal current collectors are tested. A high-density slurry processing procedure is disclosed to enable ultra-high aerial capacity electrodes for direct comparison with commercially-produced LIB cells. Various abuse testing characteristics are shown supporting the experimental analysis of short circuit joule heating, and its implications for safe-cell technological design.

Chapter 5 summarizes the information presented in this thesis and discusses future research topics for this line of work.

Chapter 2 Internal resistance and polarization dynamics of lithium-ion batteries upon internal shorting

2.1 Introduction

Lithium-ion batteries (LIB) carry safety risks inherent to their energy-dense chemistries and flammable components, which are of notable concern due to complications associated with thermal runaway [32,59]. LIB safety is particularly important for cells and modules in electric vehicles, which are prone to physical abuse in collision events [10,23]. When short circuit joule heating causes temperature to accrue to a critical point between 110 ^{o}C and 150 ^{o}C in high capacity cells [19], cascading exothermic electrochemical reactions and chemical decompositions compound to accelerate temperature increase, which can reach more than 500 ^{o}C in a matter of seconds [20]. These conditions lead to electrolyte ignition and possibly unit explosion [60]. Reported battery failures have gained the attention of both academic and industrial researchers to identify the causes, and to understand the progression of events that beset thermal runaway. These objectives serve to minimize risk by informing responsible day-to-day operation and aiding in development of effective failsafe technologies [31,61].

Risks associated with joule heating and electrochemical degradation during normal operation are well controlled in electric vehicles. Intelligent battery management system (BMS) algorithms [21,62] coupled with efficient battery thermal management system (BTMS) designs [22,63,64] ensure that the temperature throughout battery pack is maintained in a suitable temperature range below 40 ^{o}C at all times. Additionally, the state of health is constantly monitored by the onboard computer system [65,66], which identifies any hazardous conditions to be

addressed [67]. As a result, thermal runaway is of minor concern under normal operating conditions. However, vehicles may still catch fire in accidents if the battery pack is physically damaged. Collisions can cause the formation of short circuit discharge pathways which the BMS cannot control, nor the BTMS can manage. The battery pack is afforded extensive protection to minimize the possibility and extent of damage, but it is acknowledged that unmitigated damage may still take place in certain circumstances [23,61].

The exothermic decomposition events encompassing thermal runaway have been extensively studied [19,20]. By understanding the nature of how heat generation accelerates as temperature rises, thermal runaway mitigation technologies can be incorporated within the cells and modules to halt temperature increase, and specialized battery materials can be employed to tolerate excessive temperature [61]. Most failsafe features are thermally triggered, taking effect at a specific temperature above the normal LIB operating range (>80 ^{o}C), but below the critical acceleration point (<150 ^{o}C) [31,34,36,40,49,68–73]. They typically involve phase change materials or positive temperature coefficient materials that slow down temperature increase upon activation. Such technologies are capable of handling short circuits of moderate power, but may fail to manage severe short circuits in large-format LIB cells. In the event of a vehicle crash, it is preferable that LIBs have inherent failsafe features that take effect in the joule heating regime, irrespective of temperature and immediately upon shorting, but work in this area is uncommon [74–77].

In severe short circuit scenarios, joule heating dynamics are dictated by the internal resistance of the LIB cell [24,57,78]. The sum of the resistive contributions from a multitude of internal components limit the discharge current and consequent temperature increase [58,79], which in turn alters the resistance of those components in various ways. The resistive influence of

fast kinetic processes manifest rapidly. Those processes include charge transfer between the electrode and electrolyte, as well as electron movement through the composite electrode and across current collector interfaces [80]. Resistive effects of slower processes, like charge-carrying ion diffusion in electrolyte and solid-state ion diffusion within active electrode particles, become apparent on longer timescales [81]. Initially, the resistive kinetic contributions are more significant, such that the short circuit is ohmically-controlled, but as time progresses and resistive diffusion phenomena become dominant, the aggressive discharge transitions to be polarization-controlled. Surveying those resistive phenomena in the diverse network of sensitive materials organized in unwieldy and inaccessible arrangements within an LIB cell is difficult, particularly when engaged in fast, dynamic electrochemical and chemical processes [78,82].

Many experimental studies concerning severe short circuit failure have been performed on large-format LIB cells [25,58,78,79,83–86]. These tests produce fast temperature increases that often result in fire or explosion. Such study is critical to understanding the dangerous heat transfer propagation characteristics within cells and through modules. However, they do not offer systematic information concerning the fundamental joule heating dynamics that seed the energy to trigger all the other undesirable energetic phenomena.

Large-format LIB cells impose challenges to in-situ determination of the resistive contributions from individual components, as well as the progression of events which might alter their significance to the resultant current, as short circuit discharge proceeds. Their short circuit dynamics are aggressive to the point where measurements of joule heating are convoluted by other exothermic decomposition phenomena and nonuniform conduction [57]. Information on the dynamics of how internal resistance changes during the shorting process to define the joule heating rate in the early stages of shorting are limited to computational simulations, which are challenging

to verify experimentally [24,57,58,79]. Development of experimental methods to examine the resistive dynamics of LIB cells under shorting conditions is critical to informing LIB safety protocols and improving cell safety features [57,58].

The goal of this study is to gain a better understanding of how the internal resistance dynamics of LIB cells influence the initial stages and progression of a short circuit failure induced by severe mechanical abuse. Using experimental methods designed specifically to study the joule heating regime, the nature and influence of those phenomena are analyzed. A framework is discussed for the identification and development of effective thermal runaway mitigation strategies addressing short circuit discharge at its earliest stages, which bridge the gap between primary protection structures and thermally triggered failsafe features.

2.2 Experimental procedure and data processing

2.2.1 Reference cell system

Internal resistance and temperature measurements were taken during abusive discharge and short circuit experiments using LIR2450 format $LiCoO_2$ / graphite 120 mAh coin cells, obtained from Xiamen TOB New Energy Technology. The LIR2450 coin cells were chosen as the reference system specifically to investigate the joule heating regime. When severely abused, their current capacity was sufficient to produce consequential cell temperature increase up to 100 ^{o}C. Such temperature accruement was measured over a resolute timescale on the order of minutes, without reaching the critical temperature range where decomposition events characteristic of thermal runaway might occur. In this manner, joule heating data measurements were not convoluted by

other exothermic phenomena. Furthermore, the simple geometry of the rigid 304 stainless steel case structure of LIR2450 cell ensured secure electrical and thermal contact within, even during nail penetration experiments. The large mass contribution of the thermally conductive cell case aided in heat generation measurement, which allowed for an assumption of isothermal character when measuring the temperature externally, despite the fact that most heat was generated from its internal components where the temperature might be slightly different.

2.2.2 Direct current internal resistance testing

Internal resistance (R_{int}) dynamics under healthy and abusive applied constant current (I_{app}) discharge conditions were determined through direct current internal resistance (DCIR) analysis using a Neware BTS3000-5V6A Battery Analyzer. The electromotive force (V_{emf}) and terminal voltage (V_{t}) were compared to differentiate the ohmic, primarily electrical resistance and polarization, primarily ionic resistance contributions. The ohmic resistance (R_{o}) was characterized by the instantaneous potential drop upon resistor application, while polarization resistance (R_{p}) collectively described all additional overpotential manifestations as time (t) progressed. DCIR measurements were taken for cells subject to constant current discharge pulses with rates ranging from 0.2 C (24 mA) to 10 C (1200 mA). Cell temperature (T) was simultaneously monitored using a type-K gage-40 thermocouple affixed to the center of the cell case on the cathode side by polyimide tape. Data were sampled once every second.

$$R_{\mathrm{int}}(t) = R_{\mathrm{o}} + R_{\mathrm{p}}(t) \tag{2.1}$$

The LIR2450 cells were preconditioned by cycling twice between 3.0 V and 4.2 V at a constant applied current rate of 0.1 C. The electromotive force was measured by tracking the

terminal voltage from 4.2 V during the second discharge cycle, as a function of charged current capacity (Q) [87]:

$$V_{\mathrm{emf}}(Q) = V_{\mathrm{t}}\left(Q, I_{\mathrm{app}} = 0.1\ \mathrm{C}\right) \tag{2.2}$$

The obtained data were used to assess how the electromotive force changes with the state of charge (SOC) [88]:

$$Q(t) = Q(t=0) - I_{\mathrm{app}} t \tag{2.3}$$

DCIR tests were performed by applying constant current discharge pulses at various applied current rates on 2-minute intervals. For each test, the cell was charged at 0.1 C to the starting potential of 4.0 V and allowed to rest for 1 hour, ensuring stable open circuit voltage prior to discharge. The ohmic resistance was calculated from the initial potential drop based on the first voltage measurement made upon discharge initiation, sampled at 1 second after external resistor application [66,89–91]:

$$R_{\mathrm{o}} = \frac{V_{\mathrm{emf}}(t=0) - V_{\mathrm{t}}(t=1\mathrm{s})}{I_{\mathrm{app}}} \tag{2.4}$$

The dynamic polarization resistance was measured as discharge progressed with respect to terminal voltage deviations from the electromotive force, accounting for the ohmic resistance bias:

$$R_{\mathrm{p}}(t) = \frac{V_{\mathrm{emf}}\left(Q(t)\right) - V_{\mathrm{t}}(t)}{I_{\mathrm{app}}} - R_{\mathrm{o}} \tag{2.5}$$

Ohmic resistance was assumed constant for the testing duration while polarization resistance was differentiated.

The 4.0 V starting potential of the DCIR measurement was selected in recognizing the influence of SOC on charge transfer resistance and other kinetic processes. Those kinetic phenomena are notably more resistive when a cell is fully charged or discharged, but relatively constant between 30% and 80% SOC [81,90]. Furthermore, the electromotive force was measured

at a rather slow discharge rate, such that the ohmic overpotential bias is low and any minor polarization disturbances incurred would have ample time to develop and reach steady-state by 4.0 V, where it is compared with the terminal voltage [91]. The 2-minute measurement period was selected to capture expected non-linearities in polarization resistance and produce consequential joule heat generation at abusive discharge rates for analysis over resolute temperature and time scales, while remaining within this described SOC range for the entire duration of all DCIR experiments.

2.2.3 External shorting and nail penetration testing

The short circuit responses of the LIB cells were tested externally via constant resistance discharge in a similar manner to the constant current tests, as well as internally via nail penetration. In both cases, the LIB cells were preconditioned by cycling twice between 3.0 V and 4.2 V at a rate of 0.1 C, tracking the electromotive force in terms of charged current capacity during the second discharge cycle. They were then fully charged to 4.2 V and allowed to rest for 1 hour prior to short circuit initiation.

External shorting was performed using the BTS3000-5V6A Battery Analyzer, in which the positive and negative terminals of the cell were connected by a 110 mΩ resistor (R_{ext}) for a 2-minute period. The short circuit current response (I_{sc}) was measured directly using the analyzer.

Internal shorting was induced by driving a stainless steel nail (3.8 mm diameter, 50 mm long) through the cell at its center point using a drill press. In the absence of directly measured terminal voltage and current data, the short circuit current response was calculated indirectly. Without an external resistor to accept energy upon discharge, all current moves through the internal

components of the cell, which act as the only resistors in the circuit such that all stored energy is discharged as joule heat. The power of the discharge is driven by the entire electromotive force of the cell and the short circuit current allowed by its internal resistance, which dictates the rate of joule heat generation ($\dot{q}_{\mathrm{gen}}$). Hence, the rate of joule heat generation can be estimated through analysis of the dynamic temperature response and compared with the electromotive force, in order to determine the short circuit current [20,85]:

$$I_{\mathrm{sc}}(t) = \frac{\dot{q}_{\mathrm{gen}}(t)}{V_{\mathrm{emf}}(Q(t))} \tag{2.6}$$

Changes to electromotive force as a function of temperature were not considered in this calculation.

Prior to shorting via nail penetration, the charged cells were secured to a 12 mm thick polyurethane base holder using masking tape. The assembly was fastened to the drill press in order to facilitate quick nail penetration through the center point, without any lateral movement or large cell deformation. A type-K gage-40 thermocouple was affixed 6 mm from the center of the cell on the cathode side and temperature response was measured over a 20-minute period. Details of the joule heat generation rate calculation are given in Section 2.2.4.

The ohmic resistance and dynamic polarization resistance responses of the cells were determined by comparing short circuit currents with the electromotive force, accounting for bias of the applied resistor in the external shorting scenario [85,91]:

$$R_{\mathrm{o}} = \frac{V_{\mathrm{emf}}(t=0)}{I_{\mathrm{sc}}(t=1\mathrm{s})} \tag{2.7}$$

$$R_{\mathrm{p}}(t) = \frac{V_{\mathrm{emf}}(Q(t))}{I_{\mathrm{sc}}(t)} - R_{\mathrm{o}} - R_{\mathrm{ext}} \tag{2.8}$$

The depth of discharge was tracked with reference to the short circuit current, so as to distinguish how the electromotive force changes as time progresses [88]:

$$Q(t) = Q(t = 0) - \int_{t=0}^{t} I_{\mathrm{sc}}(t)\mathrm{d}t \tag{2.9}$$

Data were sampled for the short circuit experiments once every second.

The fully charged, 4.2 V starting potential for the short circuit tests was selected to produce the largest temperature signal possible, for analysis of the most severe scenarios. The anticipated degree of polarization is well in excess of any minor polarization disturbances incurred in the 0.1 C electromotive force measurements. Moreover, the SOC undergoes large variations upon shorting.

2.2.4 Determining heat transfer characteristics

A convective heat transfer relation was employed to correlate joule heat to the temperature response, taking into consideration the contributions of the heat generation rate and the heat dissipation rate ($\dot{q}_{\mathrm{dis}}$) to the net heating / cooling rate ($\dot{q}_{\mathrm{net}}$) of the cell [92,93]:

$$\dot{q}_{\mathrm{net}}(t) = \dot{q}_{\mathrm{gen}}(t) - \dot{q}_{\mathrm{dis}}(t) \tag{2.10}$$

The net heating / cooling rate reflected in the rate at which the cell temperature changes, is related to the cell mass (m) and the effective system heat capacity (c_{p}):

$$\dot{q}_{\mathrm{net}}(t) = mc_{\mathrm{p}}\frac{\mathrm{d}T(t)}{\mathrm{d}t} \tag{2.11}$$

The heat generation rate is coupled to the measured current (I_{x} representing I_{app} or I_{sc} where appropriate) and the internal resistance [20,85]:

$$\dot{q}_{\mathrm{gen}}(t) = I_{\mathrm{x}}(t)^2 R_{\mathrm{int}}(t) \tag{2.12}$$

The heat dissipation rate is governed by the magnitude of the difference between cell temperature and ambient temperature (T_0), as well as a heat dissipation frequency coefficient (h^*_{dis}) that reflects the thermal conductivity and external orientation of the system:

$$\dot{q}_{\mathrm{dis}}(t) = mc_{\mathrm{p}}h^{*}_{\mathrm{dis}}[T(t) - T_0] \tag{2.13}$$

Entropic and radiative heat transfer effects were not considered in this relation.

The heat dissipation frequency coefficient was determined irrespective of the system mass and effective system heat capacity by tracking the cell temperature upon cooling over a 2-minute interval after discharge, when all heat generation was presumed to have stopped [93]:

$$h^{*}_{\mathrm{dis}}(\dot{q}_{\mathrm{gen}} = 0) = -\ln\left[\frac{T(t)-T_0}{T(t_{\mathrm{ini}})-T_0}\right] / [t - t_{\mathrm{ini}}] \tag{2.14}$$

The initial time of the measurement interval (t_{ini}) for the DCIR testing scenarios was 1 minute after induced discharge had ceased. This interval was chosen to avoid any interference from heat of mixing effects within the electrolyte as it recovered from polarization during the initial relaxation period [82,93], but while measured temperature was sufficiently different from the ambient temperature to produce a resolute, dynamic cooling signal.

After the cell mass was identified using a Fischer Scientific Analytical Balance and the heat dissipation frequency coefficient was known, the effective system heat capacity could be deduced. The value was determined based on the proportionality between the total joule heat generated by the end of the DCIR tests, as calculated from the applied current rates and internal resistances, versus the consequent temperature accruement associated with the joule heating phenomenon, accounting for the heat dissipated from the system mass over the duration of the discharge timeframe:

$$c_{\mathrm{p}} = \left[\int_{t=0\mathrm{s}}^{t=120\mathrm{s}} I^2_{\mathrm{app}} R_{\mathrm{int}}(t)\mathrm{d}t\right] / \left[\int_{t=0\mathrm{s}}^{t=120\mathrm{s}} m\left[\frac{\mathrm{d}T(t)}{\mathrm{d}t} + h^{*}_{\mathrm{dis}}(T(t) - T_0)\right]\mathrm{d}t\right] \tag{2.15}$$

The 6 C, 8 C, and 10 C DCIR scenarios were selected to assess these heat transfer parameters, and the average determined coefficient values were applied for all DCIR data analysis. The lower discharge rate DCIR scenarios were not considered for heat transfer parameter determination, due to the insufficient temperature accruement.

The system mass, effective system heat capacity, and heat dissipation frequency coefficient were different for the nail penetration test. They were recalculated to account for the added mass and altered geometry introduced by the protruding nail, as well as the insulation provided by the polyurethane base holder. The mass of nail was measured using the balance and considered with the cell mass. Furthermore, the effective system heat capacity, as measured from the DCIR tests, was adjusted to account for the additional heat capacity of the 304 stainless steel nail, based on the known specific heat of 304 stainless steel [94]. The 2-minute measurement interval of the heat dissipation frequency coefficient began 10 minutes after the nail penetration was performed. At the selected point in time, all stored energy had been expended and any heat generation had stopped, but a high temperature differential for parameter assessment remained as the cell cooled during the evaluation period.

The testing results used to determine the heat dissipation frequency coefficient and the effective system heat capacity are shown in Section 2.4.1. The determined values of all coefficients used in the heat transfer analyses are summarized in Table 2.1.

Table 2.1 Heat transfer measurement parameters.

Discharge test	m (g)	c_{p} ($\mathrm{J.g^{-1}.K^{-1}}$)	h^{*}_{dis}(Hz)
DCIR	4.86	1.4	0.0055
Nail penetration	7.66	1.07	0.0029

2.2.5 Electrolyte conductivity and viscosity measurement

Electrolyte conductivity measurements for $LiPF_6$ salt in ethylene carbonate (EC) / ethyl methyl carbonate (EMC) solvent solutions were made using a Yoke DDS-307A Conductivity Meter at 23 ^{o}C, with the salt concentrations ranging from 0.1 M and 2.37 M. Viscosity dependence

on $LiPF_6$ salt concentration and temperature was determined by testing electrolyte solutions of varied salt concentrations for temperatures ranging from 23 ^oC and 63 ^oC, using an NDJ-9S Digital Rotary Viscometer with a #0 rotor low viscosity adapter. Temperature control was achieved by using a water bath on a hot plate. The electrolyte solutions were prepared by adjusting the molarity of BASF Selectilyte LP50 1 M $LiPF_6$ EC:EMC (1:1 w:w) electrolyte either by dilution with additional EC (Sigma Aldrich #E26258) and EMC (Sigma Aldrich #754935) mixed in 1:1 mass ratio, or dissolution of additional $LiPF_6$ salt (Sigma Aldrich #201146).

2.3 Model development and calibration

2.3.1 Modeling electrolyte conductivity

Ionic conductivity (σ) collectively captures the availability and the mobility of the charge-carrying ions in electrolyte solution. The charge carrier availability is determined by the lithium-ion concentration (C) and the ion mobility is dictated by the permittivity (ε) of solvent and the diffusivity of solvated ions. Valøen and Reimers showed that diffusivity varies strongly with concentration and temperature, expressing that appropriate understanding of how they affect transport dynamics is particularly important when predicting electrolyte performance at high currents, when a cell is prone to consequential self-heating [95]. Recognizing how particles diffuse through liquids at low Reynolds numbers with respect to the Stokes-Einstein relation, considering ion diffusivity dynamics in terms of temperature and fluid viscosity (μ) may assist in anticipating ionic conductivity changes as battery cell temperature increases [96].

Viscosity of carbonate based electrolytes can increase drastically with salt concentration, producing thick, relatively low-conductivity fluids [97,98]. In high molarity solutions this becomes relevant as a cell polarizes and concentration imbalances are induced across the characteristic length of the transport pathway [24,99]. Considering these factors relevant to a cell operating under stress, conductivity is predicted as:

$$\sigma(C,T) = A\left[\frac{CT\varepsilon(T)}{\mu(C,T)}\right] \tag{2.16}$$

where a constant of proportionality (A) describes the magnitude of the electrolyte conductivity.

As viscosity has Arrhenius-type dependence on temperature [98], it is written as:

$$\mu(C,T) = \mu^*(C,T_0)\exp\left[\frac{E_\mathrm{A}(C)}{R}\left(\frac{1}{T}-\frac{1}{T_0}\right)\right] \tag{2.17}$$

where the reference viscosity (μ^*) and the activation energy (E_A) are functions of salt concentration. For a given concentration, the reference viscosity is tabulated at the ambient temperature of 23 ^{o}C and the activation energy relative to the ideal gas constant (R) is determined based on a series of viscosity measurements at 9 temperatures for each of 7 tested concentrations (Figure 2.1). Both the reference viscosity and the activation energy are determined to have exponential dependence on concentration:

$$\mu^*(C,T_0) = \mu_1^*\exp(\mu_2^* C) \tag{2.18}$$

$$E_\mathrm{A}(C) = E_{\mathrm{A},1}\exp(E_{\mathrm{A},2}C) \tag{2.19}$$

where the reported magnitudes of the variables defining exponential dependence (μ_1^*, μ_2^*, $E_{\mathrm{A},1}$, and $E_{\mathrm{A},2}$) are determined empirically.

A linear dependence of permittivity on temperature for the EC:EMC (1:1 w:w) solvent has been previously reported by Hall et. al. [100] as:

$$\varepsilon(T) = \varepsilon_1 - \varepsilon_2 T \tag{2.20}$$

where the reported magnitudes of the variables defining linear dependence (ε_1 and ε_2) are applied directly to the ionic conductivity model.

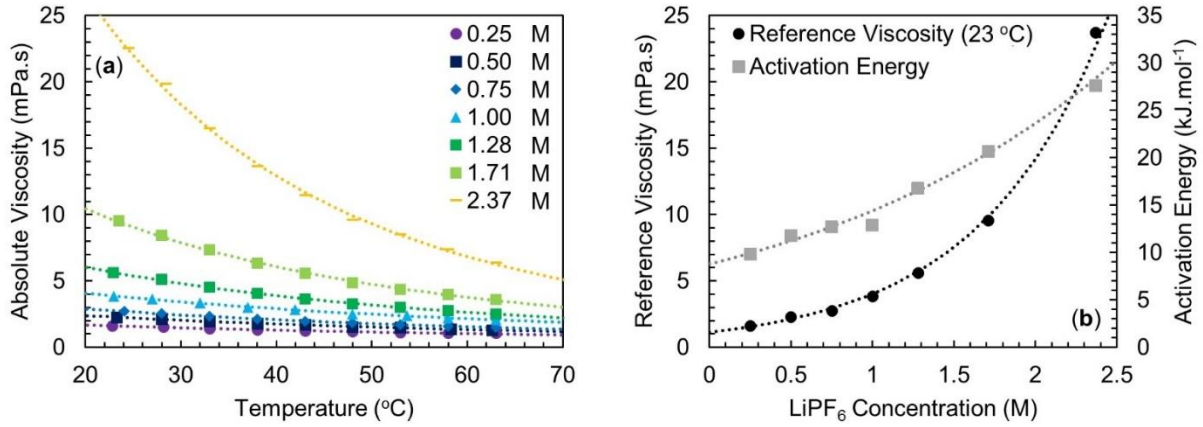


Figure 2.1 (**a**) Measured viscosity (μ) of $LiPF_6$ EC:EMC (1:1 w:w) electrolyte as a function of temperature (T) for salt concentrations (C) from 0.25 M to 2.37 M. (**b**) Fitted Arrhenius-type viscosity parameters (μ^* and E_A) as functions of the salt concentration.

The measured conductivity values are used in calibrating the constant of proportionality so as to provide the best fit relating concentration, temperature, permittivity, and viscosity to the modeled conductivity for the $LiPF_6$ EC:EMC (1:1 w:w) electrolyte system. The measurements also serve to validate the model at 23 °C (Figure 2.2). The values of all coefficients for the conductivity model are summarized in Table 2.2.

Table 2.2 Conductivity relation coefficients for $LiPF_6$ EC:EMC (1:1 w:w) electrolyte and reference parameters for relative electrolyte resistance.

μ_1^* (mPa. s)	μ_2^*(M^{-1})	$E_{A,1}$ (J. mol^{-1})	$E_{A,2}$ (M^{-1})	ε_1	ε_2 (K^{-1})
1.1415	1.2605	8784.5	0.4849	82.61	0.1645
C_0 (M)	T_0 (K)	A (mS·mPa·s·cm^{-1}·M^{-1}·K^{-1})			
1	296.15	0.003737			

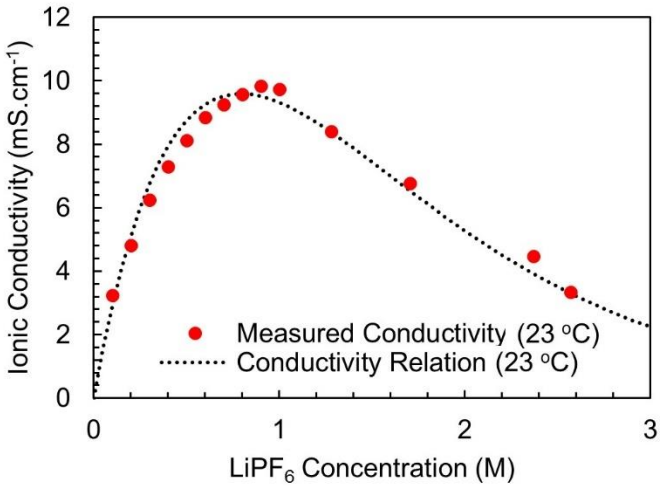


Figure 2.2 Measured and modeled ionic conductivity (σ) of $LiPF_6$ EC:EMC (1:1 w:w) electrolyte as a function of the salt concentration (C) at 23 °C (T_0).

2.3.2 Relating electrolyte and polarization resistance

The determined ionic conductivity model is applied between concentrations of 0 M and 2 M up to 80 °C, and is used to construct a relative electrolyte resistance model for comparison with measured polarization resistances in DCIR and short circuit testing (Figure 2.3). The relative electrolyte resistance (R_{elec}) for given concentration and temperature is related to the nominal resistance of the 1 M $LiPF_6$ initial unpolarized concentration (C_0) at 23 °C as:

$$\frac{R_{\text{elec}}(C,T)}{R_{\text{elec}}(C_0,T_0)} = \frac{\sigma(C_0,T_0)}{\sigma(C,T)} \tag{2.21}$$

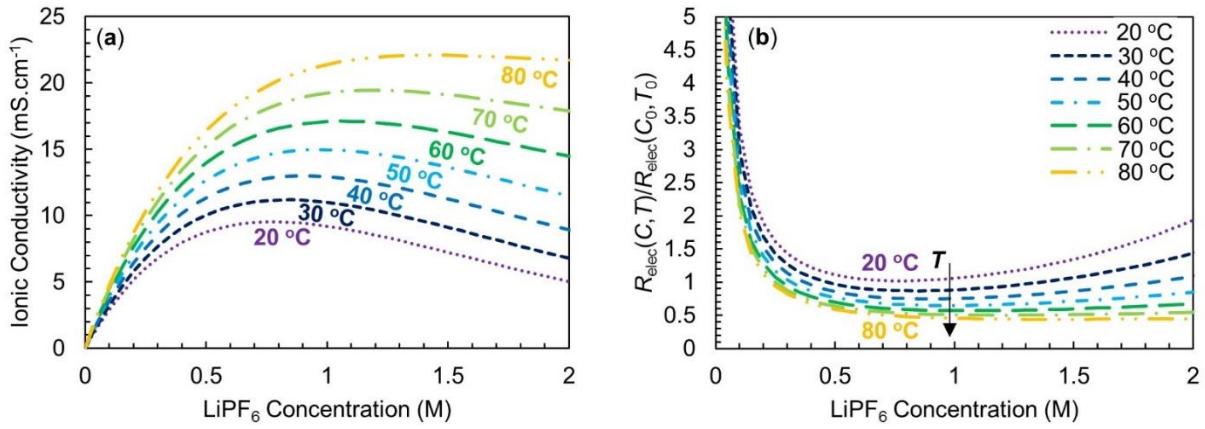


Figure 2.3 (**a**) Modeled ionic conductivity (σ) of $LiPF_6$ EC:EMC (1:1 w:w) electrolyte with respect to the salt concentration (C) and the temperature (T). (**b**) Corresponding modeled electrolyte resistance (R_{elec}) relative to the nominal 1 M $LiPF_6$ reference concentration (C_0) at 23 ^{o}C (T_0).

2.3.3 Ion polarization

The dynamic local average lithium-ion concentrations in electrolyte within the cathode ($\bar{C}_{\mathrm{c}}$), separator ($\bar{C}_{\mathrm{s}}$), and anode regions ($\bar{C}_{\mathrm{a}}$) are determined for the DCIR and short circuit scenarios, considering the measured polarization resistance and cell temperature dynamics. The sum of the resistance contributions from the polarized electrolyte in the three regions ($R_{\mathrm{p,c}}$, $R_{\mathrm{p,s}}$, and $R_{\mathrm{p,a}}$) must equal the polarization resistance measured upon discharge:

$$R_{\mathrm{p}}(t) = \sum_{\mathrm{i=c,s,a}} R_{\mathrm{p,i}}(\bar{C}_{\mathrm{i}}, T, t) \tag{2.22}$$

As electrolyte resistance is proportional to the length which a charge-carrier travels and all three regions exhibit similar porosity, the specific resistances within each region ($r_{\mathrm{p,c}}$, $r_{\mathrm{p,s}}$, and $r_{\mathrm{p,a}}$) are weighted in terms of their individual component thicknesses (δ_{c}, δ_{s}, and δ_{a}), to determine their contributions to the total polarization resistance:

$$R_{\mathrm{p,i}}(\bar{C}_{\mathrm{i}}, T, t) = \left[\frac{\delta_{\mathrm{i}}}{\delta_{\mathrm{c}}+\delta_{\mathrm{s}}+\delta_{\mathrm{a}}}\right] r_{\mathrm{p,i}}(\bar{C}_{\mathrm{i}}, T, t) \tag{2.23}$$

The average concentrations in the electrolyte within the cathode and the anode regions are related to each other, such that lithium-ion species conservation is retained:

$$\delta_{\mathrm{c}}\bar{C}_{\mathrm{c}}(t) + \delta_{\mathrm{a}}\bar{C}_{\mathrm{a}}(t) = [\delta_{\mathrm{c}} + \delta_{\mathrm{a}}]C_0 \tag{2.24}$$

The concentration in the electrolyte within the separator region is considered to be constant:

$$\bar{C}_{\mathrm{s}}(t) = C_0 \tag{2.25}$$

The measured resistance profile of the 0.2 C DCIR test is taken as a reference, representing the nominal electrolyte resistance of an unchanging, 1 M lithium-ion concentration in all three regions at 23 $^{\mathrm{o}}$C for the entire 2-minute testing duration.

For each of the discharge tests, the polarized local average electrolyte concentrations and their corresponding resistance contributions are determined simultaneously using a shooting method. The lithium-ion concentration of electrolyte within the cathode region is varied on an interval of 0.001 M between 0.001 M and 1.0 M at the temperature of the examined moment in time, while the respective ion concentration within the anode region is varied accordingly to maintain the ion species balance. Each set of concentrations are cross-referenced with the formulated relative electrolyte resistance model described in Section 2.3.2. The specific resistances of all three regions are determined based on proportionality to the nominal electrolyte reference:

$$\frac{r_{\mathrm{p,i}}(\bar{C}_{\mathrm{i}},T,t)}{R_{\mathrm{p}}(I_{\mathrm{app}}=0.2\ \mathrm{C},t)} = \frac{R_{\mathrm{elec}}(\bar{C}_{\mathrm{i}},T)}{R_{\mathrm{elec}}(C_0,T_0)} \tag{2.26}$$

The resistance contributions of the polarized electrolyte in each region, weighted by their individual component thicknesses, are totaled and compared with the measured polarization data from the DCIR or short circuit test at the moment of interest. The set of local average concentrations that produce the resistance data which matches the experimentally measured polarization resistance total is identified.

The micrometer measured individual component thicknesses of disassembled cells are summarized in Table 2.3.

Table 2.3 Thicknesses of composite cathode, separator, and composite anode.

δ_c (μm)	δ_s (μm)	δ_a (μm)
70	20	77.5

2.4 Discussion

2.4.1 Results of direct current internal resistance testing

While ohmic resistance is relatively constant regardless of the discharge rate ($R_o = \langle 0.52\ \Omega, 0.72\ \Omega \rangle$), the polarization resistance is variable, becoming increasingly significant as the discharge current increases ($R_p(t = 2\ \text{min}) = \langle 0.59\ \Omega, 3.82\ \Omega \rangle$) (Figure 2.4). Only minor increases in polarization resistance are realized relative to the established reference in the low current discharge regime (1.0 C and below). This is especially true in the first minute following resistor application, where differences in polarization resistance are effectively indistinguishable from the reference. However, notable increases in resistance are observed in the elevated current discharge regime (above 1.0 C). The magnitude becomes larger and the rate of polarization becomes faster as the discharge rate increases.

Unlike in the low current discharge regime, elevated discharge current pulses and internal resistance inefficiencies lead to consequential temperature accruement. The rate at which the measured cell temperature returns towards ambience following the high current DCIR and nail penetration tests shows the frequency of heat dissipation (Figure 2.5). Considering the joule heat

generation rate in terms of applied current and measured resistance dynamics, the effective system heat capacity of the DCIR tested cell systems are determined. The average heat transfer parameter values used in the convective heat transfer model show good agreement with the measured temperature data (Figure 2.6).

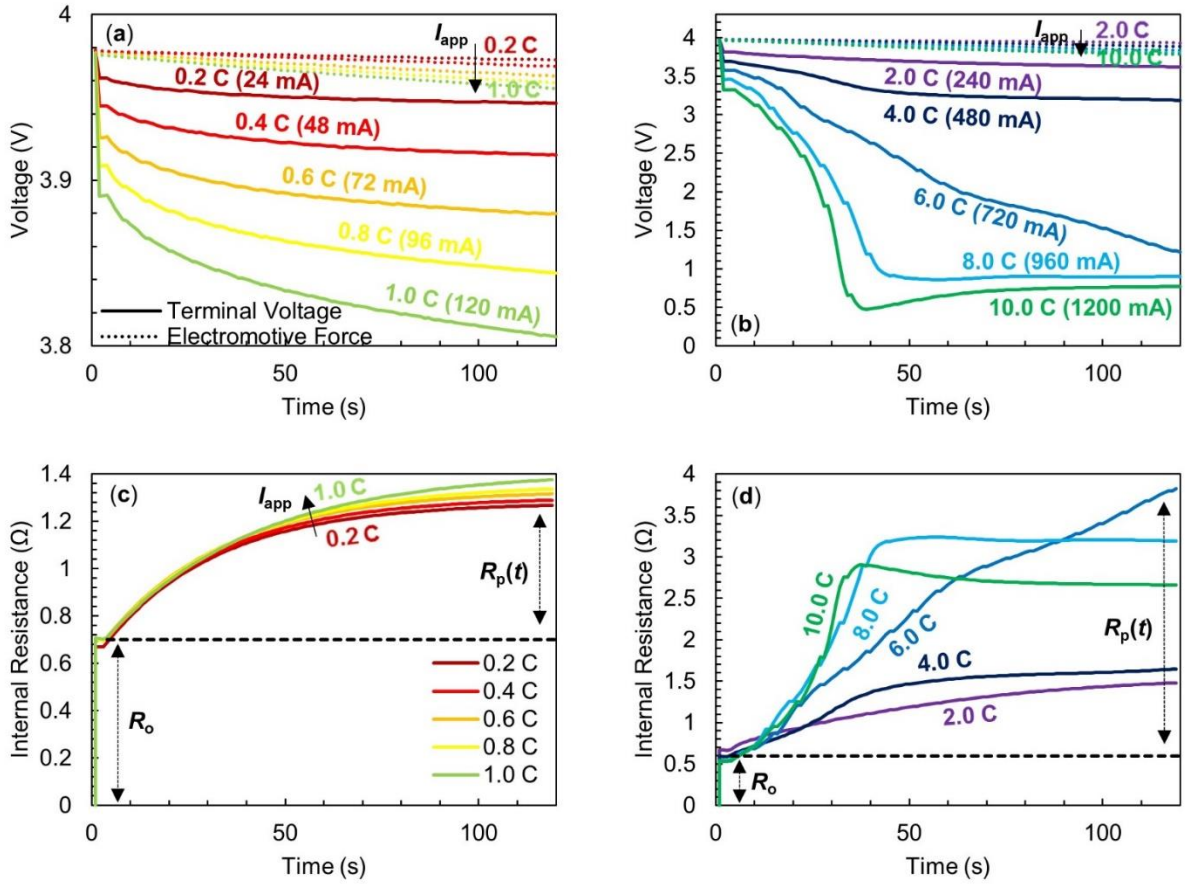


Figure 2.4 (**a**) LIR2450 cell DCIR terminal voltage (V_t) and electromotive force (V_{emf}) responses for low applied current discharge rates (I_{app}) up to 1.0 C and (**b**) elevated applied current discharge rates of 2.0 C to 10.0 C. (**c**) Corresponding ohmic resistances (R_o) and dynamic polarization resistances (R_p) for low current discharge rates and (**d**) elevated current discharge rates measured over time (t).

The ratio between the DCIR polarization resistance measurements and the nominal unpolarized electrolyte resistance profile is cross-referenced with the relative electrolyte resistance model developed for $LiPF_6$ based in EC:EMC (1:1 w:w) solvent, considering the recorded temperature response. The comparison suggests the degree to which average lithium-ion concentration of the electrolyte within the cathode and anode regions deviates from the initial uniform 1 M concentration as cell polarization proceeds.

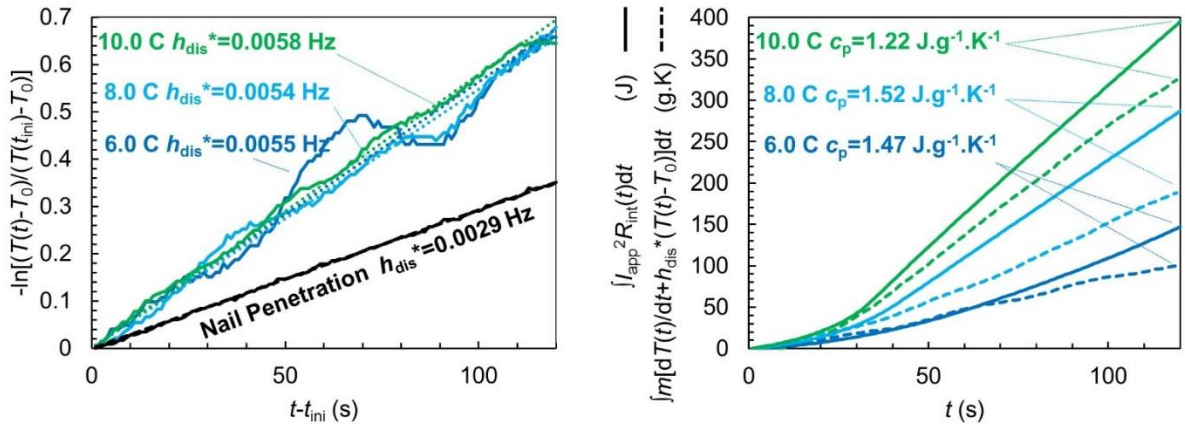


Figure 2.5 (**a**) Heat dissipation frequency coefficients (h^*_{dis}) denoting the magnitude of the slope for the linear fitted curves, determined following DCIR and nail penetration tests as cell temperature (T) cooled towards ambient temperature (T_0) over time (t), beginning at the predetermined evaluation time (t_{ini}). (**b**) System heat capacities (c_p) denoting the ratio between joule heat generated versus the product of cell mass (m) and theoretical temperature accrued without heat dissipation upon DCIR current termination, evaluated in terms of applied current (I_{app}), internal resistance (R_{int}), measured cell temperature, ambient temperature, heat dissipation frequency coefficient, and time. Relevant numerical relations and evaluating methods are enumerated in Section 2.2.4.

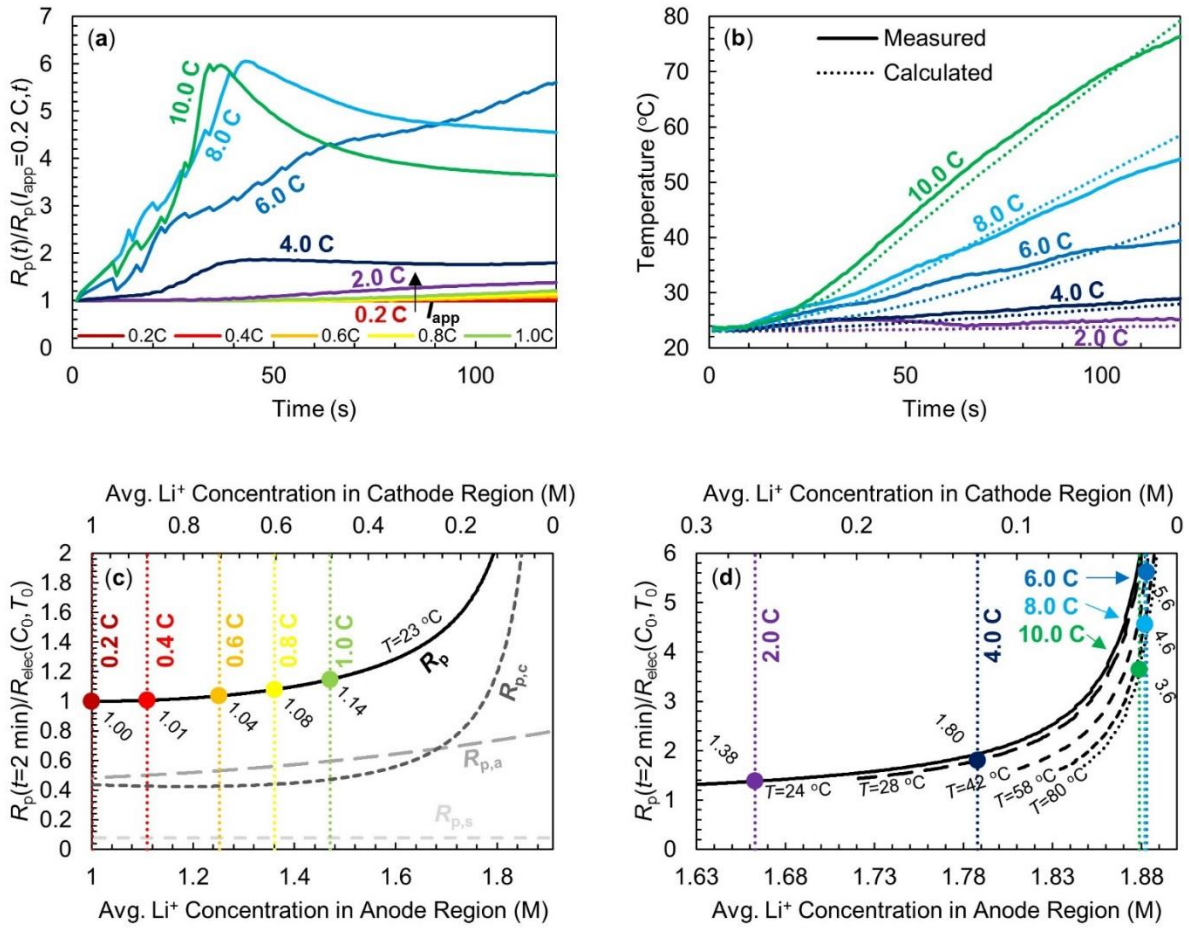


Figure 2.6 (**a**) DCIR dynamic polarization resistance responses (R_p) of LIR2450 cells at low and elevated applied current discharge rates (I_{app}), relative to the assumed 0.2 C unpolarized 1 M electrolyte reference (C_0) profile. (**b**) Corresponding measured cell temperature (T) and calculated cell temperature responses based on the measured DCIR joule heating and heat dissipation rates, using experimentally determined heat transfer parameters applied to the convective heat transfer model described in Section 2.2.4. (**c**) Local average lithium-ion concentrations in the electrolyte within the cathode ($\bar{C}_c$) and anode ($\bar{C}_a$) regions at the end of the 2-minute DCIR tests for low current discharge rates at 23 ºC (T_0), showing resistance contributions of the polarized electrolyte within cathode ($R_{p,c}$), anode ($R_{p,a}$), and separator ($R_{p,s}$) regions. (**d**) Local average lithium-ion concentrations in the electrolyte within the cathode and anode regions at the end of the 2-minute DCIR tests for elevated current discharge rates at their final calculated temperatures, determined by the method described in Section 2.3.3.

2.4.2 Low current discharge regime

Model comparison indicates notable deviations from the initial concentration as polarization occurs in the electrolyte within the cathode and anode regions at low current discharge rates, despite only minor increases in polarization resistance relative to the unpolarized electrolyte reference. As charge-carrying lithium-ions are uptaken from the electrolyte by the cathode, lithium-ions are simultaneously deposited into the electrolyte by the anode. Increasing lithium-ion concentration in the electrolyte within the anode region renders the solution more viscous, curbing ion mobility, which results in polarization resistance increase. Decreasing lithium-ion concentration in the electrolyte within the cathode region also contributes to the resistance increases due to decreased availability to facilitate charge transfer, but consequent reduction in electrolyte viscosity makes the resistive contribution from the cathode region less pronounced. While of the same order of magnitude, ion imbalances in the electrolyte within the anode region has the greatest influence on polarization impedance in the low current discharge regime. Together, resistive contributions from the electrolyte within the cathode and anode regions are no more significant than the ohmic resistance.

2.4.3 Elevated current discharge regime

Drastic increases in polarization resistance occur at elevated discharge rates as rapid, significant deviations from the initial unpolarized electrolyte concentration take place in both the cathode and anode regions of the LIB cell. Upon polarization at rates of 6.0 C and above, the lithium-ion concentration in the electrolyte within the cathode region is just 2% of its initial value

after 2 minutes, which corresponds with a significant increase in concentration within the anode region. Unlike at low currents where this phenomenon would raise the viscosity in the electrolyte within the anode region, the consequent increase in cell temperature curbs the thickening effect. The lithium-ions tend to maintain a relatively high mobility and the conductive electrolyte within the anode region does not contribute notably to the cell resistance. Instead, the imbalance of lithium-ions in electrolyte within the cathode region incurs the most significant contribution to polarization resistance and total internal resistance increases, due to the scarcity of charge-carrying ions within that locality.

Discharging at 10 C, the process of polarization occurs over about 35 seconds, at which time local average ion concentrations stabilize. Prior to polarization, during the first few seconds following resistor application, the ohmic contributions account for almost the entirety of the measured internal resistance. However, upon polarization, the resistive contributions of the electrolyte within the cathode region accounts for more than 90% of the polarization resistance and more than 70% of the total internal resistance (Figure 2.7).

While the ultimate magnitude of the concentration imbalance does not further increase beyond 6.0 C, the rate of polarization becomes quicker, as does the rate of temperature increase. These phenomena are responsible for the nonlinearities of the internal resistance dynamics at elevated discharge rates.

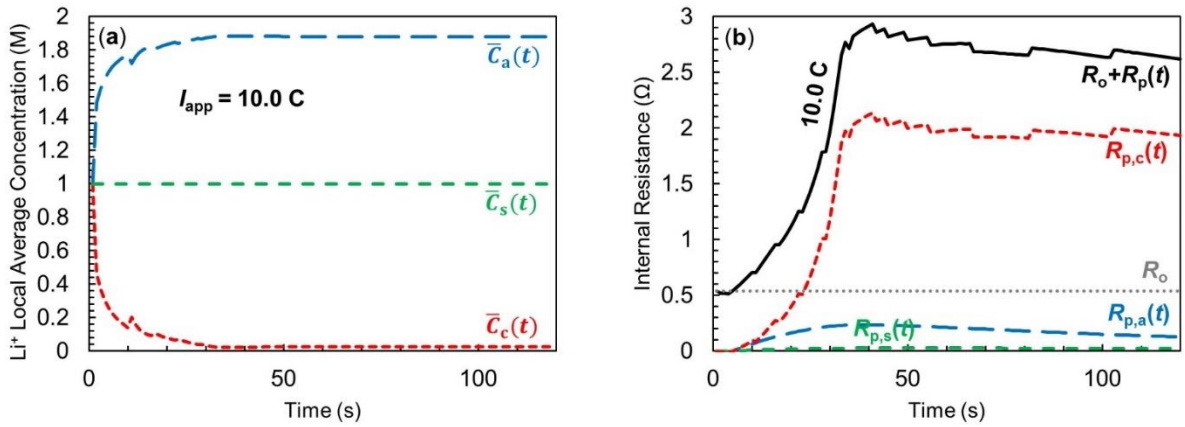


Figure 2.7 (**a**) Local average lithium-ion concentrations in the cathode ($\bar{C}_c$), anode ($\bar{C}_a$), and separator ($\bar{C}_s$) regions for a LIR2450 cell discharged at 10.0 C applied current rate (I_{app}), as a function of time (t). (**b**) Ohmic resistance (R_o), dynamic polarization resistance contributions from the individual regions ($R_{p,c}$, $R_{p,a}$, and $R_{p,s}$), and total polarization resistance (R_p) influences to the measured internal impedance, determined by the method described in Section 2.3.3.

2.4.4 Function and limitations of this interpretation

This study is designed to identify the ohmic and polarization resistance dynamics of LIB cells under abusive discharge conditions using simple experimental methods in order to better inform thermal runaway mitigation strategies addressing the joule heating regime. Ohmic resistances are primarily electrical in nature, while polarization resistances are primarily ionic; but a multitude of complex phenomena contribute to both and their combined influences under extreme conditions are difficult to accurately predict. The combined contributions of all phenomena that manifest as either ohmic or polarization resistances are collectively captured in the DCIR measurements. Further analysis serves to describe the nature of the polarization, which is significant under abusive discharge conditions. The experimental design choices are made to specifically examine individual elements.

Ohmic resistance is assumed to be constant for the duration of the DCIR tests, but charge transfer resistance, which is a major contributing factor, varies with SOC [81]. To minimize any associated error, the tests are started from about 70% SOC and discharged to a minimum of about 40% SOC in the most aggressive DCIR scenario. Within this SOC range, charge transfer resistance is relatively constant so that polarization resistance can be differentiated from the ohmic contribution [90].

The DCIR response of the 0.2 C applied current test over the duration of the 2-minute examination period is selected to represent an unchanging 1 M ion concentration in all three regions, and $LiPF_6$ salt concentration in EC:EMC (1:1 w:w) solvent represents lithium-ion concentration within the cell. These assumptions are necessary to establish a reference for comparison to ascertain information about ion imbalances upon cell polarization. Arora et. al. [99] reported through their computer simulations that when a $LiMn_2O_4$ / graphite, 1 M $LiPF_6$ EC:DMC (2:1 v:v) cell system is subjected to 0.16 C discharge, an average concentration greater than 0.95 M is maintained in the electrolyte within the cathode region after 3 minutes. Furthermore, deviations of local average concentrations from the initial 1 M unity indicated by the analysis are well beyond that of any bias introduced by using the 0.2 C testing reference.

Small increases in polarization resistance suggest large deviations from the initial concentration in the low current regime. The formulated electrolyte resistance model is quite sensitive for concentrations between 0.5 M and 1.45 M, which introduces a degree of uncertainty as to the accuracy of the local average concentration values at low discharge rates. However, the model provides much better resolution outside of this concentration range and the analysis well captures the ion imbalances at elevated current discharge rates, relevant for short circuit considerations.

This experimental analysis is carried out to identify local average ion concentrations. It does not account for local gradients in the individual cathode, separator, or anode regions. Such dynamics may be important, specifically in the electrolyte within the anode region which thickens exponentially with concentration [24,99]. Concentrations greater than the indicated average may accrue near the anode current collector, which could have a consequential contribution to internal resistance. However, as discussed previously, temperature accruement tends to negate concentration induced viscosity increases, and the resistive contribution of the electrolyte in the cathode region at elevated rates is overwhelming.

The polarization resistance analysis does not consider resistive contributions from solid-state ion diffusion in the active materials. The time constant characteristic of ion diffusional impedance development within the electrolyte is on the order of one to ten seconds [81,95], whereas the time constant for solid-state ion diffusional impedance is on the order of several tens to a couple hundred seconds [80,91]. Solid-state diffusional impedance contributes to the resistance measured at the end of the 2-minute DCIR tests to a relatively minor degree, which influences the concentration determinations. Sustained discharge at high rates might also cause particle or interfacial cracking, which could exacerbate resistance as time progresses. However, the polarization resistance increases at high discharge rates occur in the first tens of seconds over the timescale characterized by the electrolyte diffusional impedance time constant, and are a result of ion reallocation across the characteristic length of the transport pathway, which is retained through the duration of the tests.

At high discharge rates, measured internal resistances quickly increase, resulting in consequential joule heating. Through this experimental analysis, it is shown that this is primarily a result of ion depletion from the electrolyte in the cathode region. The models used to make this

determination have limitations, and although the experiments are carefully designed with those limitations in mind, a degree of error persists as a result of the collective sum of assumptions required to perform the analyses. Nonetheless, the experimental data and analyses are valuable to the discussion of resistance and polarization dynamics under extreme discharge conditions, and is critical to the study on short circuit joule heating dynamics and thermal runaway mitigation strategies.

2.4.5 External shorting and nail penetration tests

Unlike during a controlled constant current discharge, where increasing internal resistance and polarization dynamics exacerbate heat generation, internal resistance is discharge rate limiting in short circuit scenarios. Initially dictated by low, ohmic resistances, a short circuit discharge current is expected to be highest at the moment when the short is initiated and decrease as internal polarization proceeds. Heating dynamics proportionally reflect the magnitude of the current, so the LIB cell should respond initially at its maximum possible heating rate and subsequently reduce to a lower rate.

As expected, the measured current and heat generation responses initially peak at their maximum rates. External shorting initially results in a 50 C discharge current and nail penetration results in an 80 C discharge current, both extending a duration of about 3 seconds. Over the next 10 - 15 seconds, discharge rates decrease to and stabilize at about 20 C and 10 C for external shorting and nail penetration, respectively (Figure 2.8). When subjected to dynamic ion allocation analysis, the model comparison indicates a rapid depletion of lithium-ions in electrolyte within the cathode region, settling at 1-3% of the initial uniform concentration after the first 3 seconds. The

rapid uptake of nearly all the lithium-ions results in immediate polarization of the cell. Continued discharge thereafter requires that ions traverse longer distances from the concentrated electrolyte within the anode region to allow for further charge transfer, throttling the short circuit current rate (depicted in Figure 2.9).

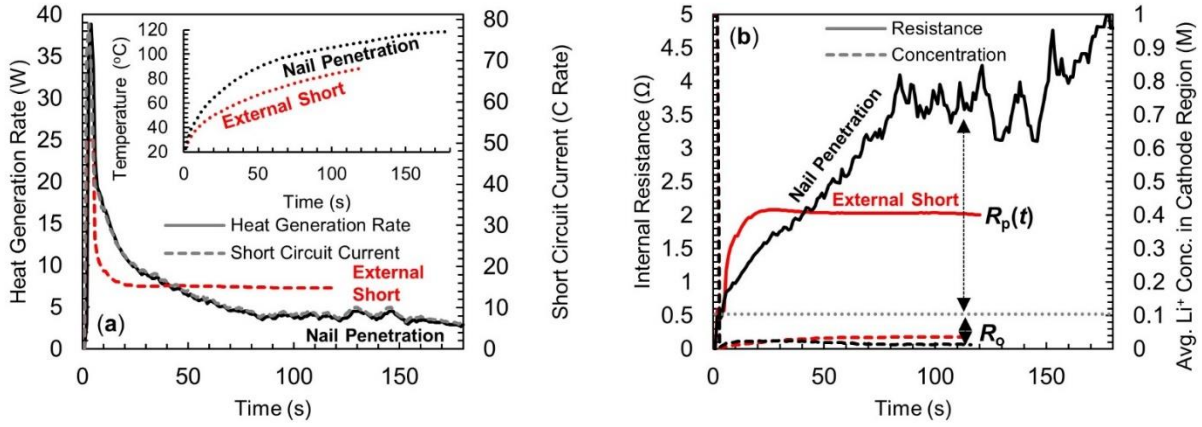


Figure 2.8 (**a**) Heat generation rate ($\dot{q}_{gen}$), discharge current (I_{sc}), and cell temperature (T) responses to external shorting and nail penetration testing of fully charged LIR2450 cells. (**b**) Corresponding ohmic (R_o) and polarization resistances (R_p) applied to the experimentally derived relative electrolyte resistance comparison model for $LiPF_6$ in EC:EMC (1:1 w:w) solvent, showing rapid depletion of lithium-ion concentration in the electrolyte within the cathode region ($\bar{C}_c$) upon abuse, obtained through the procedures described in Section 2.2.3 and Section 2.3.3.

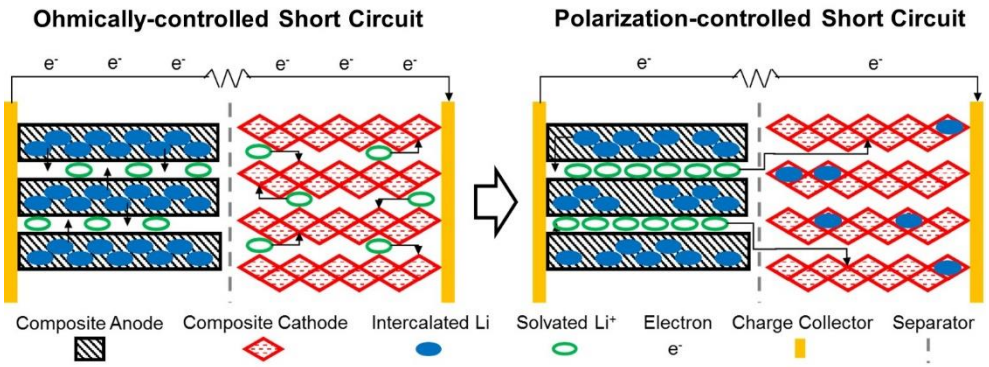


Figure 2.9 Schematic illustrating transition from ohmically-controlled short circuit to polarization controlled short circuit.

The electrically-controlled, capacitive discharge peak occurring during the first 3 seconds reflects 5% - 7% of the total current capacity of the cell. These values align with the quantity of lithium-ions that occupy the electrolyte within the cathode region prior to initiation of the short circuit. Subsequent discharge of the remaining 93% - 95% current capacity is ionically-controlled by the resistance of the ion scarce electrolyte within the cathode region. Differences in the magnitude of the capacitive heating rate and subsequent polarization resistance increase for the different modes of shorting are attributed to the different electrical shorting resistances, which result in variable compounding temperature and discharge rate dynamics. Computational simulations of Zavalis et. al. [24] suggest similar heating rate and polarization dynamics for a $LiNi_{0.8}Co_{0.15}Al_{0.05}O_2$ / graphite, 1.2 M $LiPF_6$ EC:EMC (3:7 w:w) cell system subjected to severe short circuit scenarios.

2.4.6 Implications for thermal runaway mitigation

While cells are designed to have low operational impedance to maximize their rate capability, charge efficiency, and discharge efficiency, raising internal resistance in response to the formation of a short circuit connection is critical to halting temperature increase in the joule heating regime, prior to the onset of cascading exothermic decomposition events. The investigation performed to elucidate joule heating, resistance, and polarization dynamics provides guidance on how to identify thermal runaway mitigation strategies relevant to various heating features and timeframes.

According to the experimental and modeling results, targeting and imparting excess electrical resistances is critical to decreasing the magnitude of the powerful capacitive discharge

feature demonstrated in the initial seconds following short circuit initiation. This is especially important for high capacity cells in which rapid discharge of 5%-7% current capacity may be sufficient to raise temperature to the critical point where thermal runaway accelerates. The timescale of the electrical impedance increase must be fast. Minimizing capacitive discharge heating also helps dampen and delay subsequent conductive contributions incurred by temperature accruement. Electrical resistances contribute relatively little to overall impedance after the capacitive energy has been expended, and are less relevant once the electrolyte has polarized.

Given the immediacy of the capacitive discharge, safety features should be mechanically activated or inherent to the structure of the electrically conductive components. The current collectors and the conductive carbon composite additives are reasonable targets to address this feature, as they provide the least electrically resistive pathways for charge to move between electrodes. Mitigation strategies worthy of investigation include: modification of current collectors as to strategically weaken them, promoting separation of damaged locations from undamaged locations to minimize electrical contact area in an impact event [74]; manipulating conductive carbon morphology to embrittle the electrodes so they easily break apart, limiting electrical contact within the composites when crushed [75]; decreasing conductive carbon loading in the cathode to reduce excessive electrical conductivity that is unneeded to meet functional rate capability requirements; increasing composite electrode thickness to increase electron transport length as well as reduce the possibility of low resistance contact with the counter electrode's current collector [78,79]; to name a few.

Exacerbating ionic resistances is important to halting the continued discharge upon polarization. While polarized-electrolyte-controlled discharge is notably slower than the ohmically-controlled discharge, this regime represents more than 90% of the total current capacity

for a fully charged LIB cell. Given sufficient charged current capacity, this ion-transport-dependent feature of short circuit discharge would heat a higher capacity cell to the critical acceleration temperature of thermal runaway, if the electron-transport-dependent feature does not. The timescale for ionic impedance increase is slightly less constrained than electrical impedance increases, but faster responses are still desirable to throttle the continued heat generation as temperature rises. Ionic resistances incur the most significant contributions to internal resistance upon polarization, and they limit the discharge rate for the major duration of the shorting response.

Considering the electrolyte conductivity model helps to identify different methods for manipulating the electrolyte to exacerbate polarization resistance in order to curb or stop continued joule heating after the capacitive discharge. Given the extreme degree to which concentration is imbalanced upon polarization, it would seem rather difficult to manipulate it further, but forcibly altering the permittivity or viscosity could be viable mitigation approaches. The ion diffusional resistance in electrolyte could be manipulated by: implanting encapsulated poisons within the electrodes or separator, which produce low or zero permittivity regions upon rupture [76]; shear-thickening electrolyte additives, which increase viscosity immediately upon impact prior to temperature increase [77]; less porous anode composites, which restrict ion motion upon polarization; etc.

It is envisioned that, with improved understanding of how joule heating proceeds as well as the significance and nature of the different ohmically-controlled and polarization-controlled discharge features, new techniques may be developed to address short circuit discharge at its earliest stages.

2.4.7 Significance of abuse responsive impedance increases

The predicted increases in electrically-controlled and ionically-controlled resistances immediately in response to short circuit initiation are shown for the LIR2450 cell system examined upon nail penetration (Figure 2.10). Even increasing the resistance two-fold ($2R_{\mathrm{o}}$ and $2R_{\mathrm{p}}(t)$) is consequential to the heating rate and temperature responses. Increasing ohmic resistance has major influence in the first 3 seconds and increasing polarization resistance has a greater degree of influence once the capacitive energy has discharged. The different influences of the electrical and ionic resistive modes are apparent when comparing five-fold increases of ohmic resistances ($5R_{\mathrm{o}}$) and polarization resistances ($5R_{\mathrm{p}}(t)$) independently. While the relative temperature increase is 10 degrees less after 3 seconds in the ohmic increase scenario due to notable suppression of heating associated with capacitive discharge, relative temperature increase is 22 degrees less after 3 minutes for the polarization increase scenario, as the magnitude of the resistance increase is higher for the greater duration of the shorting event.

Heat generation rate in the first 3 seconds following shorting initiation is inversely proportional to the ohmic resistance increase. In all examined cases, the magnitude of increase in polarization resistance supersedes and continues to grow beyond a proportional increase in ohmic resistance, as the dominant resistive force within 8 seconds of short circuit initiation. Hence, increasing ion transport resistance would be more effective in throttling the ultimate accrued temperature, but may offer relatively little benefit in the important first few seconds after the connection is formed. That is not to say electrical resistance increases do not have influence after the capacitive discharge energy has subsided. Ten-fold to twenty-fold increases in electrical resistances ($10R_{\mathrm{o}}$ to $20R_{\mathrm{o}}$) can curb the rate of temperature increase to manageable levels without

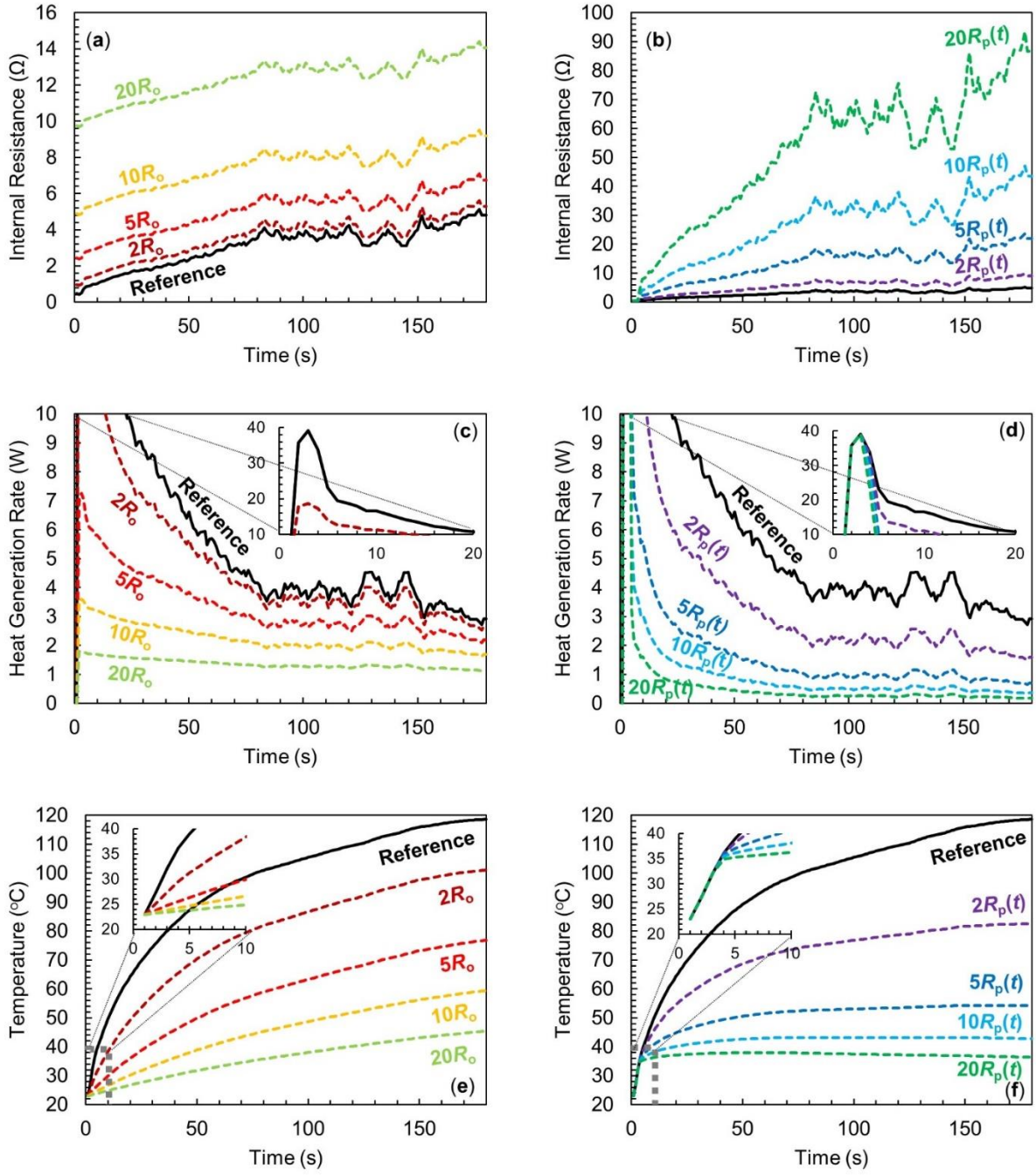


Figure 2.10 Predicted internal impedance, heat generation rate ($\dot{q}_{gen}$), and cell temperature (T) responses of LIR2450 cells upon nail penetration, subjected to: (**a**, **c**, **e**) increased ohmic resistances or (**b**, **d**, **f**) increased polarization resistances by two-fold ($2R_o$, $2R_p(t)$), five-fold ($5R_o$, $5R_p(t)$), ten-fold ($10R_o$, $10R_p(t)$), and twenty-fold ($20R_o$, $20R_p(t)$) relative to the measured reference response.

additionally increasing ionic resistances. By contrast, ten-fold to twenty-fold increases in ionic resistances ($10R_{\mathrm{p}}(t)$ to $20R_{\mathrm{p}}(t)$) may be much less effective in larger cells if the ohmic resistance is sufficiently low and the capacity of lithium-ions initially in the electrolyte within the cathode region is sufficiently large.

The above analyses and understanding should help identify thermal runaway mitigation targets for various safety strategies, and critique their relevance to different stages and timescales of discharge progression. To quickly assess the magnitudes of the ohmic and polarization resistances in higher capacity cells, and to estimate associated joule heating rates experienced upon severe shorting, similar DCIR experiments at high current rates using much shorter pulse durations could be performed to establish a reference for selecting impedance design targets in more dangerous systems. Such analysis is a pragmatic approach for evaluating and improving LIB safety. These considerations will become critical as advances in LIB chemistry yield higher energy densities and new devices demand a greater degree of system integration, leading to faster temperature accruement and leaving a shorter timeframe to address joule heating.

2.5 Concluding remarks

In this study, the internal resistance and polarization dynamics of lithium-ion batteries in the initial stages of a severe short circuit discharge are investigated experimentally, to examine the joule heating regime. Nonlinear resistance, polarization, and joule heating dynamics are identified in direct current internal resistance testing of LIR2450 format $LiCoO_2$ / graphite 120 mAh coin cells at high current discharge rates. The nature of polarization is clarified using an electrolyte resistance comparison model, indicating rapid depletion of lithium-ions from the electrolyte within

the cathode region and consequent temperature accruement are responsible for the nonlinearities. Results are corroborated in external shorting and nail penetration experiments, which reveal a powerful, electrically-controlled, capacitive heating feature immediately upon shorting. Heating is subsequently throttled to lower, ionically-controlled rates as ions quickly transfer to the composite cathode from the electrolyte in the cathode region, leaving the region scarce of ions and relatively resistive.

The prospect of how to address these joule heating features are discussed to support investigation of safe-cell design strategies that take effect in the earliest stages of short circuit discharge. A sensitivity analysis is performed to show how increasing ohmic or polarization resistance would affect the heating rate, as well as their relevance to different timescales. Such analysis could assist in setting impedance exacerbation design targets for cell safety features in the joule heating regime. The information gained serves to help bridge the gap in thermal runaway mitigation technological development between primary protection structures and thermally activated failsafe features.

2.6 Acknowledgements

Chapter 2, in full, is a reprint of the published material as it appears in Applied Energy. Daniel Noelle, Meng Wang, Anh V. Le, Yang Shi, and Yu Qiao., 2018. Internal resistance and polarization dynamics of lithium-ion batteries upon internal shorting. *Appl. Energy, 212, 796-808*. The dissertation author was the primary investigator and first author of the paper.

Chapter 3 Aggressive electrolyte poisons and multifunctional fluids comprised of diols and diamines for emergency shutdown of lithium-ion batteries

3.1 Introduction

Short circuit hazards potentially leading to thermal runaway have plagued energy-dense, flammable lithium-ion battery (LIB) chemistries since their outset [10,32]. In 1978, a patent was awarded for over-temperature battery deactivation with thermally-activated blocking agent and reaction agent poisoning mechanisms, intended to shut down non-rechargeable lithium thionyl chloride batteries in an emergency [47]. Blocking agents, typically chemically-inert phase change materials serving to physically impede ion-transport pathways, and reaction agents, chemicals hostile to the LIB that interfere with electrolyte or electrode function, are employed to slow or halt short circuit discharge and heat generation. Depending on the nature of the poisons, they may be encapsulated in inert materials rigged for release upon thermal activation of the container, or remain inert below a certain threshold temperature; the latter enabling direct incorporation of the agent into the LIB cell.

Various renditions of this shutdown feature concept have emerged to address the dangers of modern, rechargeable LIB chemistries. Uncontained blocking agents have been incorporated in several successful designs [40,69,70], with the trilayer shutdown separator being the most prominent example [101]. Encapsulated poisons have also attracted some interest, with focus primarily given to fire retardants [48,102,103]. These designs are often effective at slowing joule heat generation and preventing electrolyte ignition under short circuit conditions of moderate power, but cannot be relied on to halt increasing temperature prior to reaching the thermal runaway

acceleration point in large LIB cells subject to powerful shorting currents.

Severe LIB shorting failures are of particular concern for electric vehicles and portable electronics prone to physical abuse [32,61]. As such, it is highly desirable that shutdown mechanisms be mechanically-activated to address heat generation in the earliest stages of short circuit progression, irrespective of temperature. Breakable capsules filled with aggressive poisons designed to rupture in an impact event, such as an automobile collision, could fill the gap between primary protection structures and thermally-triggered safety features. However, encapsulated poisoning agents which actively interfere with specific electrochemical components at ambient temperature have received relatively little attention [104].

Halting short circuit discharge by preventing charge-carrying lithium-ions from traversing the electrolyte from the anode to the cathode, where they would normally recombine with charge-carrying electrons to liberate joule heat, is a well-established shutdown strategy. Uncontained blocking agent poisons seek to accomplish this goal, acting at the interface of one of the electrodes [40] or within the free electrolyte [34], upon thermal-activation at high temperatures. Here it is envisioned that a variety of functionally different classifications of encapsulated, aggressive reaction agent and blocking agent poisons could potentially serve to hinder the lithium-ions' transport at low temperatures, if appropriately arranged in the LIB cell for prompt interference in response to a mechanical-activation event. Effective examples might include: solid electrolyte interface promoters, gas generating agents, ionic conductivity disruptors, immiscible fluids, binder dissolution solvents, etc.

The previous investigation into the fundamental nature of short circuit joule heating phenomena revealed that polarized electrolyte resistance is discharge-rate-limiting for more than 90% of the total current capacity of a fully charged LIB cell, implicating the free electrolyte as a

prime target for exacerbating impedance to curb joule heating [105]. The electrolyte resistance model used to make that determination also provides guidance for how to effectively disrupt the ionic conductivity of the electrolyte during a stressful discharge event. Specifically, electrolyte solvent permittivity tends to remain sufficiently high [100] while solution viscosity thins as discharge progresses and temperature accrues [97,98], such that the electrolyte in the anode region remains relatively conductive for the duration of the shorting event. This knowledge is helpful in informing disruption strategies and identifying poisoning candidates which effectively target critical properties on relevant timescales, to safely shut down the battery.

For the proposed safety feature to be viable for implementation, it needs to be lightweight to maintain performance characteristics and avoid sacrificing the energy density of the LIB dependent device. As such, the poisoning agent should be not only aggressive at ambient temperature, but potent so it is effective at low concentrations, or retain other useful properties inherent to fluids in existing LIB infrastructure, modified for multifunctionality. To identify diverse poisoning agent selections for enabling novel shutdown feature designs using this previously uninvestigated strategy, many unexplored potential candidates could undergo vetting.

This study seeks to identify aggressive and potent reaction agent poisons capable of exacerbating electrolyte resistance to safely shut down short circuit discharge, early in the joule heating regime. A unique testing system is developed to probe the competing joule heating and poisoning dynamics in LIB cells upon nail penetration, when agents are introduced to the LIB environment at the moment shorting is initiated, efficiently evaluating the real-time influence of a variety of candidates. In this manner, the expected influence of the agents is predicted for the scenario in which they are encapsulated, remaining inert until rupture of the container in a mechanical-activation event. Upon determining the most effective poisoning options for modern

electrolyte chemistries, further development of advanced shutdown systems can proceed to impart greater safety in LIB devices.

3.2 Experimental methods and data acquisition

3.2.1 Reference cell system

The merits of LIR2450 format $LiCoO_2$ / graphite 120 mAh coin cells for studying short circuit joule heating were demonstrated in the previous study examining the fundamental internal resistance and polarization dynamics in the earliest stages upon nail penetration [105]. The sensitivity analysis performed predicting how exacerbation of polarization resistance would influence joule heating and resultant temperature accruement, is used to set impedance targets for the proposed poisoning strategy, and evaluate the magnitude and timeframe over which an agent increases the effective internal resistance. Additionally, the high mass content and rigid geometry of the cell case promote good thermal contact throughout, as well as consistent specific heat and heat dissipation properties, even with modifications made to facilitate poison evaluation testing. This allows for the reasonable assumption of isothermal character to be maintained, and the previously determined heat transfer parameters enumerated in Section 2.2.4 to be confidently applied for these analyses.

Since the cells tested were purchased in a large quantity from a single commercial manufacturer, Xiamen TOB New Energy Technology, consistency from cell to cell was ensured for accurate comparison of many agent species, with repeated trials. With a few simple, easy-to-make modifications, the cell system demonstrated to be ideal for efficiently and safely vetting a

variety of candidate poisons, intended for encapsulation in breakable containers and multifunctional systems.

3.2.2 Poisoning agent candidate selection and mechanism evaluation

Diols and diamines were selected as the reaction agent poison classifications of interest for this study. Motivations for these choices are presented in the discussion of Section 3.3.1, Section 3.3.2, and Section 3.4.2.

Diol poisons: 1,2-ethanediol, 1,3-propanediol, 1,5-pentanediol; diamine poisons: 1,2-ethanediamine, 1,3-propanediamine; and carbonate solvent components: ethylene carbonate (EC), ethyl methyl carbonate (EMC) were purchased from Sigma Aldrich in their highest available purity. Pristine electrolyte, 1 M $LiPF_6$ EC:EMC (1:1 w:w), was obtained from BASF with Product Code Selectilyte LP50.

Viscosities of pristine electrolyte, diols, and electrolyte / diol mixtures were evaluated over the temperature range of 23 ^{o}C and 63 ^{o}C, using an NDJ-9S Digital Rotary Viscometer with #0 and #1 rotors. Temperature was controlled using a water bath on a hot plate. Ionic conductivity of pristine electrolyte, electrolyte / diol mixtures, and electrolyte / diamine mixtures were determined using a Yoke DDS-307A Conductivity Meter. Solutions of predetermined compositions were vigorously mixed, and conductivity measurements were taken via probe immersion exactly 1 minute after mixing initiation. Reaction temperature for mixtures of EMC, EC:EMC (1:1 w:w), or pristine electrolyte solutions with 1,2-ethanediamine was monitored using a type-K gage-40 thermocouple immersed in the mixture, contained within a polypropylene test tube. Tested liquid volume for measuring viscous fluid properties was about 20 mL, and 2 mL for all other examined

properties.

3.2.3 Simultaneous nail penetration and injection testing

The short circuit joule heating suppression capabilities of LIB electrolyte poisoning agents were evaluated using a simultaneous nail penetration and poison injection method developed for LIR2450 coin cells. To allow for rapid introduction of poisons immediately upon abuse, the LIR2450 cells were modified with cell cases outfitted with 2 holes through which tubes were inserted to facilitate fluid injection using a syringe. Poisoning agents were injected into the LIB cells through one of the holes punched into the modified cell case just prior to nail penetration, induced using a coin cell holder / drill press assembly. The temperature response was measured using a thermocouple, and joule heating resistance dynamics were discerned for further evaluation.

Modification of a coin cell and subsequent nail penetration and poison testing injection testing proceeded according to the following procedure (images of the cell at various points of the procedure are shown in Figure 3.1):

1. Cell taken as received was conditioned by cycling twice at 10 mA from 3.0 V - 4.2 V, then fully charged to 4.2 V using a BTS4000-5V10mA Battery Analyzer.
2. LIR2450 cell case, obtained from Xiamen TOB New Energy Technology, was modified by cutting 2 3/16” outer diameter, 1/16” inner diameter holes on the positive terminal enclosure using a hand punch, approximately 3/16” from the edges on opposite sides of the piece.
3. Coin cell was disassembled in an argon filled MBraun LABStar glovebox using an MTI Corporation MSK-110 Hydraulic Press with CR2450 Disassembling Die Set.

4. Charged electrode stack was harvested, oriented between the 2 holes of the modified cell case, and reassembled using an MTI Corporation MSK-110 Hydraulic Press with CR2450 Crimping Die Set.
5. Modified cell was removed from the glovebox, and holes were plugged with 3/16" diameter Tygon tubing, coated with vacuum grease to form leakproof seal.
6. Type-K gage-40 thermocouple was affixed 6 mm from the center of the modified cell case on the positive terminal and connected to an Omega OM-EL-USB-TC Data Logger.
7. Modified cell was tested to ensure an open circuit voltage greater than 4.15 V using a BK Precision 2405A Digital Multimeter, certifying charged capacity was maintained during the reconstruction process.
8. Modified cell was secured to a custom-made 12 mm thick polyurethane base holder using masking tape, and assembly was fastened to a drill press loaded with a stainless steel nail (3.8 mm diameter, 50 mm long) to initiate shorting.
9. Syringe with 1/16" diameter needle tip containing predetermined volume of poison was inserted into inlet Tygon tube and outlet tube is routed to waste collection vessel.
10. After 10-minute standby period, poison was injected into the cell and nail penetration was subsequently performed using the drill press assembly within 1 second.
11. Cell temperature was monitored over a 20-minute period and saved for further analysis.

The reference nail penetration tests underwent the identical cell case modification and reconstruction procedure, but no poisoning fluid was injected into the cell. The measured cell temperature response signal was used to determine the effective heat generation rate ($\dot{q}_{\mathrm{gen,eff}}$), which was compared with the reference nail penetration joule heat generation rate ($\dot{q}_{\mathrm{gen,ref}}$) and

internal resistance (R_{ref}) dynamics, to deduce the degree to which the effective short circuit resistance (R_{eff}) was exacerbated by the poison. Heat transfer determination methods and parameters are enumerated in Section 2.2.4.

$$\frac{R_{\mathrm{eff}}}{R_{\mathrm{ref}}} = \frac{\dot{q}_{\mathrm{gen,ref}}}{\dot{q}_{\mathrm{gen,eff}}} \tag{3.1}$$

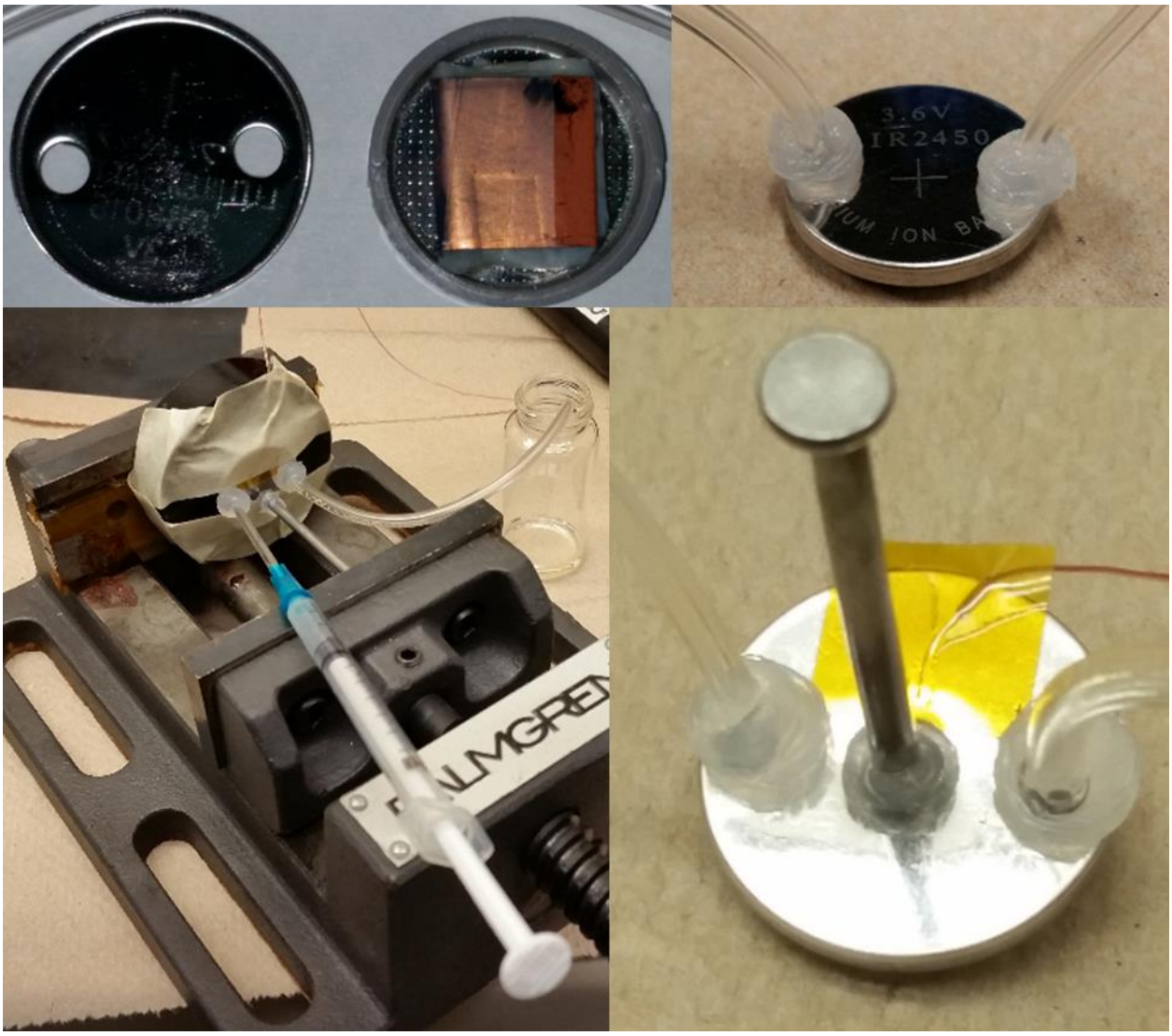


Figure 3.1 Modified cell case reconstruction and simultaneous nail penetration and poison injection testing.

3.2.4 Modified cell case encapsulated poison impact testing

The heat suppression capability of encapsulated poisoning agents released into the LIB environment upon rupture of a breakable container in a mechanical impact induced short circuit event, was evaluated via poison encapsulation in a modified LIR2450 cell case. The poison was encapsulated in an aluminum container incorporated into a modified cell case structure. A custom-made mechanical impact testing drop tower system (schematic depicted in [74]) was used to push the container into the LIR2450 electrolyte stack, simultaneously inducing shorting. The temperature response was measured using a thermocouple to demonstrate the feasibility of a mechanically-activated electrolyte poisoning safety strategy.

Modification of a coin cell and subsequent impact testing proceeded according to the following procedure (images of the cell at various points of the procedure are shown in Figure 3.2):

1. Cell taken as received was conditioned by cycling twice at 10 mA from 3.0 V - 4.2 V, then fully charged to 4.2 V using a BTS4000-5V10mA Battery Analyzer.
2. Poison was encapsulated in a 40 µL aluminum container (Perkin Elmer part #02190041) sealed using a crimping press (Perkin Elmer part #02190048).
3. LIR2450 cell case, obtained from Xiamen TOB New Energy Technology, was modified by cutting a 9/32” hole on positive terminal enclosure using a hand punch, and replaced with the encapsulated poison aluminum container.
4. Coin cell was disassembled in an argon filled MBraun LABStar glovebox using an MTI Corporation MSK-110 Hydraulic Press with CR2450 Disassembling Die Set.

5. Charged electrode stack was harvested, oriented between in the center of the modified cell case, carefully sealed with polyimide tape to avoid breaking the encapsulated poison aluminum container, and removed from the glovebox.
6. Type-K gage-40 thermocouple was affixed 5 mm away from the aluminum container component of modified cell case on the positive terminal and connected to an Omega OM-EL-USB-TC Data Logger.
7. Modified cell was tested to ensure an open circuit voltage greater than 4.15 V using a BK Precision 2405A Digital Multimeter, certifying charged capacity was maintained during the reconstruction process.
8. Modified cell was secured to a custom-made 12 mm thick polyurethane base holder using masking tape, and assembly was secured in a custom-made impact testing drop tower.
9. After 10-minute standby period, a 7 kg cylindrical steel hammer was dropped from a distance of 30 cm onto a 1/4” diameter brass ball indenter suspended 5 mm above the mechanically-triggered aluminum container component of the cell case.
10. Cell temperature was monitored over a 20-minute period and saved for further analysis.

The temperature response of reference cells was determined with modified cases and tested under the same conditions, but no poisoning fluid was added to the aluminum container. In the absence of reliable heat transfer parameters because of non-traditional coin cell sealing without a hydraulic press, effective heat generation rate and resistance measurements were not considered in these experiments.



Figure 3.2 Modified LIR2450 coin cell with encapsulated poison aluminum container incorporated into the cell case shown before and after drop tower impact testing.

3.3 Poison selection and evaluation

3.3.1 Diol poison selection motivations and mechanism evaluation

Modern-day, commercialized LIB electrolyte consists of a conductive inorganic lithium salt, most commonly $LiPF_6$, dissolved in a solution of cyclic carbonates, such as EC, and linear alkyl carbonates, such as EMC. To achieve high ionic conductivity and low resistance, the salt concentration should be high, while the solution viscosity is low [95,96]. Efforts to dilute the electrolyte while simultaneously raising the viscosity, disrupting ionic conductivity to subdue joule heating in a short circuit event, are discussed as follows.

The previous study showed that when slowly discharging at low temperatures, polarized electrolyte resistance is greatest in the anode region due to increased viscosity, despite moderate increase in local lithium-ion charge-carrier concentration. At high discharge rates, significant increase in local charge-carrier concentration occurs within the anode region, but the accrued temperature negates any would-be concentration induced viscosity increase, such that lithium-ions maintain mobility and the electrolyte remains conductive in that locality [105].

Diluting the electrolyte and raising electrolyte viscosity would hamper charge-carrying ion availability and mobility in all regions, hindering the ability for them to travel from the anode to the cathode, slowing the joule heating rate. Diols have two intermolecular hydrogen-bonding hydroxyl functional groups that allow them to form supramolecular polymer networks, yielding high viscosity fluid properties [106,107]. As the electrolyte's viscosity is proportional to its resistance, selected diols up to 25 times more viscous than pristine electrolyte at room temperature are rapidly mixed as diluents to increase impedance. Using these species as poisons could thicken

the electrolyte solution and simultaneously reduce charge-carrier concentration to slow discharge to manageable rates, if introduced early the short circuit progression.

Mixing pristine electrolyte in equal volumes with α,ω-polymethylenediols HO-$(CH_2)_n$-OH of n=2, 3, and 5 methylene bridges increases viscosity by 1.7-fold, 2.4-fold, and 4-fold, respectively at room temperature (Figure 3.3). The resultant viscosity of the mixture is closer to that of the pristine electrolyte than the neat diol, which is likely because the pristine electrolyte components are aprotic, forming end-caps on the hydrogen-bonding supramolecular polymer chains, segmenting them into smaller groups such that the diol network losses much of its viscous character. Furthermore, the degree of thickening incurred by addition of diols is reduced as temperature increases, both in terms of absolute viscosity and relative increase with respect to the pristine electrolyte reference at equivalent temperature. This is not surprising considering both fluids demonstrate Arrhenius-type viscosity dependence on temperature. As such, employing diols as electrolyte poisons is likely to be most effective at low temperatures, but offer diminishing returns as shorting progresses and the generated joule heat accrues.

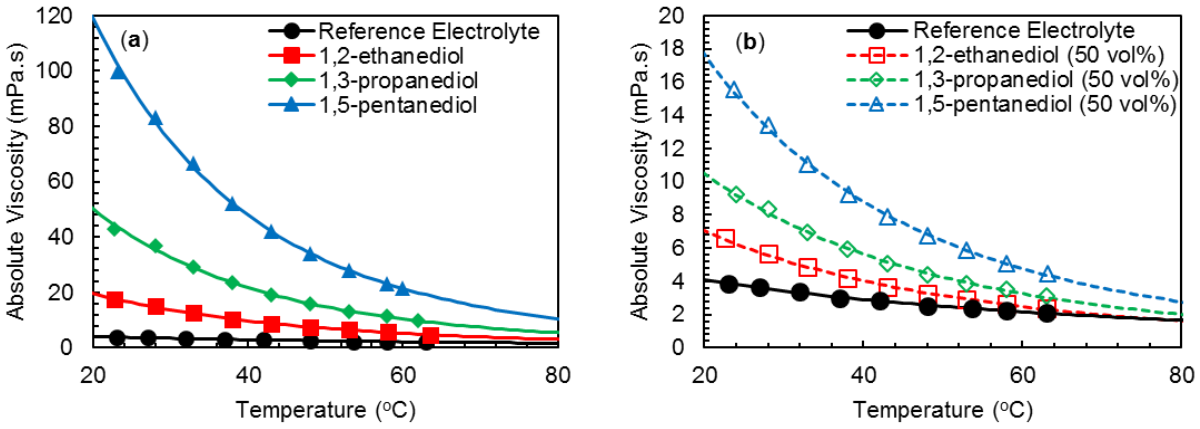


Figure 3.3 (**a**) Viscosity of pristine electrolyte, diols, and (**b**) electrolyte / diol mixed solutions.

The diols demonstrate an ability to suppresses the ionic conductivity of pristine electrolyte (Figure 3.4). Larger, more viscous diol species employed in high loadings have a greater degree of influence, with 1,5-pentanediol reducing ionic conductivity by 80% within 1 minute when added at 50 vol%, equating a 5-fold increase in electrolyte resistance. In addition to increased viscosity, reduced salt concentration and lower permittivity imparted by mixing the lower dielectric constant poison also influences the resultant ionic conductivity. Conversely, 1,2-ethanediol increases the ionic conductivity of the mixture when added at less than 20 vol%, despite moderately raising viscosity and reducing ion concentration, likely due to moderate increase in permittivity by the higher dielectric constant poison (Table 3.1). However, as 1,2-ethanediol loading further increases, viscous contributions and charge-carrier concentration reductions overwhelm conductive gains experienced at low diol loadings, reducing ionic conductivity by 50% within 1 minute when added at 50 vol%, equating a 2-fold increase in electrolyte resistance.

Given the ionic conductivity results for poisoned electrolyte solutions, all three diols are expected to have a consequential influence on short circuit response with sufficient poison loading, as the impedance exacerbation sensitivity analysis of Section 2.5.7 shows even a 2-fold increase in electrolyte resistance can make a notable difference.

Table 3.1 Dielectric constant of pristine electrolyte, electrolyte components, and diols.

	EC:EMC (1:1 w:w)	EC	EMC	1,2-ethanediol	1,3-propanediol	1,5-pentanediol
ε (25 ^{o}C)	33.6 [100]	95.2 [100]	3.5 [100]	40.3 [108]	34.4 [108]	25.6 [108]

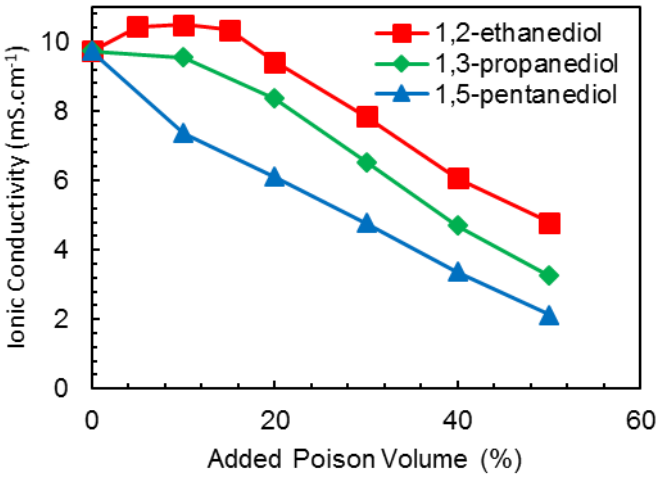


Figure 3.4 Ionic conductivity of pristine electrolyte / diol mixed solutions.

3.3.2 Diamine poison selection motivations and mechanism evaluation

An electrolyte solvent's permittivity should be sufficient to stabilize separation of the positively and negatively charged ions of the electrolyte salt to be soluble within the solution, and promote mobility as a conducting medium. In traditional LIB electrolytes, such as $LiPF_6$ EC:EMC 1:1 w:w electrolyte, the cyclic carbonate, EC, has a much higher dielectric constant than the linear alkyl carbonate, EMC [100]. If the EC solvent component no longer offers its dielectric property to the solvent, the solution would lose its permittivity, such that the $LiPF_6$ salt's ions would not remain stable in a separated state, and the lithium-ion could no longer facilitate charge-transfer from the anode to the cathode. Efforts to actively interfere with the EC electrolyte component to subdue joule heating in a short circuit event, are discussed as follows.

In a previous study, primary and secondary amines were demonstrated to have poisonous character in electrolyte, as identified using the simultaneous nail penetration and fluid injection testing method [109]. The heat generation suppression phenomenon was identified to be chemical

reaction with the high dielectric constant EC electrolyte component via ring-opening mechanism [110]. As low molecular weight primary diamines comprise a particularly high density of reactive, EC-passivating amine functional groups, they are selected for examination with the expectation they are potent permittivity-disrupting poisons.

Furthermore, this EC / diamine reaction mechanism has also been discussed as a synthesis route for polyurethane [111]. In general, higher-molecular-weight species of a particular chemical classification tend to have higher viscosity and lower melting points than lower-molecular-weight species, as is characteristic of diols for instance [106]. As larger, non-permitting oligomer species are formed in the EC / diamine polymerization poisoning process, solution viscosity is expected to increase to slow charge-carrying ion species, eventually curing the liquid electrolyte into a nonconductive solid mass.

Upon mixing EC:EMC (1:1 w:w) solution with 20 vol% 1,2-ethanediamine, notable reaction heat is generated, compounding to gradually increase temperature over several minutes, suggesting ring-opening polymerization occurs (Figure 3.5). When mixed with pristine electrolyte, the reaction is more aggressive, resulting in a faster temperature increase. This suggests that $LiPF_6$ either participates in or catalyzes the EC / diamine reaction, also potentially interacting through competing solvation [112]. The diamine reaction also rapidly increases solution viscosity as higher molecular weight products are formed, in addition to starving the electrolyte of its solvent's permittivity. The reaction amasses an almost completely solid reaction product within 10 minutes.

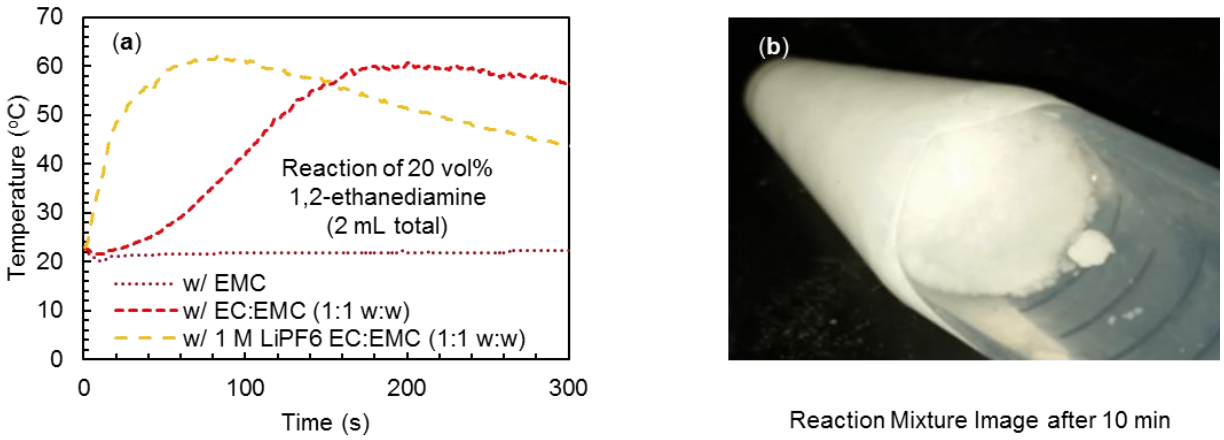


Figure 3.5 (**a**) Reaction temperature of 2 mL mixture of electrolyte components with 20 vol% 1,2-ethanediamine and (**b**) image of solid reaction product after 10 minutes.

As expected, the diamines are excellent for quickly raising electrolyte resistance with relatively low poison loadings (Figure 3.6). Upon introduction of the diamines, a drastic reduction in ionic conductivity of 95% is realized within 1 minute when added at only 20 vol%, equating a 20-fold increase in electrolyte resistance. According to the impedance exacerbation sensitivity analysis of Section 2.5.7, a 20-fold increase in electrolyte resistance effectively stops joule heat generation upon polarization. This result demonstrates the extreme potency of the EC / low molecular weight primary diamine poisoning interaction.

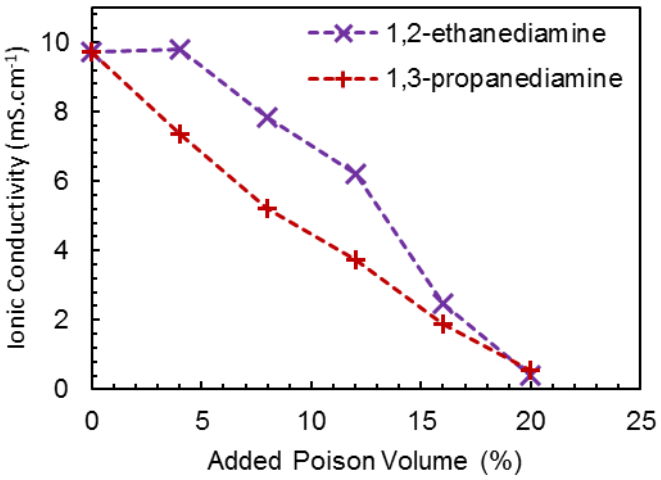


Figure 3.6 Ionic conductivity of pristine electrolyte / diamine mixed solutions.

3.3.2 Simultaneous nail penetration and poison injection testing

The competing short circuit discharge and reaction agent poisoning dynamics of these fluids are evaluated via simultaneous nail penetration and injection testing of LIR2450 cells. The temperature response collectively captures joule heat generation, heat of mixing, and poison / system reaction heating. The overall effectiveness and time to action of the poisons' heat suppression kinetic capabilities and diffusive distribution are observed in direct competition with the short circuit discharge current. Together, the all-encompassing consequent heat generation rate measurements allow for deduction of the effective resistance exacerbation increase dynamics, considering all exothermic phenomena associated with the poisoning event, to evaluate their effectiveness as thermal runaway mitigation agents. These phenomena are analyzed considering the nature of short circuit discharge kinetics to inform further investigation, select effective candidates for device testing, and facilitate diverse safety component designs.

Upon diol injection, quick mixing dilutes the native electrolyte, increasing its viscosity to

slow the ion transport between electrodes, thus suppressing the discharge current and joule heating rates (Figure 3.7 and Figure 3.8). The results show the influence of the tested diols increases sequentially with molecular size, as expected based on the measured viscosity and conductivity. The 400 µL injection volume is about 15 wt% of all LIB cell components, excluding the cell case. This poison content produces an effective resistance increase to joule heating averaged over the first 3 minutes of shorting by 1.9-fold, 2.2-fold, and 2.7-fold for 1,2-ethanediol, 1,3-propanediol, and 1,5-pentanediol, respectively. For 1,5-pentanediol, active poisoning reduces the peak temperature accrued by 58% compared to the unmitigated reference nail penetration scenario.

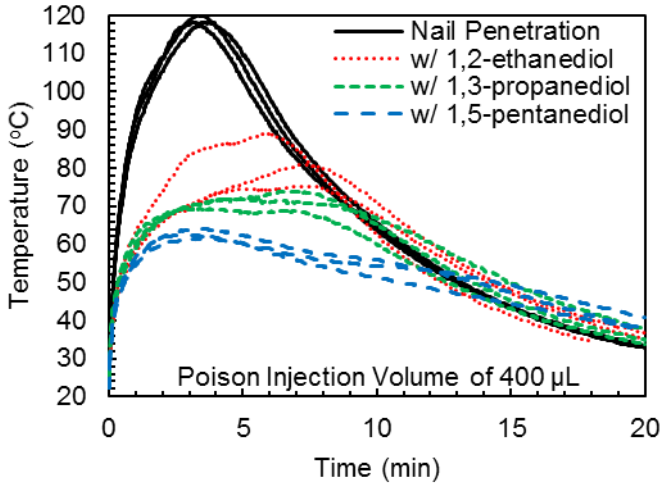


Figure 3.7 Cell temperature response observed in simultaneous nail penetration and diol injection testing of LIR2450 coin cells.

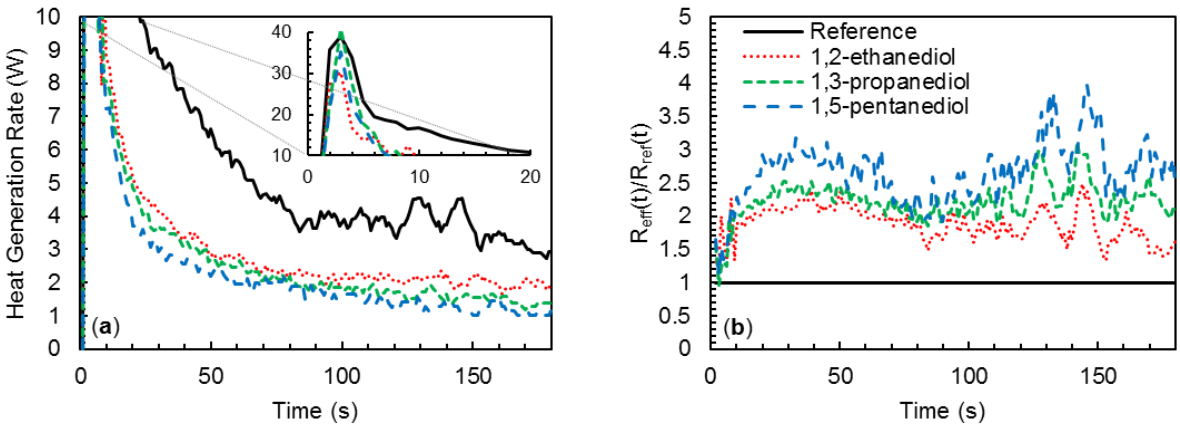


Figure 3.8 (**a**) Heat generation rate and (**b**) effective internal resistance increase dynamics observed in simultaneous nail penetration and diol injection testing of LIR2450 coin cells.

For diamine poison injection, the effective resistance increase manifests slower than it does for the diols, but the ultimate magnitude is more significant once it takes full effect (Figure 3.9 and Figure 3.10). The EC poisoning reaction proceeds gradually over time, decreasing permittivity and increasing the viscosity with the extent of reaction. The EC / diamine reaction also generates heat, which contributes to the observed temperature response. These inherent characteristics of diamine poison / electrolyte mixing delay the resistive contributions, but after the first 3 minutes of shorting, the effective resistance to joule heating is nearly 10-fold that of the reference event, essentially shutting down electrochemical function thereafter. Both tested diamines are potent, with little discernable difference observed in the nail penetration temperature response. The 65 µL diamine injection volumes, about 2.5 wt% cell mass, excluding the cell case, reduces peak temperature accrued by 62% with respect to the unmitigated shorting reference on average.

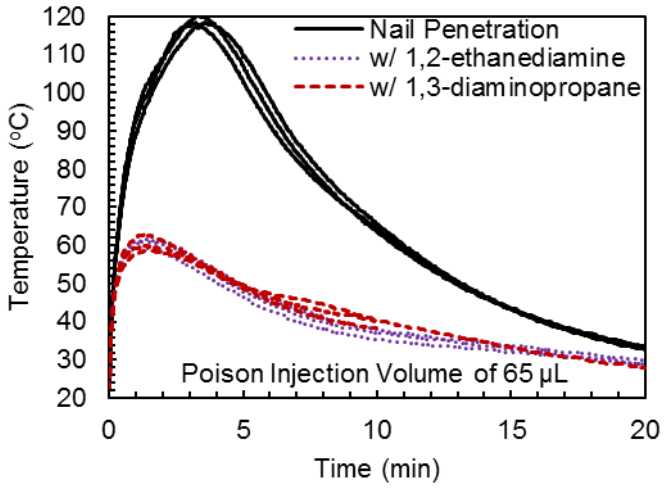


Figure 3.9 Cell temperature response observed in simultaneous nail penetration and diamine injection testing of LIR2450 coin cells.

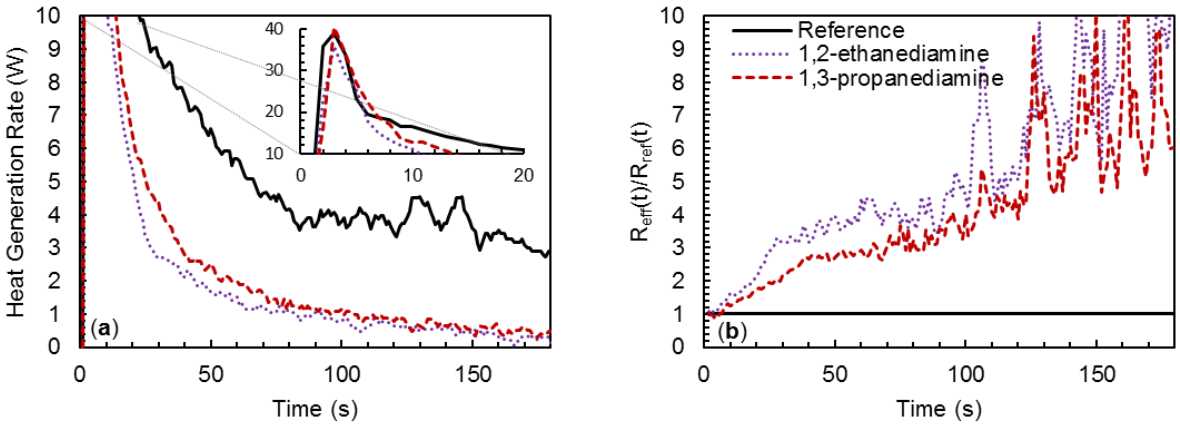


Figure 3.10 (**a**) Heat generation rate and (**b**) effective internal resistance increase dynamics observed in simultaneous nail penetration and diamine injection testing of LIR2450 coin cells.

This thermal runaway mitigation strategy shows merit in its ability to curb discharge heating rates at low temperatures, as demonstrated via in-situ short circuit experimentation with consistent responses over many repeated trials. The exacerbation impedance capabilities of the candidates follow the trends shown in the poisoned electrolyte conductivity measurement experiments, albeit not at the same magnitudes. More importantly, these tests elucidate the

timescales over which each candidate is capable acting for determination of whether or not, and how they can be most effectively used.

Active poisoning of the LIB electrolyte raises resistance upon polarization, but does not have any influence on the ohmically-controlled capacitive discharge feature described in Section 2.4.5, demonstrating the dynamic heating response characteristics predicted in Section 2.5.7. This is expected, given that poison introduction is intended to hinder ion-conduction, and not electron-conduction. Nonetheless, the mechanism of action should be as fast as possible to throttle heat generation prior to realization of increases in electrical and ionic conductivities experienced upon increasing temperature. As such, the diols, which are immediately effective upon mixing, may be better choices as poisoning agents than the higher-potency diamines, which have delayed resistive influence characteristic of their chemical reaction mechanism.

3.4 Electrolyte poisoning device design

3.4.1 Encapsulated poison impact testing

Encapsulated poisons rigged for release upon mechanical-activation in physical abuse events would allow for introduction of LIB shutdown agents at low temperature without influencing everyday performance prior to triggering. There are a variety of container designs and placement locations to be considered, depending on the poisons' mechanisms of action. To minimize mass the safety feature would add at the expense of energy density, existing cell structural components could be considered for functionalization as containers, like the way polypropylene separators are functionalized to house a thermally-activated polyethylene blocking

agent layer in the trilayer shutdown design [101]. This concept is demonstrated upon impact testing of LIR2450 units with modified cell case structures encapsulating 1,5-pentanediol, as described and depicted in Section 3.2.3.

The modified cell cases are retrofitted with a thin metal aluminum 40 µL container either housing 1,5-pentanediol fluid or remaining empty for reference testing. In this demonstration, the container is punched into the electrode stack with the custom-made drop tower system to simultaneously initiate shorting and break the container, releasing the poisoning agent immediately upon impact. The temperature responses are monitored for evaluation (Figure 3.11).

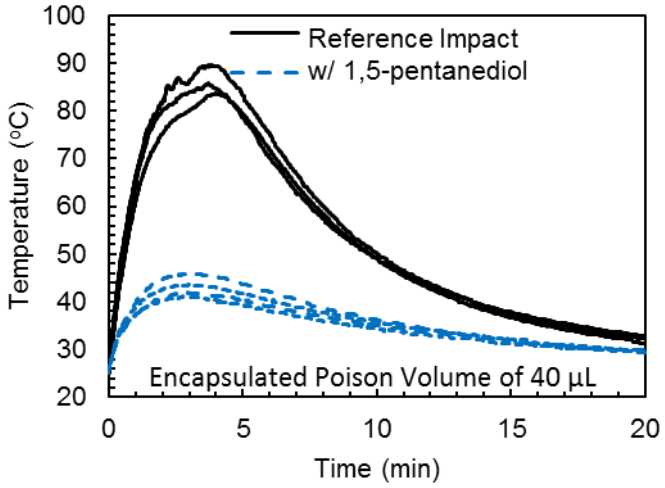


Figure 3.11 Cell temperature response observed in impact testing of LIR2450 cells with modified cases housing 1,5-pentanediol.

The modified cells containing 1,5-pentanediol accrue a maximum temperature increase 65% to 75% lower than the modified reference cells containing no fluid. Immediate release of the diol poisoning agent fluid upon impact clearly has a notable influence on the LIB cells ability to generate heat upon shorting. That said, temperature suppression in this orientation is limited to this specific impact scenario. If this specific cell design were not impacted in this manner, the fluid

may not enter the electrode stack, and would not likely to have the same influence. More robust designs might include poison spread through the entirety of the cell case, supported by other safety features. Nonetheless, the experiment demonstrates the mechanically-activated encapsulated poison concept is a viable approach to address joule heat at the earliest stages of short circuit discharge.

The impact testing response is quite different than that of nail penetration, so both tests are important when evaluating the feasibility of specific poison and container selections. Mechanical response of the poison-encapsulation container may also influence the temperature response observed, as the mode of damage influences the nature of the short circuit electrical connections formed within the multicomponent battery stack, some types more powerful than others [79]. Depending on the design of the container or properties of the poison, this could be advantageous in dampening the impact intensity, or distributing the reaction force in a manner that decreases the probability severe short circuit connections form within the cell [77]. Considering the expected failure mechanism, intended mechanical response is also an important aspect of the safety feature design.

Further examination demonstrates the merits of this thermal runaway mitigation strategy in another study, employing breakable containers housing electrolyte poison placed within vacancies arranged in the electrode stack [76]. Using the simultaneous nail penetration and injection method, liquid alkanes are identified to be effective blocking agent poisons. Those alkanes contained in inert capsules are shown to curb temperature increase in impact testing of pouch LIB cells.

The poisons selected are aggressive, and would interfere with electrochemical performance if exposed to the LIB environment prior to their intended release, rendering the cell unusable. In

this demonstration, the container resides outside of the working LIB environment in a structurally-robust element of the battery, so the modification is not expected to have influence on the electrochemical performance prior to activation. When this poison is housed within the LIB environment in fragile containers, more careful attention is needed to confirm the integrity of the encapsulating structure throughout the manufacturing process, to avoid premature rupture.

3.4.2 Multifunctional thermal management systems

Diols have useful heat transfer properties and are inherent to many thermal management systems in large volumes, including those controlling LIB pack temperature in electric vehicles. Thermal management systems have previously been considered for functionalization as emergency thermal runaway mitigation devices to absorb heat, through incorporation of endothermic phase change materials [49] or LIB module flooding with high specific heat and fire retardant fluids [51]. Recognizing thermal management systems are innate vessels of diol fluid, as well as the merits of diols as electrolyte poisons, thermal management systems could also be considered for functionalization as active shutdown poisoning systems, without adding poisoning fluid mass to the vehicle.

The most common diol used in thermal management fluids is 1,2-ethanediol. Thermal management fluids also incorporate corrosion inhibitors to protect the conduits through which they travel. Primary diamines are commodity chemicals with a wide range of uses, and have been considered for corrosion inhibitor applications for many decades [113]. Specifically, 1,2-ethanediamine has shown to be an effective corrosion inhibitor in modern thermal management fluid formulations, for automotive heat exchangers comprising 1,2-ethanediol [114].

While 1,2-ethanediol is the least effective of the reaction agent poisons discussed in this narrative, its resistive contributions are immediately apparent upon mixing with electrolyte. In contrast, 1,2-ethanediamine is effective in exacerbating electrolyte resistance, but its resistive influence is delayed, as it takes time for the poisoning reaction to proceed, such that increasing injection volume above 65 µL does not have an appreciable consequence in further temperature suppression. In simultaneous nail penetration and injection testing of LIR2450 cells with a 400 µL injection volume of 1,2-ethanediol and 1,2-ethanediamine mixed in a 4:1 v:v ratio, it is demonstrated that a mixed solution of the two fluids is more effective at suppressing joule heating than either of them individually. Peak temperature accrued is reduced by 70% of the unmitigated reference value, and time to reach peak temperature increased by about 25% with respect to pure diamine injection (Figure 3.12).

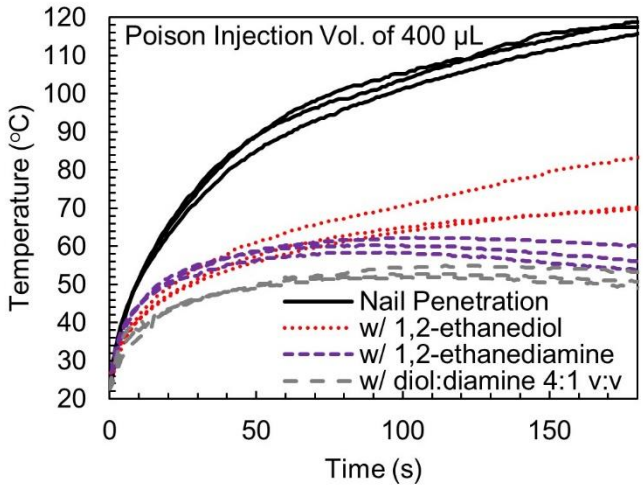


Figure 3.12 Simultaneous nail penetration and poison injection temperature response of LIR2450 cells with 400 µL of 1,2-ethanediol, 1,2-ethanediamine, and 1,2-ethanediol:1,2-ethanediamine 4:1 v:v mixed solution.

Given that both diol and diamine fluids demonstrate efficacy as reaction agent poisons for LIB shutdown, and exhibit both usefulness as well as abundance in fluid formulations characteristic of thermal management systems, they could be considered for advanced safety feature device designs. For example, battery management and thermal management systems are closely coupled with LIB cells in electric vehicle modules, with electrical and thermal sensing capable of identifying dangerous conditions, as well as control over pressurized thermal management fluid motion through the LIB pack [67]. One might envision that with greater integration of the thermal management system's fluid conduits with the LIB cells, the vehicle's onboard computer system could guide the fluid into the LIB cells to actively shut them down if the battery management system's sensors identify overtemperature, short circuit, or mechanical damage events. Maintained outside of the LIB cells' electrochemical environments prior to a triggering event, large volumes of shutdown fluid are available in an emergency, without sacrificing energy density nor risking disruption of everyday performance. Considering the infrastructure is already outfitted to electric vehicles, novel safety features could be incorporated to protect vehicle occupants in emergency situations through multifunctional design, given knowledge of the electrolyte poisoning characteristics of diols and diamines.

This investigation demonstrates encouraging results in controlled testing of LIR2450 cells, serving to identify and vet the merits of poisoning candidates for further engineering development and validation in large-format cells, where joule heating dynamics and diffusion characteristics are more challenging, and abuse conditions are less predictable. The poisons discussed in this narrative are only useful if they are delivered effectively, and it is critical any containers or delivery devices hold the liquids in manner such that they do not prematurely disrupt electrochemical performance. Modifications to the LIB cell, such as electrode stack reorientation or vacancy formation, might

also increase the efficacy of poisoning strategies, so new poison delivery devices should be designed in tandem with the cells in which they are to be incorporated. Device optimization is essential to maximize the safety margin, and knowledge of these chemical species presents opportunities to increase that margin in addressing joule heating during the earliest stages of short circuit failure, bridging the gap between traditional primary protection structures and thermally-activated failsafe features.

3.5 Conclusion

Diols and diamines are shown to be aggressive electrolyte reaction agent poisons capable of shutting down lithium-ion batteries in an emergency. By manipulating the permittivity and viscosity of electrolyte, ionic resistance is forcibly exacerbated to slow short circuit discharge and corresponding joule heating kinetics, to curb temperature accruement in a short circuit event. Examined for the purpose of encapsulation within inert materials rigged for release into the battery environment upon mechanical-abuse, a unique nail penetration and poison injection system is developed to evaluate the competing dynamics of the poisoning candidates and short circuit joule heating in real-time.

Mechanically-activated poisoning containers are incorporated into the structure of battery cell cases and punched into the cell, initiating shorting and releasing the poison into the battery immediately upon impact to demonstrate the feasibility of this thermal runaway mitigation strategy, which addresses short circuit failure in the earliest stages. Diol and diamine mixed solutions show synergistic effects in simultaneous nail penetration and poison injection experiments of battery cells. Recognizing their merits as thermal management fluids and corrosion

inhibitors, multifunctional applications are discussed for functionalization of battery management systems inherent to electric vehicles as advanced safety features.

3.6 Acknowledgements

Chapter 3, in part, is a reprint of the published material as it appears in Journal of Power Sources. Daniel Noelle, Yang Shi, Meng Wang, Anh V. Le, and Yu Qiao., 2018. Aggressive electrolyte poisons and multifunctional fluids comprised of diols and diamines for emergency shutdown of lithium-ion batteries. *J. Power Sources, 384, 93-97.* The dissertation author was the primary investigator and first author of the paper.

Chapter 4 Improved safety and mechanical characterizations of thick lithium-ion battery electrodes structured with porous metal current collectors

4.1 Introduction

Structural lithium-ion battery (LIB) designs present opportunities to increase the energy density of LIB-powered devices by undertaking both electrochemical and mechanical load-bearing functions, without modifying the underlying LIB chemistry [115]. By using energy-storing LIBs to give a device its structural form, overall mass and volume can be reduced to improve performance if the LIBs can sustainably fulfill both tasks [116,117]. Multifunctional design could aid in lightweighting of electric vehicles to extend driving range capabilities or reduce the size of personal electronics to make them easier to carry [29,118,119]. However, structural applications make LIBs more susceptible to physical damage, which could induce dangerous short circuit events leading to thermal runaway. As such, multifunctional LIBs with greater degrees of device integration demand more robust mechanical properties and greater margins of safety against abuse [30].

Porous metal current collectors (also referred to as metal foam current collectors) can serve as electrically-conductive structural reinforcements to enable thick electrode orientations with high aerial capacity [120–123]. When filled with an electroactive matrix of energy-storing active materials, conductive additives, and adhesive polymer binders, interpenetrating phase composite (IPC) electrode structures with unique mechanical characteristics are formed [124,125]. Unlike traditional laminate composite (LC) electrodes using 2D metal foil current collector substrates, which are coated with electroactive matrix layers on each side typically with thicknesses on the

scale of 50–100 μm [120], porous metal current collectors offer a 3D foundation. In an IPC orientation, active materials can be retained close to the nearest porous metal current collector surface even when the overall electrode thickness is much larger, ensuring electron conduction uniformity and achieving high aerial loading of the electroactive matrix [121]. High capacity IPC electrodes allow for fewer bilayers to be used compared to traditional LC electrodes, reducing the need for nonelectrochemical support components such as separators, which helps increase the volumetric energy density [126,127].

Current collectors have a significant role in short circuit discharge electrical kinetics and the electroactive matrix layer thicknesses have a notable influence on ion transport dynamics [24,105]. Upon physical damage of traditional LC electrode multilayer assemblies, direct contact between the metal foil current collectors is often the major cause of thermal runaway [79]. Electrons will rapidly discharge across low-resistance pathways afforded by the electrically-conductive metals, moving in tandem with lithium-ions travelling short distances through the electrolyte within the thin, porous electroactive matrix layers. As the electrons and the ions recombine in the cathode's active material particles, liberated joule heat can cause temperature to accrue to dangerous levels in a matter of seconds [20]. The metal foil current collectors dictate the ultimate strength of the LC electrodes, and strategic weakening of the metal foil has been shown to greatly improve safety in impact testing [74]. Thus, restructuring of the electrodes with porous metal current collectors into IPCs without strong homogeneous metal layers, as well as longer ion transport lengths, may exhibit improved safety characteristics.

The mechanical properties of the IPC electrodes are categorically different from traditional LC electrodes. In LC electrodes, the high tensile modulus metal foil component is thin, and located at the center of the structure where it imparts only low flexural stiffness to the electrode structure

[128]. The porous metal current collector in heterogeneous IPC orientation reinforces the electroactive matrix throughout the thickness [124,125]. Additionally, flexural stiffness tends to increase with larger thickness components. High flexural stiffness is critical to minimizing deflection to maintain form and function when subject to mechanical loading. With these mechanical performance and safety design considerations, IPC electrodes with porous metal current collectors are investigated.

4.2 Experimental methods and data acquisition

4.2.1 Electrode processing

Porous metal current collectors were provided by the Sumitomo Electric Industries, Ltd. The cathode's aluminum foam current collector (Al Celmet) had an initial thickness of 1.0 mm, porosity of ~95%, and pore density of ~45 PPI. The anode's copper foam current collector (Cu Celmet) had an initial thickness of 1.0 mm, porosity of ~94%, and pore density of ~105 PPI. They were filled with high-density LIB electrode slurries by hand using a spatula, and then dried under vacuum at 80 ^{o}C for 24 hr. Once dry, the IPC electrodes were calendered to 600 µm thicknesses using a generic rolling press containing 2 rollers with 7.62 cm diameter in a single passthrough motion. The electrodes were cut into 1.98 cm^2 circular discs, which were subsequently characterized using a Fischer Scientific mass balance.

The high-density LIB electrode slurries, containing active materials, conductive additives, and adhesive binders, were prepared by dispersion and homogenization in processing solvents using a QSonica Q55 Sonicator with 3.2 mm diameter submersible ultrasonic horn in 10 mL Pyrex

beakers (25 mm diameter, 33 mm height). Systematically applied ultrasonic power at a frequency of 20 kHz was controlled, such that standing wave resonance was maintained throughout the mixing processes. The ultrasonic friction and processing solvent cavitation was used to heat the slurry while mixing, and active stirring by hand with the horn tip ensured temperature uniformity during the homogenization process and upon cooling, as monitored by 2 type-K gage-40 thermocouples affixed to opposite sides of the beaker, connected to a Digi Sense 20250-02 Temperature Logger. The processes yielded slurries with appropriate casting viscosities at room temperature. Details of optimized power application, slurry temperature, and mixing event progression during the processes are given in Section 4.3.1.

For cathode, $LiCoO_2$ (LCO, Lectro Plus 100, FMC Lithium), carbon black (CB, C-Energy Super C45, TIMCAL), and polyvinylidene fluoride (PVDF, MW ~534,000 powder, Sigma Aldrich) were dispersed in the ratio of LCO:CB:PVDF 93:3:4 w:w:w totaling 10.8 g into 3.6 g of N-methyl-2-pyrrolidone (NMP, anhydrous 99.5%, Sigma Aldrich). LCO, CB, and PVDF powders were premixed using a mortar and pestle prior to dispersion in NMP.

For anode, graphite (TIMREX SLP30, TIMCAL), CB, carboxymethylcellulose sodium salt (CMC, medium viscosity, Sigma Aldrich), and styrene-butadiene rubber (SBR, MTI Corporation) were dispersed in the ratio of graphite:CB:CMC:SBR 93:2:2:3 w:w:w:w totaling 3.15 g into 3.5 g of deionized water (DI). The CMC salt was first dissolved in DI water. The SBR liquid was subsequently mixed in solution at 80 ^{o}C for 1 hour using a Corning PC-420D Stirring Hot Plate. Then, graphite and CB powders were fully mixed into the solution using a glass stir bar prior to ultrasound application. Graphite and CB powders were premixed using a mortar and pestle before being added to the DI / CMC / SBR solution.

4.2.2 Electrochemical performance and abuse characterization

LIR2032 format full cells were constructed for electrochemical characterization and short circuit abuse testing of the IPC electrode assemblies. The electrode stacks were assembled in uniaxial orientation using one cathode disc, one anode disc, one trilayer separator layer (Celgard 2320), and a copper foam spacer used to secure electrical and thermal contact with the cell case. The electrodes and separators were submerged in 1 M $LiPF_6$ EC:EMC 1:1 w:w electrolyte (BASF Selectilyte LP50), and subjected to reduced pressure atmosphere of 85 mmHg at room temperature for 3 min, ensuring complete wetting prior to cell construction. Cells were sealed using an MTI Corporation MSK-100 hydraulic press with CR20XX crimping die set inside an MBraun LABStar glovebox with water-free argon atmosphere (H_2O <0.5 ppm).

Galvanostatic analysis was carried out using a Neware BTS4000-5V10mA Battery Analyzer. The mass and dimensions of galvanostatic-conditioned electrode stack assemblies and components were measured in the discharged state with a Fischer Scientific mass balance and displacement micrometer inside the glovebox. Measurements were made immediately upon deconstruction using the MTI Corporation MSK-100 hydraulic press with CR20XX disassembling die set. These measurements were taken to evaluate energy density accounting for electroactive matrices, current collectors, separator, and saturated electrolyte mass internal to the stack, while excluding mass and volume contributions from cell cases, connecting tabs / spacers, and electrolyte external to the stack.

The LIB cells were subjected to external shorting and nail penetration testing, performed using the same testing procedures described in Section 2.2.3. In external shorting, current response was directly measured using a Neware BTS3000-5V6A Battery Analyzer upon discharge with a

110 mΩ resistor. Nail penetration was performed using a 2.7 mm diameter, 38 mm long 304 stainless steel nail. In both experiments cell temperature response was documented using type-K gage-40 thermocouple affixed to the cell case by polyimide tape. Cells used in abuse testing were preconditioned by cycling twice at C/45 between 3.0 V and 4.2 V, charged to 33.1 mAh capacity, and then given a 24 hr resting period prior to short circuit initiation.

Electrochemical performance and abuse characterizations were compared against commercially-produced LIR2032 format LCO / graphite 40 mAh cells with traditional LC electrode stack assemblies, purchased from AA Portable Power Corporation. They were subjected to identical electrochemical conditioning, abuse testing, and mass / dimension measurement protocols as the cells assembled with IPC electrodes.

4.2.3 Mechanical property characterization

Measurements of force and displacement were made to elucidate the roles of current collector reinforcements, electroactive matrix layers, and multilayer electrode assembly orientations using an Instron 5582 Testing Machine. Aluminum and copper foil current collectors as well as LCO and graphite LC electrodes were purchased from MTI Corporation for comparison with the porous metal current collectors and the IPC electrode units.

Shear testing was performed on individual current collector and electrode layers using a custom-made load cell that slowly compressed the center of 1.98 cm^2 circular samples with a 3.2 mm diameter piston into a 3.8 mm diameter gap at a rate of 10 $\mu m.s^{-1}$, until fracture occurred. Three-point bending was performed on individual electrode layers, as well as multilayer stacks with separator interfaces, all precut to widths of 12.5 mm and loaded at a rate of 10 $\mu m.s^{-1}$ across

the center of a 12.5 mm support span. Multilayer assemblies were compared on 2.5 mm thickness basis. The assemblies were formed with cathode / separator / anode / separator alternating bilayers vacuum-sealed in polypropylene bags to secure interlayer contact. The intended testing thickness was produced with 8 and 2 electrode bilayer assemblies for LC and IPC electrodes, respectively.

4.3 Results

4.3.1 High aerial capacity electrode fabrication

The metal foam current collectors are impregnated with slurries exhibiting high active material loading densities to produce the IPC electrodes. The slurries have LCO and graphite loadings of ~1.5 $g.mL^{-1}$ and ~0.7 $g.mL^{-1}$, enabling realization of high aerial capacity electrodes with active material loadings of 138 $mg.cm^{-2}$ and 55 $mg.cm^{-2}$ after drying and calendering for cathode and anode, respectively. The optimized slurry processing mixing procedure, ultrasonic power application sequence, and processing temperature results for 3.5 mL processing solvent bases are depicted in Figure 4.1.

4.3.2 Electrochemical performance evaluation

The IPC electrode cells achieve a high reversible capacity of 16.7 $mAh.cm^{-2}$ following 3 formation cycles when charged and discharged at 0.375 $mA.cm^{-2}$, approaching 99.4% columbic efficiency after 10 cycles. This full cell capacity equates to 121 $mAh.g^{-1}$ of LCO, indicating suitable usage of the large active material loading, after irreversible capacity loss to solid

electrolyte interface formation is considered. At higher discharge rates, the cells exhibit diminished discharge capacity capabilities. Reported in Figure 4.2, these performance characteristics are consistent with other investigations on thick IPC electrodes with porous metal current collectors [120,121], but respectable gains in aerial and volumetric electrode capacities are demonstrated, as facilitated by advanced slurry processing procedures.

Commercially-produced LIR2032 units with LC electrodes of the same LCO / graphite chemistry exhibit better rate performance at room temperature. In terms of energy densities, the LC electrode stack assembly is 11% higher with respect to mass, while the IPC electrode stack assembly is 22% higher with respect to volume, as noted in Table 4.1.

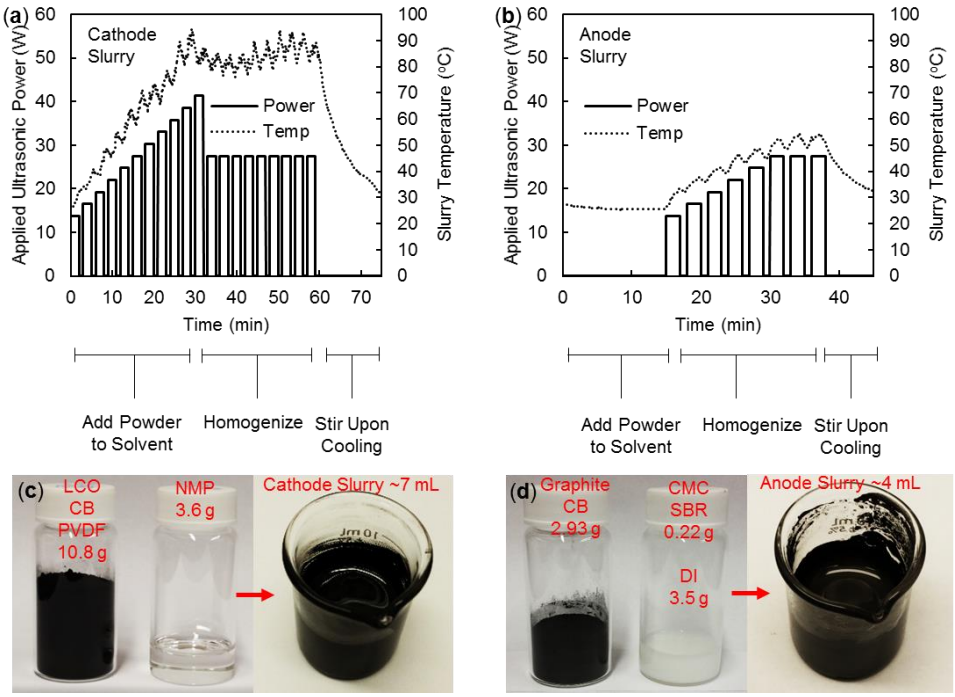


Figure 4.1 Ultrasonic power application, mixing sequence, and consequent temperature dynamics of (**a**) cathode and (**b**) anode slurries processed using QSonica Q55 Sonicator with 3.2 mm diameter submersible ultrasonic horn homogenized in 10 mL Pyrex beakers. (**c**) Images of the $LiCoO_2$ (LCO), carbon black (CB), and polyvinylidene fluoride (PVDF) materials dispersed in N-methyl-2-pyrrolidone (NMP) to produce finished high-density cathode slurry. (**d**) Images of graphite, CB, carboxymethyl cellulose (CMC), and styrene-butadiene rubber (SBR) dispersed in deionized water (DI) to produce finished high-density anode slurry.

Table 4.1 Electrochemical characteristics of LIR2032 cells with laminate composite (LC) electrodes and interpenetrating phase composite (IPC) electrodes.

Assembly	LIR2032 w/ LC Electrodes	LIR2032 w/ IPC Electrodes
Cathode		
Active Material	LCO	LCO
Binder	NMP soluble (e.g. PVDF)	PVDF
Current Collector	Aluminum foil (15 µm thick)	Aluminum foam
Overall Thickness	57.5 µm (each side)	600 µm
Active Material Mass	--	274 mg
Total Mass (Dry)	--	320 mg
Anode		
Active Material	Graphite	Graphite
Binder	Water soluble (e.g. CMC)	CMC:SBR 2:3 w:w
Current Collector	Copper foil (10 µm)	Copper foam
Overall Thickness	67.5 µm (each side)	600 µm
Active Material Mass	--	109 mg
Total Mass (Dry)	--	198 mg
Full Cell		
Production Means	Commercial Factory	Handmade
Charge / Discharge Time	10 hr	45 hr
Voltage Range	3.0 V – 4.2 V	3.0 V – 4.2 V
Discharge Capacity	40.0 mAh	33.1 mAh
Discharge Energy	153 mWh	124 mWh
Electrode Area	7.70 cm^2	1.98 cm^2
Electrode Orientation	Biaxial	Uniaxial
Electrode Stack Thickness	2.52 mm	1.24 mm
Electrode Stack Volume	370 µL	245 µL
Total Electrode Stack Mass	781 mg	696 mg
Volumetric Energy Density	414 Wh/L	506 Wh/L
Gravimetric Energy Density	196 Wh/kg	178 Wh/kg

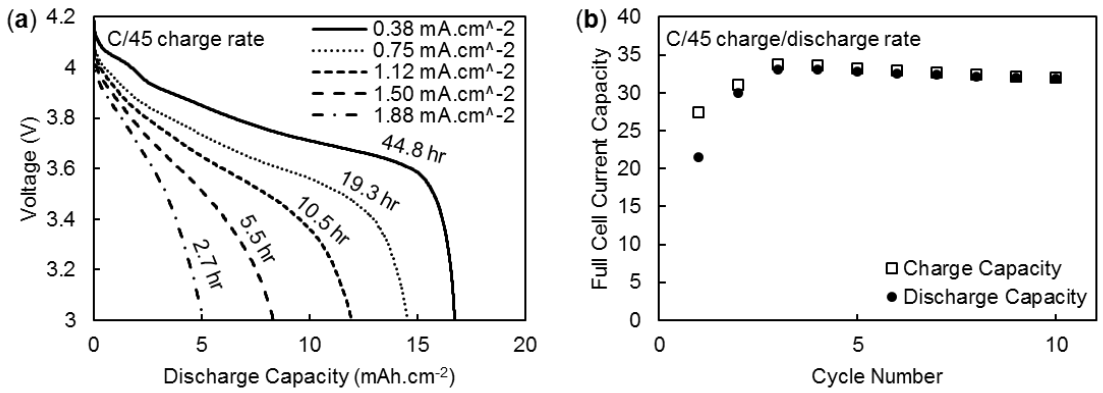


Figure 4.2 (**a**) Voltage / capacity profiles and times for increasing discharge current rates and (**b**) formation / cycling capacity for 600 µm thick, 1.98 cm^2 interpenetrating phase composite $LiCoO_2$ / graphite electrodes arranged in uniaxial full cell orientation in LIR2032 format coin cells.

4.3.3 External short circuit and nail penetration responses

As postulated, thick IPC electrodes supported by porous metal current collectors are considerably safer than traditional LC units with metal foil current collectors. Upon external shorting, the electrically-controlled capacitive discharge current measured for the modified IPC cells is only 38% of the reference LC cells in the first 3 seconds after initiation. Due to the increased thickness, the continued ionically-controlled, sustained discharge current averages only 14% of the reference values over the following 5 minutes. These joule heating dynamics limit the maximum peak temperature increase to just 25% of the reference external shorting experiments, with consistent results observed in nail penetration testing. For fair comparison, both traditional LC electrode and modified IPC electrode units are charged to the current capacity of 33.1 mAh. Short circuit current dynamics and cell temperature responses are shown alongside images of the electrodes in Figure 4.3.

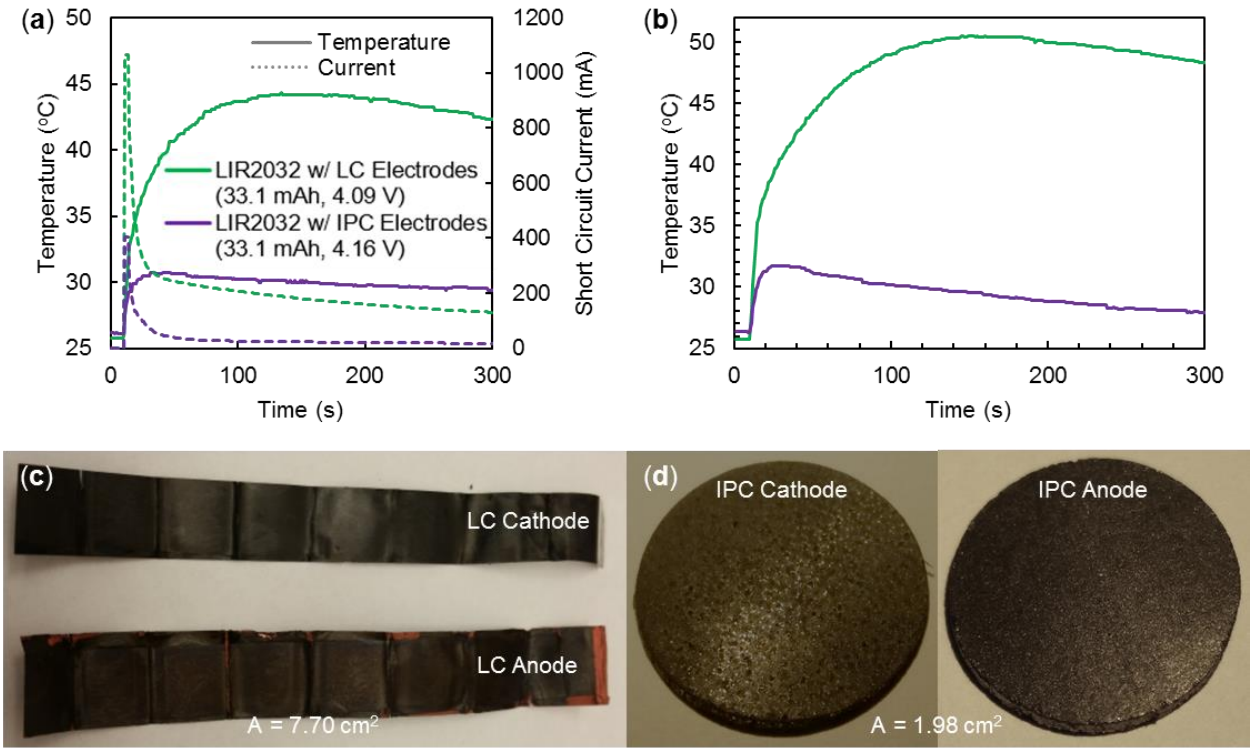


Figure 4.3 (**a**) External short circuit temperature response and discharge current dynamics of LIR2032 coin cells with laminate composite (LC) electrodes and interpenetrating phase composite (IPC) electrodes. (**b**) Nail penetration temperature response. Images of (**c**) LC electrodes and (**d**) IPC electrodes used for electrochemical evaluation and abuse testing.

4.3.4 Shear testing

The force-displacement curves show the IPC electrodes are more robust against shear loading than the LC electrodes, withstanding forces more than two times greater prior to fracture. For the IPC electrodes, complete fracture occurs upon failure such that the damaged area is electrically disconnected from the remaining electrode, while the metal foil current collectors and LC electrodes exhibit only partial breakage. Fracture responses demonstrating complete separation of the damaged area are favorable in abusive impact conditions from a safety standpoint, as discussed in previous report [74]. In both LC and IPC electrodes, the anodes exhibit higher

maximum loads and post-yield displacements than the cathodes. The mechanical response results and images after testing are shown in Figure 4.4.

For both cathode and anode, the metal foil current collectors and reference LC electrodes behave largely the same, demonstrating that the electroactive matrix coated layers do not make significant contributions to the mechanical response under abusive shear, and the metal foil reinforcements carry the bulk of the mechanical load. Conversely, the porous metal current collectors experience notably larger post-yield displacements under less stress than the modified IPC electrodes, which withstand larger mechanical loads prior to fracture. This result indicates the electroactive matrix has a consequential influence on the shear response in the IPC orientation, sharing the mechanical load with the porous metal current collector reinforcements.

4.3.5 Three-point bending

In three-point bending, the individual IPC electrodes demonstrate bending stiffnesses of 4.9 $N.mm^{-1}$ and 5.9 $N.mm^{-1}$ for cathode and anode respectively, an order of magnitude greater than the LC electrodes which exhibit 0.37 $N.mm^{-1}$ and 0.14 $N.mm^{-1}$. These extensive properties persist despite the larger flexural modulus of the LC electrodes, exhibiting 6.87 GPa and 1.80 GPa for the cathode and anode, respectively, compared to just 0.83 GPa and 1.01 GPa for the IPC electrodes. The result demonstrates that electrode thickness and component orientation can have a greater influence on mechanical performance characteristics than the intensive material properties of those individual components. Furthermore, the lower flexural modulus of the IPC electrodes suggests the low-tensile-modulus electroactive matrices play greater roles in load-bearing functionality than

they do in LC electrodes, which is consistent with the observations noted in shear testing. Results of the three-point bending tests are depicted in Figure 4.5.

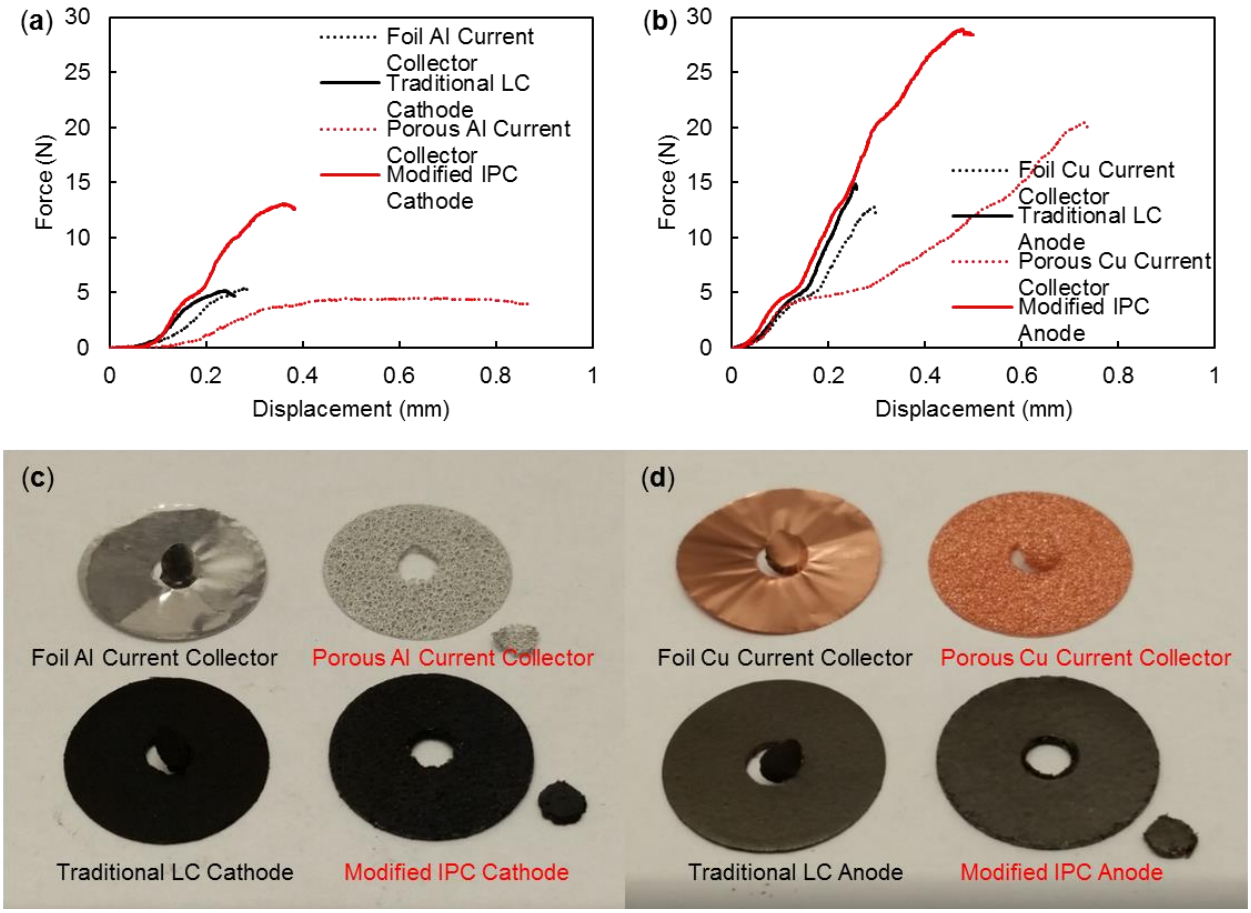


Figure 4.4 Shear force-displacement profiles of current collector and electrode 1.98 cm^2 samples with a 3.2 mm diameter piston pressing the geometric centers into a 3.8 mm diameter gap at a rate of 10 $\mu m.s^{-1}$ for (**a**) aluminum current collectors and cathodes as well as (**b**) copper current collectors and anodes in laminate composite (LC) and interpenetrating phase composite (IPC) formations. Images show fracture of (**c**) cathodes, (**d**) anodes, and current collectors after testing.

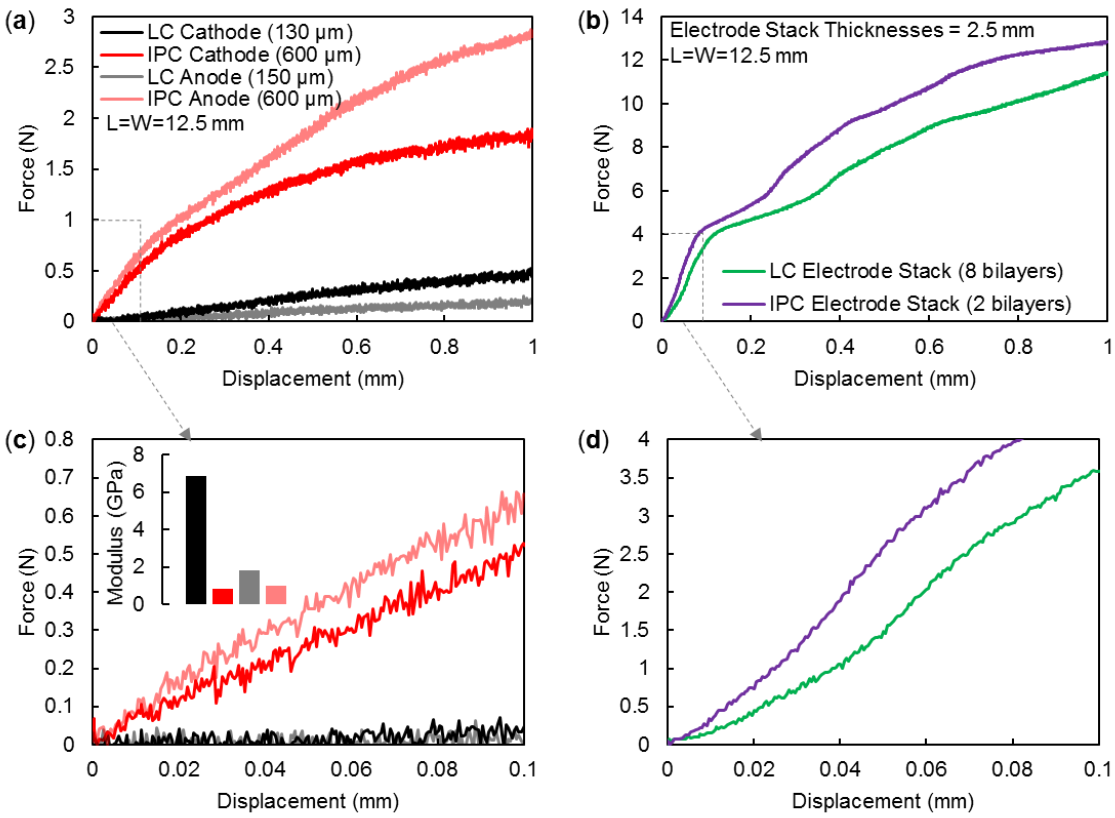


Figure 4.5 (**a**) Three-point bending force-displacement profiles for individual laminate composite (LC) and interpenetrating phase composite (IPC) electrodes and (**b**) electrode stack assemblies totaling 2.5 mm thickness, all tested with 12.5 mm width and support length loaded at a rate of 10 µm.s^{-1}. Enhanced images of regions used to determine (**c**) the flexural modulus for the individual electrodes and (**d**) bending stiffness for the multilayer assemblies.

When multiple LC or IPC layers are stacked with separators and vacuum-sealed together in bags, as is characteristic of practical LIB pouch cell formats, three-point bending of the electrode stack assemblies are evaluated on equivalent 2.5 mm thickness basis. The force-displacement curves are fairly linear up to 75 µm displacement, equating 3% deflection, but not perfectly so, likely due to interlayer sliding and reorientation under stress, which is more pronounced in the LC stacks which have a more layers. Electrode assemblies exhibit average bending stiffnesses of 34.2 N.mm^{-1} for the LC electrodes and 48.8 N.mm^{-1} for the IPC electrodes until a yield load of 3.5 N is

reached, at which point the weaker electroactive matrix phases begin to fail under the compression. This result reaffirms that IPC electrode assemblies can be preferable to the LC electrodes when structural functions are to be considered. That said, it should be noted that in practice, mechanical properties are also influenced by cell orientation, formation techniques, state-of-charge, and a variety of other factors.

4.4 Discussion

4.4.1 Balancing rate capability and short circuit safety

The safety characteristics of LIB cells are closely coupled to their discharge rate capabilities. Prior to discharge initiation, the concentration of lithium-ions in electrolyte is uniform across the characteristic length of the cell. When discharge begins, ions in the electrolyte of the cathode region are uptaken by the LCO active material particles, while simultaneously, ions are liberated from the graphite active material particles into the electrolyte of the anode region. In this manner, a concentration imbalance forms a chemical potential gradient which drives mass transfer of lithium-ions through the electrolyte across the separator membrane from the anode region to the cathode region. The rate these ions are capable of moving is dictated by their diffusivity in the organic electrolyte where they are located. The pathlength charge-carrying lithium-ions need to travel in electrolyte to balance the concentration difference primarily depends on the orientation of the electrodes.

When the discharge current is fast enough to remove ions from the electrolyte of the cathode region more quickly than they are replenished by ions crossing the separator interface

from the anode region, electrolyte polarization impedance manifests. Under excessive constant current discharge control, the consequent overpotential bias causes the lower operating range 3.0 V cutoff to be realized with reduced current capacity discharged, defining the cells' sustained rate capabilities in many cases. If a low resistance short circuit discharge pathway is formed, the reservoir of charge-transferable lithium-ions in the electrolyte of the cathode region is rapidly depleted in a brief capacitive joule heating event. The short circuit current is subsequently throttled to lower rates dependent on the ions' abilities to traverse the separator interface from the anode region to recombine with electrons in the LCO active material particles [105].

The electrode thickness has a significant role in both rate capability and short circuit response. It is standard practice to use LC electrodes with thinner electroactive matrix layers to minimize the pathlength that ions would need to travel to retain low polarization impedances, thus increasing sustained rate capabilities. This characteristic is common in power cells, but reduces energy-storing active material mass relative to the contributions of the current collector reinforcements, sacrificing energy density [120]. The thick IPC electrodes examined here take the opposite approach, increasing the pathlength for the purpose of exacerbating polarization impedances in a short circuit event to curb sustained joule heating rate responses.

Electrodes should be thin enough to realize the rate capabilities required for optimal performance of the devices they are intended to power, but no thinner. Rate capabilities in excess of what is needed incur unnecessary added risk without further benefit. Porous metal current collectors allow for versatility in designing LIB cells with fast rate capabilities, long run-times, and balanced intermediates. IPC electrodes have shown they can retain full use of all active materials loaded at thicknesses as little as 100 μm and as high as 1200 μm [120,127]. Using thin IPC electrodes with high current collector pore densities has been shown to improve rate

capabilities for $LiFePO_4$ electrodes by enhancing electron conduction [126], which is useful for devices like heavy-duty power tools. Using thick, robust IPC electrodes to continuously supply low power over long run-times could greatly improve safety margins in applications where they are of the utmost importance, as is demanded of advanced communication and tracking electronics carried by dismounted soldiers with 72 hr mission life requirements [129]. Optimal thicknesses for devices with intermediate power requirements, like smart phones and other personal electronics, could be selected to satisfy power demands with the least risk retention.

4.4.2 Prospects and challenges for multifunctional application

The IPC electrodes formed with porous metal current collectors show greater bending stiffness and volumetric energy density than units with comparable current capacity and shape constructed with LC electrodes, in addition to being significantly safer in short circuit events. These characteristics are desirable to have in devices with greater degrees of cell integration. Such improvements are profound considering the LIB components have simply been reoriented, and the chemical make-up of the cells has not been altered. Thus, modification with porous metal current collectors could be considered for many modern or future LIB chemistries that would otherwise use standard aluminum or copper foil current collector materials. Improvements in safety will become increasingly important as advanced chemical development techniques continue to improve the inherent energy density of active materials, which incur additional risk. That said, optimization of the porous metal current collector geometry and further development of the electroactive matrices is necessary to be viable for multifunctional implementation, such that the LIB cells can carry a physical load while retaining sustainable electrochemical storage functionality.

Larger pore densities and thread thicknesses of porous metals increase the bending stiffness of IPCs, but tend to have lower porosity and larger masses [125]. In this demonstration, the ~45 PPI pore density aluminum foam current collector accounts for less than 8 wt% of the lower stiffness cathode, while the ~105 PPI pore density copper foam current collector accounts for more than 38 wt% of the higher stiffness anode. Depending on the structural load the LIB needs carry, the aluminum foam's pore density and thread thickness could be increased to impart greater bending stiffness, or the copper foam's pore density and thread thickness could be decreased to improve the gravimetric energy density, which is slightly lower than the reference LC electrode cells in this example. If thinner electrodes are used, that would notably influence the bending stiffness, and current collectors may be precut considering the intended thicknesses of the fully formed IPC electrodes in order to retain their characteristic mechanical and mass contributions to the heterogeneous electrode structures. However, even if the gravimetric energy density of the IPC cell is lower than a traditional LC cell, it could still be preferable if the overall mass of the cell is reduced because it is able to perform multiple functions, replacing redundant load-bearing components, or reduced volume is a more important design factor [116].

For structural LIBs using IPC electrode orientations to be practical, they must perform their primary function as electrochemical storage devices dutifully when subjected to physical-loading that is not normally imposed on traditional LIB cells. LIB performance commonly degrades over time from interfacial debonding between the binder phase and active material particles within the electroactive matrix, as well as delamination of the electroactive matrix layers from the current collector reinforcements due to fatigue experienced upon electrochemical cycling. This mode of failure is particularly concerning when considering the prospect that a LIB would be subject to continuous static loading and dynamic mechanical stress cycles in the field that could cause

debonding, limiting the cyclability to be shorter than it would under unstressed conditions. Additionally, unmitigated strain the IPC electrodes are exposed to could cause the sharp edges of the porous metal current collectors to pierce the separator layers and cause a short circuit. While such events would be much less dangerous than if they were to occur in traditional LC units, they still need to be treated as a risk factor. As such, the electroactive matrix and separator layers need to be strengthened for the IPC units to be realistically considered for multifunctional implementation.

The mechanical tests performed in this study show that the electroactive matrix phase plays a notable role in the load-bearing responsibility of the IPC electrode. The tensile modulus and adhesive strength of the electroactive matrices are largely imparted by the binder phases, which need to be improved tolerate mechanical stress. The CMC binder of the anode layers has good adhesive strength and its SBR component facilitates a degree of compliance when strain is experienced. However, the PVDF binder of the cathode layers has relatively poor mechanical properties, especially upon wetting by organic carbonate-based electrolyte, and is more likely to fail [130]. Additionally, thin polypropylene separators are not puncture resistant. The fact that the binder phases and separator layers of IPC units would assume undue burden in structural applications, they need to be replaced with more robust materials. Solid-state and gel electrolyte separator layers have received considerable research attention [131], and next generation binders developed in the pursuit of large-strain-inducing active materials and environmentally friendly processing could be adapted to support structural LIB designs [130,132]. With supporting modifications, the porous metal current collectors facilitating thick electrodes showing excellent abuse tolerance are promising materials for further development of multifunctional LIBs.

4.5 Conclusion

Porous metal current collectors facilitate formation of thick, high aerial capacity lithium-ion battery electrodes with improved safety and unique mechanical characteristics. By reorienting the electrode materials from laminate composite into interpenetrating phase composite formations, short circuit currents and joule heating rates are significantly suppressed to prevent temperature accruement that could lead to thermal runaway in physically abusive events. Increasing thickness also imparts greater flexural bending stiffness to the electrodes which make them attractive for multifunctional battery applications, where they might assist in load-bearing structural functions to improve overall device performance and safety margins. Simultaneously, energy density is increased by reducing volumetric contributions from nonelectrochemical support components such as separators, due to the reduced geometric interfacial area. A technical challenge of this safety-first design approach is that it sacrifices rate capability, which precludes its use in certain applications. Further optimization of the electrode thicknesses, component orientations and materials are discussed to satisfy the different needs of battery-operated devices, improving safety margins, and facilitating multifunctional structural implementation.

4.6 Acknowledgements

Chapter 4, in full, is a reprint of the material submitted for publication. Daniel Noelle, Meng Wang, and Yu Qiao. Improved safety and mechanical characterizations of thick lithium-ion battery electrodes structured with porous metal current collectors. The dissertation author was the primary investigator and first author of the paper.

Chapter 5 Summary and future work

Modern lithium-ion battery (LIB) safety infrastructures demand improvements to be resilient against abuse in the most dangerous scenarios. LIB fires in Tesla Model S vehicles, Samsung Galaxy Note 7 smartphones, and other personal electronics over recent years have highlighted the risks that persist in spite of decades of academic research and commercial development seeking to make LIBs safe, demonstrating gaps in technological achievement remain to be filled. A fundamental understanding of the nature of those challenges is essential to inform effective solutions. Enlightened knowledge of the problems aids in devising strategies which address the dangers directly. A primary goal of this narrative is to clarify the detailed progression and significance of events which beset a LIB in severe short circuit events. Considering the fundamental joule heating dynamics, several safe-cell design strategies and technologies are discussed to mitigate thermal runaway events in the earliest stages of LIB failure.

The short circuit joule heating dynamics are measured experimentally upon nail penetration of LIR2450 $LiCoO_2$ / graphite 120 mAh coin cells. The cell system demonstrates ideal energy storage, mechanical, and heat transfer characteristics for analyzing discharge over resolute temperature and time scales without convolution from other exothermic decomposition phenomena characteristic of thermal runaway at excessive temperatures. Via analysis of the measured nail penetration temperature response with a simple convective heat transfer relation, a distinct high-power joule heating feature is identified immediately upon short circuit initiation, lasting a brief few seconds before subsequent throttling to a lower sustained power for several minutes. As joule heating rate is inversely proportional to the cell's internal resistance, direct current analysis over a wide range of currents is used to elucidate the reasons for these dynamics.

Upon direct current application, overpotentials are observed in the operating voltage readings showing an immediate ohmic potential drop followed by added overpotential manifestations upon polarization over several minutes. The voltage dynamics exhibit predictable behavior at low current rates but adopt increasingly non-linear polarization overpotential responses at elevated current rates. An electrolyte resistivity model is postulated in terms of charge-carrier concentration, temperature, permittivity, and viscosity for comparison. The study suggests that as discharge time proceeds at very high current rates, the reservoir of lithium-ions in the electrolyte of the cathode region is rapidly depleted, requiring they traverse longer distances from the electrolyte of the anode region to facilitate charge transfer thereafter.

Internal impedance in lithium-ion cells is discharge rate limiting in short circuit scenarios. Resistance dynamics ascertained through analysis the nail penetration temperature response signal show rapid polarization of the cell occurs following the initial powerful joule heating phenomenon. It is determined that this is due to rapid uptake of lithium-ions from the electrolyte of the cathode region in a capacitive discharge which is electrically controlled, and the subsequently throttled current rate is limited by the low electrolyte conductivity of lithium-ion deficient cathode region. This information is used to predict the degree to which internal impedance contributing elements of the LIB could be forcibly exacerbated to curb joule heating and consequent cell temperature, aiding in identification of effective thermal runaway mitigation strategies targeting appropriate LIB components acting on relevant time scales.

The fundamental conclusion of this in-depth experimental analysis of short circuit discharge event progression is that to suppress the ohmically-controlled capacitive discharge feature, efforts to increase electrical resistances immediately upon shorting should be prioritized,

while simultaneously electrolyte should be targeted to hinder continuous polarization-controlled discharge thereafter.

Primary targets for addressing the ohmically-controlled capacitive discharge feature include the electrically-conductive current collectors and carbon black components of the otherwise electrically-resistive cathode composite. Impedance exacerbation features should be inherent to the LIB structure, acting immediately upon short circuit initiation if they are to successfully suppress the capacitive discharge power. Strategically-weakened current collector reinforcements debossed with embrittling safety patterns and large carbon black particles promoting cracking and debonding of the electroactive matrix are two such embodiments demonstrating success in mechanical impact events.

Strategies and development of LIB features capable of suppressing the polarization-controlled sustained discharge feature is the focus of this narrative. The goal is disruption of the ion transfer through the electrolyte as quickly and effectively as possible by taking effect upon short circuit initiation at low temperatures. Two strategies are considered: active poisoning of the electrolyte so it is no longer conductive using aggressive reaction agents encapsulated in breakable containers; and increasing the pathlength ions must traverse to complete charge transfer by reorienting the electrodes into thick interpenetrating phase composite formations using porous metal current collectors.

Aggressive electrolyte poisons are identified considering the postulated electrolyte conductivity model used in evaluating the nature of polarization upon shorting. Raising electrolyte viscosity by dilution with diols commonly used in thermal management applications notably hinders charge-carrying ion diffusivity. However, large volumes are required for encapsulation within a LIB cell which would impose unacceptable sacrifices to energy density. Diamines

demonstrate the ability to rapidly polymerize the high-permittivity ethylene carbonate component of traditional LIB electrolytes with low concentrations, causing the liquids to become non-permitting solids. They are shown to be excellent candidates for encapsulation in breakable containers. Diol and diamine mixtures show synergistic poisoning character with unique thermal transport and anticorrosion properties which present opportunities to perform multiple functions.

Poison delivery devices are discussed for further investigation upon demonstration of one embodiment which incorporates the shutdown fluids into a LIB case structure rigged to penetrate the electrode stack upon mechanical impact. Potential for modification of battery thermal management systems in electric vehicles as advanced shutdown features is identified considering the diol and diamine poisoning characteristics and recognizing their innate presence in large volumes within the existing LIB pack infrastructure for temperature control applications.

Reorientation of the LIB electrodes into thick interpenetrating phase composite formations using porous metal current collectors shows the profound influence of structural design on LIB safety. By increasing the ion transport pathlength, the LIBs become more susceptible to polarization overpotentials as it becomes more difficult for the electrolyte to maintain ion concentration uniformity across the characteristic length of the cell. This phenomenon diminishes a LIB's rate capabilities, which consequently limits their power in a short circuit failure. Optimizing electrode thicknesses to be thin enough to dutifully perform at the rate capabilities required for the devices they are intended to power, but be as thick as possible so the ion transport pathlength is maximized upon shorting, is a simple and intuitive safe-cell design strategy worth further consideration.

Mechanical testing of thick interpenetrating phase composite electrodes shows them to be stiffer in three-point bending and stronger against shear with more favorable fracture responses

than traditional laminate composite electrodes. The enhanced robustness of the electrodes formed with porous metal current collectors make them more resilient against mechanical loading, such that they might retain form and avoid shorting in some physically stressful scenarios electrodes with metal foil current collectors would not. The most straightforward way to avoid thermal runaway is to prevent the short circuit from occurring in the first place.

In summary, this thesis elucidates the fundamental joule heating, resistance, and polarization dynamics of short circuit progression in the earliest stages of LIB failure, which can lead to thermal runaway in modern LIB chemistries. The critical components contributing to the sequence of joule heating events are identified and targeted for development of unique shutdown features capable of exacerbating the internal resistance on appropriate timescales. Using this knowledge, safe-cell design strategies concerning electrolyte poisoning and ion transport pathway reorientation are devised and shown to be effective in experimental demonstrations, reinforcing the importance of understanding the fundamentals of a challenge to inform better solutions.

Lithium-ion battery safety and robustness will be increasingly important as next-generation LIB chemistries enable higher specific energies with larger cell sizes and greater degrees of device integration, imposing increasingly tough challenges. This investigation focuses on the short circuit characteristics of modern LIB chemistries and components to inform considerations for novel safety designs, but future investigations of more dangerous chemistries and components should be tailored to the specific units and LIB-powered devices of interest. Furthermore, as LIB chemistries approach the theoretical limits of their capabilities, advanced designs will be necessary to continue reducing mass and volume, such as multifunctional LIBs for electric vehicles.

Prioritizing safety-first, structurally-robust LIB designs is a novel approach for increasing electric vehicle range, as well as improving image and perception to facilitate greater marketplace

acceptance. Structural robustness of LIBs has been secondary to electrochemical design, which is part of the reason they can be so dangerous. Nonelectrochemical components give LIBs their essential form, contributing considerable mass and volume to vehicle systems which is often overlooked. Giving greater attention to the selection and optimization of those nonelectrochemical components can make LIBs stiffer and stronger so they can withstand greater abuse, protecting themselves rather than being dependent on heavy primary protection structures. With considerable improvements, they may even carry a physical load, replacing redundant structural components in the vehicle frame. With continued dedication to understanding the research fundamentals in pursuit of the larger picture, structural LIB development for electric vehicles using next-generation LIB chemistries is the next step in the progression of this investigation to increase driving range with improved safety designs.

References

[1] E. Musk, Model S Fire, (2013). https://www.tesla.com/blog/model-s-fire.

[2] B. Vlasic, Car Fire a Test for High-Flying Tesla, New York Times. (2013). http://www.nytimes.com/2013/10/04/business/car-fire-a-test-for-high-flying-tesla.html.

[3] P. Lebeau, Electric car blaze raises new questions for Tesla, NBC News. (2013). https://www.nbcnews.com/business/electric-car-blaze-raises-questions-tesla-8c11327622.

[4] P. Valdes-Dapena, Third Tesla Model S catches fire after crash, CNN Money. (2013). http://money.cnn.com/2013/11/07/autos/tesla-fire/index.html.

[5] S. Mufson, Tesla Model S cars under probe for possible defect that can cause fire, Washington Post. (2013). https://www.washingtonpost.com/business/economy/tesla-model-s-cars-under-probe-for-possible-defect-that-can-cause-fire/2013/11/19/580d8212-5139-11e3-a7f0-b790929232e1_story.html?utm_term=.dd083c586909.

[6] S. Abada, G. Marlair, A. Lecocq, M. Petit, V. Sauvant-Moynot, F. Huet, Safety focused modeling of lithium-ion batteries: A review, J. Power Sources. 306 (2016) 178–192. doi:10.1016/j.jpowsour.2015.11.100.

[7] DOT Bans All Samsung Galaxy Note7 Phones from Airplanes, U.S. Dep. Transp. (2016). https://www.transportation.gov/briefing-room/dot-bans-all-samsung-galaxy-note7-phones-airplanes.

[8] Batteries Carried by Airline Passengers Frequently Asked Questions, Fed. Aviat. Adm. (2016). https://www.faa.gov/about/office_org/headquarters_offices/ash/ash_programs/hazmat/passenger_info/media/airline_passengers_and_batteries.pdf.

[9] L. McKenna, Electronic Cigarette Fires and Explosions in the United States 2009-2016, U.S. Fire Adm. (2017). https://www.usfa.fema.gov/downloads/pdf/publications/electronic_cigarettes.pdf.

[10] D. Lisbona, T. Snee, A review of hazards associated with primary lithium and lithium-ion batteries, Process Saf. Environ. Prot. 89 (2011) 434–442. doi:10.1016/j.psep.2011.06.022.

[11] F.R. Kalhammer, H. Kamath, M. Duvall, M. Alexander, B. Jungers, Plug-In Hybrid Electric Vehicles: Promise, Issues and Prospects, in: EVS24 Int. Batter. Hybrid Fuel Cell Electr. Veh. Symp., Stavanger, Norway, 2009: pp. 1–11. http://www.e-mobile.ch/pdf/2010/EVS-24-5040526.pdf.

[12] O. Egbue, S. Long, Barriers to widespread adoption of electric vehicles: An analysis of consumer attitudes and perceptions, Energy Policy. 48 (2012) 717–729. doi:10.1016/j.enpol.2012.06.009.

[13] H. Ma, F. Balthasar, N. Tait, X. Riera-Palou, A. Harrison, A new comparison between the life cycle greenhouse gas emissions of battery electric vehicles and internal combustion vehicles, Energy Policy. 44 (2012) 160–173. doi:10.1016/j.enpol.2012.01.034.

[14] P. Lebeau, Yet another Model S fire puts heat on Tesla, CNBC. (2013). https://www.cnbc.com/2013/11/07/yet-another-model-s-fire-puts-heat-on-tesla.html.

[15] J. Mullen, M. Thompson, Samsung takes $10 billion hit to end Galaxy Note 7 fiasco, CNN Tech. (2016). http://money.cnn.com/2016/10/11/technology/samsung-galaxy-note-7-what-next/index.html.

[16] J. Stempel, Florida man sues Samsung, says Galaxy Note 7 exploded, Reuters. (2016). https://www.reuters.com/article/us-samsung-elec-smartphones-lawsuit/florida-man-sues-samsung-says-galaxy-note-7-exploded-idUSKCN11M2E7?feedType=RSS&feedName=domesticNews&utm_medium=Social&utm_source=Twitter.

[17] International Energy Agency, Global EV Outlook 2017: Two million and counting, IEA Publ. (2017) 1–71. doi:10.1787/9789264278882-en.

[18] G. Berckmans, M. Messagie, J. Smekens, N. Omar, L. Vanhaverbeke, J. Van Mierlo, Cost projection of state of the art lithium-ion batteries for electric vehicles up to 2030, Energies. 10 (2017). doi:10.3390/en10091314.

[19] P. Ping, Q. Wang, P. Huang, J. Sun, C. Chen, Thermal behaviour analysis of lithium-ion battery at elevated temperature using deconvolution method, Appl. Energy. 129 (2014) 261–273. doi:10.1016/j.apenergy.2014.04.092.

[20] R. Spotnitz, J. Franklin, Abuse behavior of high-power, lithium-ion cells, J. Power Sources. 113 (2003) 81–100. doi:10.1016/S0378-7753(02)00488-3.

[21] L. Lu, J. Hua, A review on the key issues for lithium-ion battery management in electric vehicles, J. Power Sources. 226 (2015) 272–288. doi:10.1016/j.jpowsour.2012.10.060.

[22] S. Basu, K.S. Hariharan, S. Mayya, T. Song, D. Kee, Coupled electrochemical thermal modelling of a novel Li-ion battery pack thermal management system, Appl. Energy. 181 (2016) 1–13. doi:10.1016/j.apenergy.2016.08.049.

[23] C. Ashtiani, Analysis of Battery Safety and Hazards' Risk Mitigation, ECS Trans. 11 (2008) 1–11. doi:10.1149/1.2897967.

[24] T.G. Zavalis, M. Behm, G. Lindbergh, Investigation of Short-Circuit Scenarios in a Lithium-Ion Battery Cell, J. Electrochem. Soc. 159 (2012) A848. doi:10.1149/2.096206jes.

[25] X. Feng, L. Lu, M. Ouyang, J. Li, X. He, A 3D thermal runaway propagation model for a large format lithium ion battery module, Energy. 115 (2016) 194–208. doi:10.1016/j.energy.2016.08.094.

[26] H. Uwai, A. Isoda, H. Ichikawa, N. Takahashi, Development of body structure for crash safety of the newly designed electric vehicle, in: 22nd ESV Conf. Proc., Washington, D.C., 2011: pp. 1–7.

[27] J. Kukreja, T. Nguyen, T. Siegmund, W. Chen, W. Tsutsui, K. Balakrishnan, H. Liao, N. Parab, Crash analysis of a conceptual electric vehicle with a damage tolerant battery pack, Extrem. Mech. Lett. 9 (2016) 371–378. doi:10.1016/j.eml.2016.05.004.

[28] J. Istiyanto, D. a. Sumarsono, M.S. Utomo, G. Kiswanto, A.S. Baskoro, S. Supriadi, Development of platform structure as protection to lithium batteries in electric vehicle during crash impact, in: 2013 Jt. Int. Conf. Rural Inf. Commun. Technol. Electr. Technol. (rICT ICeV-T), Bandung-Bali, Indonesia, 2013: pp. 1–8. doi:10.1109/rICT-ICeVT.2013.6741552.

[29] M. Wang, L. Zhu, A.V. Le, D.J. Noelle, Y. Shi, Y. Zhong, F. Hao, X. Chen, Y. Qiao, A multifunctional battery module design for electric vehicle, J. Mod. Transp. 25 (2017) 218–222. doi:10.1007/s40534-017-0144-8.

[30] F. Hao, X. Lu, Y. Qiao, X. Chen, Crashworthiness analysis of electric vehicle with energy-absorbing battery modules, J. Eng. Mater. Technol. 139 (2016) 1–4. doi:10.1115/1.4035498.

[31] P.G. Balakrishnan, R. Ramesh, T. Prem Kumar, Safety mechanisms in lithium-ion batteries, J. Power Sources. 155 (2006) 401–414. doi:10.1016/j.jpowsour.2005.12.002.

[32] Q. Wang, P. Ping, X. Zhao, G. Chu, J. Sun, C. Chen, Thermal runaway caused fire and explosion of lithium ion battery, J. Power Sources. 208 (2012) 210–224. doi:10.1016/j.jpowsour.2012.02.038.

[33] S.S. Zhang, A review on electrolyte additives for lithium-ion batteries, J. Power Sources. 162 (2006) 1379–1394. doi:10.1016/j.jpowsour.2006.07.074.

[34] L. Xia, D. Wang, H. Yang, Y. Cao, X. Ai, An electrolyte additive for thermal shutdown protection of Li-ion batteries, Electrochem. Commun. 25 (2012) 98–100. doi:10.1016/j.elecom.2012.09.038.

[35] B. Chaloner-Gill, I. Olsen, US5580680, 1996.

[36] C.L. Cheng, C.C. Wan, Y.Y. Wang, M.S. Wu, Thermal shutdown behavior of PVdF-HFP based polymer electrolytes comprising heat sensitive cross-linkable oligomers, J. Power Sources. 144 (2005) 238–243. doi:10.1016/j.jpowsour.2004.12.043.

[37] J. Treger, US5091272, 1992.

[38] K. Nguyen, C. Wensley, US6749961B1, 2004.

[39] S.S. Zhang, A review on the separators of liquid electrolyte Li-ion batteries, J. Power Sources. 164 (2007) 351–364. doi:10.1016/j.jpowsour.2006.10.065.

[40] M. Baginska, B.J. Blaiszik, R.J. Merriman, N.R. Sottos, J.S. Moore, S.R. White, Autonomic shutdown of Lithium-ion batteries using thermoresponsive microspheres, Adv. Energy Mater. 2 (2012) 583–590. doi:10.1002/aenm.201100683.

[41] K. Xu, M.S. Ding, S. Zhang, J.L. Allen, T.R. Jow, An Attempt to Formulate Nonflammable Lithium Ion Electrolytes with Alkyl Phosphates and Phosphazenes, J. Electrochem. Soc. 149 (2002) A622–A626. doi:10.1149/1.1467946.

[42] K. Xu, S. Zhang, J.L. Allen, T.R. Jow, Nonflammable Electrolytes for Li-Ion Batteries Based on a Fluorinated Phosphate, J. Electrochem. Soc. 149 (2002) A1079. doi:10.1149/1.1490356.

[43] Z. Jin, H. Gao, C. Kong, H. Zhan, Z. Li, A Novel Phosphate-Based Flame Retardant and Film-Forming Electrolyte Additive for Lithium Ion Batteries, ECS Electrochem. Lett. 2 (2013) A66–A68. doi:10.1149/2.005307eel.

[44] D.H.C. Wong, J.L. Thelen, Y. Fu, D. Devaux, A.A. Pandya, V.S. Battaglia, N.P. Balsara, J.M. DeSimone, Nonflammable perfluoropolyether-based electrolytes for lithium batteries., Proc. Natl. Acad. Sci. U. S. A. 111 (2014) 3327–31. doi:10.1073/pnas.1314615111.

[45] J.Y. Luo, W.J. Cui, P. He, Y.-Y. Xia, Raising the cycling stability of aqueous lithium-ion batteries by eliminating oxygen in the electrolyte., Nat. Chem. 2 (2010) 760–5. doi:10.1038/nchem.763.

[46] H. Kim, J. Hong, K.Y. Park, H. Kim, S.W. Kim, K. Kang, Aqueous rechargeable Li and Na ion batteries, Chem. Rev. 114 (2014) 11788–11827. doi:10.1021/cr500232y.

[47] D.H. Fritts, US4075400, 1978.

[48] W. Li, P. Liu, US8309240B1, 2012.

[49] R. Kizilel, R. Sabbah, J.R. Selman, S. Al-Hallaj, An alternative cooling system to enhance the safety of Li-ion battery packs, J. Power Sources. 194 (2009) 1105–1112. doi:10.1016/j.jpowsour.2009.06.074.

[50] S. Eaves, B. Bubois, F. Bakhtyari, US20100028758A1, 2010.

[51] A. Prillutsky, W.A. Hermann, EP2302727B1, 2010.

[52] D. Tse, US8846232B2, 2014.

[53] S. Energy, Panasonic NCR18650B Specifications Sheet, 2012.

[54] E.M. Verks, EVTV Monitor / Controller For Tesla Model S Battery Modules, 2017.

[55] P. Rez, Embodied Energy and Energy Return on Investment, in: Simple Phys. Energy Use, 2017: p. 222.

[56] P. Liu, R. Ross, A. Newman, Long-range, low-cost electric vehicles enabled by robust

energy storage, MRS Energy Sustain. 2 (2015). doi:10.1557/mre.2015.13.

[57] W. Zhao, G. Luo, C.-Y. Wang, Modeling Nail Penetration Process in Large-Format Li-Ion Cells, J. Electrochem. Soc. 162 (2015) A207–A217. doi:10.1149/2.1071501jes.

[58] T. Volck, W. Sinz, G. Gstrein, C. Breitfuss, S. Heindl, H. Steffan, S. Freunberger, M. Wilkening, M. Uitz, C. Fink, A. Geier, Method for Determination of the Internal Short Resistance and Heat Evolution at Different Mechanical Loads of a Lithium Ion Battery Cell Based on Dummy Pouch Cells, Batteries. 2 (2016) 8. doi:10.3390/batteries2020008.

[59] T.M. Bandhauer, S. Garimella, T.F. Fuller, A Critical Review of Thermal Issues in Lithium-Ion Batteries, J. Electrochem. Soc. 158 (2011) R1. doi:10.1149/1.3515880.

[60] P. Ribière, S. Grugeon, M. Morcrette, S. Boyanov, S. Laruelle, G. Marlair, Investigation on the fire-induced hazards of Li-ion battery cells by fire calorimetry, Energy Environ. Sci. 5 (2012) 5271–5280. doi:10.1039/c1ee02218k.

[61] D.H. Doughty, Vehicle Battery Safety Roadmap Guidance, National Renewable Energy Laboratory, Albuquerque, NM, 2012.

[62] Y. Xing, E.W.M. Ma, K.L. Tsui, M. Pecht, Battery Management Systems in Electric and Hybrid Vehicles, Energies. (2011) 1840–1857. doi:10.3390/en4111840.

[63] C. Lan, J. Xu, Y. Qiao, Y. Ma, Thermal management for high power lithium-ion battery by minichannel aluminum tubes, Appl. Therm. Eng. 101 (2016) 284–292. doi:10.1016/j.applthermaleng.2016.02.070.

[64] W.Q. Li, Z.G. Qu, Y.L. He, Y.B. Tao, Experimental study of a passive thermal management system for high-powered lithium ion batteries using porous metal foam saturated with phase change materials, J. Power Sources. 255 (2014) 9–15. doi:10.1016/j.jpowsour.2014.01.006.

[65] J. Remmlinger, M. Buchholz, M. Meiler, P. Bernreuter, K. Dietmayer, State-of-health monitoring of lithium-ion batteries in electric vehicles by on-board internal resistance estimation, J. Power Sources. 196 (2011) 5357–5363. doi:10.1016/j.jpowsour.2010.08.035.

[66] Y. Zou, X. Hu, H. Ma, S.E. Li, Combined State of Charge and State of Health estimation over lithium-ion battery cell cycle lifespan for electric vehicles, J. Power Sources. 273 (2015) 793–803. doi:10.1016/j.jpowsour.2014.09.146.

[67] X. Feng, C. Weng, M. Ouyang, J. Sun, Online internal short circuit detection for a large format lithium ion battery, Appl. Energy. 161 (2016) 168–180. doi:10.1016/j.apenergy.2015.10.019.

[68] B.N. Pinnangudi, S.B. Dalal, N.K. Medora, A. Arora, J. Swart, Thermal shutdown characteristics of insulating materials used in lithium ion batteries, Proc. - 2010 IEEE Symp. Prod. Compliance Eng. PSES 2010. (2010) 4–8. doi:10.1109/PSES.2010.5636859.

[69] W. Ji, B. Jiang, F. Ai, H. Yang, X. Ai, Temperature-responsive microspheres-coated

separator for thermal shutdown protection of lithium ion batteries, RSC Adv. 5 (2015) 172–176. doi:10.1039/c4ra11500g.

[70] Z. Chen, P.C. Hsu, J. Lopez, Y. Li, J.W.F. To, N. Liu, C. Wang, S.C. Andrews, J. Liu, Y. Cui, Z. Bao, Fast and reversible thermoresponsive polymer switching materials for safer batteries, Nat. Energy. 1 (2016) 15009. doi:10.1038/NENERGY.2015.9.

[71] X.M. Feng, X.P. Ai, H.X. Yang, A positive-temperature-coefficient electrode with thermal cut-off mechanism for use in rechargeable lithium batteries, Electrochem. Commun. 6 (2004) 1021–1024. doi:10.1016/j.elecom.2004.07.021.

[72] R. Zhao, S. Zhang, J. Gu, J. Liu, S. Carkner, E. Lanoue, An experimental study of lithium ion battery thermal management using flexible hydrogel films, J. Power Sources. 255 (2014) 29–36. doi:10.1016/j.jpowsour.2013.12.138.

[73] A.V. Le, M. Wang, D.J. Noelle, Y. Shi, Y. Qiao, Mitigating thermal runaway of lithium-ion battery by using thermally sensitive polymer blend as cathode binder, J. Appl. Polym. Sci. 135 (2017) 45737. doi:10.1002/app.45737.

[74] M. Wang, A. V Le, D.J. Noelle, Y. Shi, Y.S. Meng, Y. Qiao, Internal-short-mitigating current collector for lithium-ion battery, J. Power Sources. 348 (2017) 84–93. doi:10.1016/j.jpowsour.2017.03.004.

[75] A. V Le, M. Wang, Y. Shi, D.J. Noelle, Y. Qiao, Heat generation of mechanically abused lithium-ion batteries modified by carbon black micro-particulates, J. Phys. D. Appl. Phys. 48 (2015) 385501. doi:10.1088/0022-3727/48/38/385501.

[76] Y. Shi, D.J. Noelle, M. Wang, A. V. Le, H. Yoon, M. Zhang, Y.S. Meng, J. Fan, D. Wu, Y. Qiao, Mitigating thermal runaway of lithium-ion battery through electrolyte displacement, Appl. Phys. Lett. 110 (2017) 63902. doi:10.1063/1.4975653.

[77] J. Ding, T. Tian, Q. Meng, Z. Guo, W. Li, P. Zhang, F.T. Ciacchi, J. Huang, W. Yang, Smart multifunctional fluids for lithium ion batteries: enhanced rate performance and intrinsic mechanical protection., Sci. Rep. 3 (2013) 2485. doi:10.1038/srep02485.

[78] R. Zhao, J. Liu, J. Gu, Simulation and experimental study on lithium ion battery short circuit, Appl. Energy. 173 (2016) 29–39. doi:10.1016/j.apenergy.2016.04.016.

[79] S. Santhanagopalan, P. Ramadass, J. (Zhengming) Zhang, Analysis of internal short-circuit in a lithium ion cell, J. Power Sources. 194 (2009) 550–557. doi:10.1016/j.jpowsour.2009.05.002.

[80] M. Park, X. Zhang, M. Chung, G.B. Less, A. Marie, A review of conduction phenomena in Li-ion batteries, J. Power Sources. 195 (2010) 7904–7929. doi:10.1016/j.jpowsour.2010.06.060.

[81] M. Schönleber, C. Uhlmann, P. Braun, A. Weber, A Consistent Derivation of the Impedance of a Lithium-Ion Battery Electrode and its Dependency on the State-of-Charge,

Electrochim. Acta. 243 (2017) 250–259. doi:10.1016/j.electacta.2017.05.009.

[82] S.J. Drake, M. Martin, D.A. Wetz, J.K. Ostanek, S.P. Miller, J.M. Heinzel, A. Jain, Heat generation rate measurement in a Li-ion cell at large C-rates through temperature and heat fl ux measurements, J. Power Sources. 285 (2015) 266–273. doi:10.1016/j.jpowsour.2015.03.008.

[83] W. Cai, H. Wang, H. Maleki, J. Howard, E. Lara-Curzio, Experimental simulation of internal short circuit in Li-ion and Li-ion-polymer cells, J. Power Sources. 196 (2011) 7779–7783. doi:10.1016/j.jpowsour.2011.04.024.

[84] C. Lin, C. Cui, X. Xu, Lithium-ion battery electro-thermal model and its application in the numerical simulation of short circuit experiment, 2013 World Electr. Veh. Symp. Exhib. (2013) 1–8. doi:10.1109/EVS.2013.6914959.

[85] H. Maleki, J.N. Howard, Internal short circuit in Li-ion cells, J. Power Sources. 191 (2009) 568–574. doi:10.1016/j.jpowsour.2009.02.070.

[86] P.R. Shearing, E. Darcy, M. Keyser, B. Tjaden, T.M.M. Heenan, R. Jervis, J.J. Bailey, R. Malik, N.T. Vo, O. V. Magdysyuk, R. Atwood, M. Drakopoulos, M. DiMichiel, A. Rack, G. Hinds, D.J.L. Brett, P.R. Shearing, Characterising thermal runaway within lithium-ion cells by inducing and monitoring internal short circuits, Energy Environ. Sci. 10 (2017) 1377–1388. doi:10.1039/C7EE00385D.

[87] W. Waag, D. Uwe, Adaptive estimation of the electromotive force of the lithium-ion battery after current interruption for an accurate state-of-charge and capacity determination, Appl. Energy. 111 (2013) 416–427. doi:10.1016/j.apenergy.2013.05.001.

[88] S. Nejad, D.T. Gladwin, D.A. Stone, Sensitivity of lumped parameter battery models to constituent parallel-RC element parameterisation error, IECON Proc. (Industrial Electron. Conf. 40th Annua (2014) 5660–5665. doi:10.1109/IECON.2014.7049367.

[89] J.H. Kim, S.J. Lee, J.M. Lee, B.H. Cho, A new direct current internal resistance and state of charge relationship for the li-ion battery pulse power estimation, in: 7th Internatonal Conf. Power Electron. ICPE'07, 2008: pp. 1173–1178. doi:10.1109/ICPE.2007.4692563.

[90] S. Lee, J. Kim, J. Lee, B.H. Cho, State-of-charge and capacity estimation of lithium-ion battery using a new open-circuit voltage versus state-of-charge, J. Power Sources. 185 (2008) 1367–1373. doi:10.1016/j.jpowsour.2008.08.103.

[91] T. Dubeshter, J. Jorne, Pulse Polarization for Li-Ion Battery under Constant State of Charge : Part I . Pulse Discharge Experiments, J. Electrochem. Soc. 164 (2017) E3539–E3546. doi:10.1149/2.0551711jes.

[92] K. Onda, T. Ohshima, M. Nakayama, K. Fukuda, T. Araki, Thermal behavior of small lithium-ion battery during rapid charge and discharge cycles, J. Power Sources. 158 (2006) 535–542. doi:10.1016/j.jpowsour.2005.08.049.

[93] Y. Ji, Y. Zhang, C.-Y. Wang, Li-Ion Cell Operation at Low Temperatures, J. Electrochem. Soc. 160 (2013) A636–A649. doi:10.1149/2.047304jes.

[94] CRC Handbook of Chemistry and Physics, in: 97th ed., CRC Press, 2006: p. 12.210.

[95] L.O. Valøen, J.N. Reimers, Transport Properties of LiPF6-Based Li-Ion Battery Electrolytes, J. Electrochem. Soc. 152 (2005) A882. doi:10.1149/1.1872737.

[96] P. Porion, Y.R. Dougassa, C. Tessier, L. El Ouatani, J. Jacquemin, M. Anouti, Comparative study on transport properties for LiFAP and LiPF6 in alkyl-carbonates as electrolytes through conductivity, viscosity and NMR self-diffusion measurements, Electrochim. Acta. 114 (2013) 95–104. doi:10.1016/j.electacta.2013.10.015.

[97] K. Kondo, M. Sano, A. Hiwara, T. Omi, M. Fujita, A. Kuwae, M. Iida, K. Mogi, H. Yokoyama, Conductivity and Solvation of Li+ Ions of LiPF6 in Propylene Carbonate Solutions, J. Phys. Chem. B. 104 (2000) 5040–5044. doi:10.1021/jp000142f.

[98] H. Lundgren, M. Behm, G. Lindbergh, Electrochemical Characterization and Temperature Dependency of Mass-Transport Properties of LiPF6 in EC:DEC, J. Electrochem. Soc. 162 (2014) A413–A420. doi:10.1149/2.0641503jes.

[99] P. Arora, M. Doyle, A.S. Gozdz, R.E. White, J. Newman, Comparison between computer simulations and experimental data for high-rate discharges of plastic lithium-ion batteries, J. Power Sources. 88 (2000) 219–231. doi:10.1016/S0378-7753(99)00527-3.

[100] D.S. Hall, J. Self, J.R. Dahn, Dielectric Constants for Quantum Chemistry and Li-Ion Batteries: Solvent Blends of Ethylene Carbonate and Ethyl Methyl Carbonate, J. Phys. Chem. C. 119 (2015) 22322–22330. doi:10.1021/acs.jpcc.5b06022.

[101] W.C. Yu, US5691077, 1997.

[102] S. Choi, H.K. Park, US8758925B2, 2014.

[103] K. Liu, W. Liu, Y. Qiu, B. Kong, Y. Sun, Z. Chen, D. Zhuo, D. Lin, Y. Cui, Electrospun core-shell microfiber separator with thermal-triggered flame-retardant properties for lithium-ion batteries, Sci. Adv. 3 (2017) e1601978. doi:10.1126/sciadv.1601978.

[104] A.K. Sachdev, M.W. Verbrugge, T.C. Pederson, W.R. Rodgers, H.G. Kia, H.W. Cox, P.D. Fasulo, I.A. Rousseau, T. Xia, US8951654B2, 2015.

[105] D.J. Noelle, M. Wang, A. V. Le, Y. Shi, Y. Qiao, Internal resistance and polarization dynamics of lithium-ion batteries upon internal shorting, Appl. Energy. 212 (2018) 796–808. doi:10.1016/j.apenergy.2017.12.086.

[106] G. Czechowski, J. Jadzyn, The Viscous Properties of Diols I . The Homologous Series of 1,2- and 1,n -Alkanediols, Zeitschrift Für Naturforsch. 58a (2003) 317–320. doi:10.1515/zna-2003-5-612.

[107] G. Czechowski, J. Jadzyn, The Viscous Properties of Diols . II . 1,2- and 1,5-Pentanediol in Water and 1-Pentanol Solutions, Zeitschrift Für Naturforsch. 58a (2003) 321–324. doi:10.1515/zna-2003-5-613.

[108] W.M. Haynes, ed., CRC Handbook of Chemistry and Physics, 97th ed., CRC Press, 2016.

[109] Y. Shi, D.J. Noelle, M. Wang, A. V. Le, H. Yoon, M. Zhang, Y.S. Meng, Y. Qiao, Exothermic behaviors of mechanically abused lithium-ion batteries with dibenzylamine, J. Power Sources. 326 (2016) 514–521. doi:10.1016/j.jpowsour.2016.07.034.

[110] Y. Shi, D.J. Noelle, M. Wang, A. V. Le, H. Yoon, M. Zhang, Y.S. Meng, Y. Qiao, Role of Amines in Thermal-Runaway-Mitigating Lithium-Ion Battery, ACS Appl. Mater. Interfaces. 8 (2016) 30956–30963. doi:10.1021/acsami.6b10501.

[111] G. Rokicki, A. Piotrowska, A new route to polyurethanes from ethylene carbonate, diamines and diols, Polymer (Guildf). 43 (2002) 2927–2935. doi:10.1016/S0032-3861(02)00071-X.

[112] P. Tran-Van, G. Herlem, B. Fahys, E. Kwa, T. Diaco, M. Herlem, Anomalous high salt conductivity in primary diamines as solvents, J. Mol. Liq. 123 (2006) 105–109. doi:10.1016/j.molliq.2005.06.003.

[113] E. McCafferty, N. Hackerman, Double Layer Capacitance of Iron and Corrosion Inhibition with Polymethylene Diamines, J. Electrochem. Soc. 119 (1972) 146–154. doi:10.1149/1.2404150.

[114] I. Danaee, M.N. Khomami, Effect of ethylenediamine on corrosion of AISI 4130 steel alloy in 30 % ethylene glycol solution under static and hydrodynamic condition, Materwiss. Werksttech. 43 (2012) 942–949. doi:10.1002/mawe.201200020.

[115] P. Liu, E. Sherman, A. Jacobsen, Design and fabrication of multifunctional structural batteries, J. Power. 189 (2009) 646–650. doi:10.1016/j.jpowsour.2008.09.082.

[116] J.F. Snyder, E.B. Gienger, E.D. Wetzel, Performance metrics for structural composites with electrochemical multifunctionality, J. Compos. Mater. 49 (2015) 1835–1848. doi:10.1177/0021998314568167.

[117] L.E. Asp, E.S. Greenhalgh, Structural power composites, Compos. Sci. Technol. 101 (2014) 41–61. doi:10.1016/j.compscitech.2014.06.020.

[118] Y. Zhang, J. Ma, A.K. Singh, L. Cao, J. Seo, C.D. Rahn, C.E. Bakis, M.A. Hickner, Multifunctional structural lithium-ion battery for electric vehicles, J. Intell. Mater. Syst. Struct. 28 (2017) 1603–1613. doi:10.1177/1045389X16679021.

[119] P. Ladpli, R. Nardari, F. Kopsaftopoulos, Y. Wang, F. Chang, Design of Multifunctional Structural Batteries with Health Monitoring Capabilities, in: 8th Eur. Work. Sturctural Heal. Monit., Bilbao, Spain, 2016: pp. 5–8.

[120] J.S. Wang, P. Liu, E. Sherman, M. Verbrugge, H. Tataria, Formulation and characterization

of ultra-thick electrodes for high energy lithium-ion batteries employing tailored metal foams, J. Power Sources. 196 (2011) 8714–8718. doi:10.1016/j.jpowsour.2011.06.071.

[121] G.F. Yang, K.Y. Song, S.-K. Joo, Ultra-thick Li-ion battery electrodes using different cell size of metal foam current collectors, RSC Adv. 5 (2015) 16702–16706. doi:10.1039/C4RA14485F.

[122] J. Nishimura, K. Okuno, K. Kimura, K. Goto, H. Sakaida, A. Hosoe, R. Yoshikawa, Development of New Aluminum-Celmet Current Collector That Contributes to the Improvement of Various Properties of Energy Storage Devices, SEI Tech. Rev. 76 (2013) 40–44.

[123] H. Nara, T. Yokoshima, H. Mikuriya, S. Tsuda, T. Momma, T. Osaka, The Potential for the Creation of a High Areal Capacity Lithium-Sulfur Battery Using a Metal Foam Current Collector, J. Electrochem. Soc. 164 (2017) A5026–A5030. doi:10.1149/2.0381701jes.

[124] Z. Yuan, N. Rayess, N. Dukhan, Modeling of the Mechanical Properties of a Polymer-Metal Foam Hybrid, Procedia Mater. Sci. 4 (2014) 207–211. doi:http://dx.doi.org/10.1016/j.mspro.2014.07.602.

[125] N. Dukhan, N. Rayess, J. Hadley, Characterization of aluminum foam-polypropylene interpenetrating phase composites: Flexural test results, Mech. Mater. 42 (2010) 134–141. doi:10.1016/j.mechmat.2009.09.010.

[126] G.F. Yang, K.Y. Song, S.K. Joo, A metal foam as a current collector for high power and high capacity lithium iron phosphate batteries, J. Mater. Chem. A. 2 (2014) 19648–19652. doi:10.1039/C4TA03890H.

[127] H. Sakaida, K. Goto, K. Kimura, K. Okuno, J. Nishimura, A. Hosoe, Aluminum-Celmet―Aluminum Porous Metal with Three-Dimensional Consecutive Pores, SEI Tech. Rev. (2017) 87–92.

[128] B.Y. Wyser, C. Pelletier, J. Lange, Predicting and Determining the Bending Stiffness of Thin Films and Laminates, Packag. Technol. Sci. 14 (2001) 97–108.

[129] T.B. Atwater, P.J. Cygan, F.C. Leung, Man portable power needs of the 21st century. I. Applications for the dismounted soldier. II. Enhanced capabilities through the use of hybrid power sources, J. Power Sources. 91 (2000) 27–36. doi:10.1016/S0378-7753(00)00484-5.

[130] A. Magasinski, B. Zdyrko, I. Kovalenko, B. Hertzberg, R. Burtovyy, C.F. Huebner, T.F. Fuller, I. Luzinov, G. Yushin, Toward Efficient Binders for Li-Ion Battery Si-Based Anodes : Polyacrylic Acid, Appl. Mater. Interfaces. 2 (2010) 3004–3010. doi:10.1021/am100871y.

[131] J.G. Kim, B. Son, S. Mukherjee, N. Schuppert, A. Bates, O. Kwon, M.J. Choi, H.Y. Chung, S. Park, A review of lithium and non-lithium based solid state batteries, J. Power Sources. 282 (2015) 299–322. doi:10.1016/j.jpowsour.2015.02.054.

[132] N. Loeffler, T. Kopel, G. Kim, S. Passerini, Polyurethane Binder for Aqueous Processing of Li-Ion Battery, J. Electrochem. Soc. 162 (2015) 2692–2698. doi:10.1149/2.0641514jes.